Oxygen-mediated mitigation of Ru/Al_2O_3 deactivation during propane steam reforming

Submitted by Stephen Cotterrell

In partial fulfilment of the requirements of Master of Science in engineering

February 2023

Synopsis

Short catalytic lifespans may hinder the deployment of fuel-processor technology. The development of stable catalysts and processes to prolong catalyst lifespan is therefore important to the deployment of this technology. Ruthenium-based steam reforming catalysts are of great research interest because of the high activity of ruthenium in steam reforming, in comparison to other platinum group metals (PGMs), and the relative availability of ruthenium as a co-product of PGM mining. Deactivation by coking in typical industrial steam reforming catalysts is a well-documented phenomenon.

This study primarily investigates the effects of co-feeding air in several propane steam reforming experiments. It hypothesises that carbon deposition is the primary mechanism of catalytic deactivation, and that the addition of a co-feed of air in small proportion (1 – 3%) to the total dry feed will avail free oxygen in the reactor bed, which will incur the gasification of deposited carbon, facilitating reduced deactivation. The study also seeks to investigate the effects of varying steam-to-carbon ratio, and the effects of steaming the catalyst prior to introduction of the dry feed.

Two sets of experiments were performed – four using calcined and reduced catalyst, and two using calcined, reduced, and steamed catalyst. The experiments using the calcined and reduced catalyst followed three clear phases, *viz*., activation spanning 10 – 20 h, deactivation spanning several hundred h, and stable performance following complete deactivation. In comparison, the experiments using the calcined, reduced, and steamed catalyst displayed two reaction phases – a substantially higher initial activity with rapid deactivation spanning around 10 h, and a lower stable performance once deactivation was complete.

The effect of co-feeding air in the reformer was found to have a limited and effectively negligible effect on conversion. Notwithstanding, some effects were observed, particularly a favourable shift in carbon product selectivities. The effects were most pronounced in the experiment in which the highest co-feed was used, indicating that the effect scales with co-feed size. The effects were found to be reversible on removal of the co-feed.

It was found that, within the range of steam-to-carbon ratios tested (2.5 – 6), there was a remarkably limited difference in catalytic performance, indicating that this was not a controlling factor in the rate of deactivation.

Characterisation of the catalyst recovered from the experiments confirmed the presence of both graphitic carbon and carbon nanotubes in significant quantities, confirming that this was likely the mechanism of deactivation.

Further work should investigate the effect of co-feeding air at larger proportions of the dry feed, as this is where the greatest effect was observed. The equipment should be refined so that it is more reliable, and capable of performing experiments at higher temperatures which are more favourable for steam reforming.

Acknowledgments

First and foremost, I would like to express my gratitude to my supervisor, Professor Jack C.Q. Fletcher, for the opportunity to perform this project, and for his work to ensure that this project was funded. The direction and support I have received from Prof Fletcher has been invaluable, and his patience has helped to run it through completion. I would like to thank the rest of my supervisory team: Mr Stephen Roberts, for his support in the lab and consistent availability for troubleshooting; Dr Jack V. Fletcher for further guidance with regards to lab work and theory; and Mr Niels Luchters for his technical expertise. I would also like to thank Professor Patricia Kooyman for her input and expertise, and the many hours spent in the electron microscopy unit.

I would like to thank the following technical staff at the Catalysis Institute in the Department of Chemical Engineering: Mr Waldo Koorts, Ms Portia Johnston, Ms Chantal Le Roux and Ms Rachel Cupido, for always being available to offer assistance and expertise. Particular thanks go to Mr Waldo Koorts, for his consistent availability and technical expertise throughout this project, and for his friendship which has been an invaluable source of support. I would also like to thank the staff at the IKEY workshop, particularly Aviwe Poswayo and Darryn Stevens, for their support, particularly in my attempts to keep my furnace operational.

I would like to thank my sisters, Emily, Jessica, Julia, Ashleigh, and Isobella, for their encouragement. I would also like to thank my relatives in Cape Town: Cron and Shelley, Richard and Arianne, and my grandmother Gill, for the time we have spent together and the assistance that they have provided. In particular, I would like to thank my parents, Mark and Theresa, for their unrelenting support and faith in me.

I would like to thank my friends in the department for keeping me motivated – Nicole Uys, Evren Turan, Sally Berge, James Hockey, Hayley Swait, Sage Govender, Fernando Ortega, Vuyisile Mahlaba and Kin De Kock. I would like to thank Junfeng Guo in particular for his friendship, mentorship, and guidance – his assistance in teaching me various concepts in catalysis when I was new to the field was instrumental. I would also like to thank Dr John Woodland from chemistry for our lunches on campus and his academic assistance.

I would like to thank the UCT Brewing Team for the skills, friends, and appreciation for beer that I have gained over this time. I would also like to thank the members of beer club — Mr Waldo Koorts, Mr Graham Inggs, Prof Nico Fischer, Mr Joachim Macke, Mr Hilton Heydenrych, Mr James Heydenrych, and Prof Klaus Moller – for their support, academic and otherwise, and for always being there to share a beer.

Lastly, I would like to acknowledge the Department of Chemical Engineering at UCT for the skills I learned during my undergraduate years, and for the opportunity to continue studying in the form of this research project. I appreciate the many world-class facilities to which I have had access over this period.

Declaration

I know the meaning of plagiarism and declare that all the work in the document, save for that which is properly acknowledged, is my own. This thesis/dissertation has been submitted to the Turnitin module (or equivalent similarity and originality checking software) and I confirm that my supervisor has seen my report and any concerns revealed by such have been resolved with my supervisor.

Signed by candidate

Stephen Cotterrell

2 February 2023

Contents

List of Figures

List of Tables

Nomenclature

Term	*Description*
CR-#	Experimental run using Calcined and Reduced catalyst
Cracking	Reaction of hydrocarbon to form smaller C_nH_m products
CR-Cat	Calcined and Reduced Catalyst
CRS-#	Experimental run using Calcined Reduced and Steamed catalyst
CRS-Cat	Calcined, Reduced and Steamed Catalyst
DTA	Differential Thermal Analysis
DTG	Differential Thermogravimetric Analysis
EDX	Electron Dispersive X-ray Spectroscopy
FC-Cat	Fresh Calcined Catalyst
GC	Gas Chromatograph
GHGs	Greenhouse Gasses
HTS	High Temperature Shift (of water-gas-shift)
ICE	Internal Combustion Engine
LTS	Low Temperature Shift (of water-gas-shift)
MFC	Mass Flow Controller
MSA	Metal Surface Area
PEMFC	Proton-Exchange Membrane Fuel Cell
PGM	Platinum Group Metals
Reforming	Reaction of hydrocarbon to form H_2 and CO_x products
RRF	Relative Response Factor
S/C Ratio	Steam-to-carbon ratio
sccm	Standard cubic centimetres per minute
STP	Standard Temperature and Pressure (0°C, 1 bar)
TCD	Thermal Conductivity Detector
TEM	Transmission Electron Microscopy
TGA	Thermogravimetric Analysis
Time-on-stream	Time from the introduction of reactants in an experiment
TPO	Temperature-Programmed-Oxidation
TPR	Temperature-Programmed-Reduction
XRD	X-ray Diffractometry

1. Introduction

1.1. Background and Rationale

A broad goal of research and industry is to develop efficient technologies for cleaner energy production, with lower emissions in comparison to traditional internal combustion engines (ICEs). In particular, there have been large advances in the field of fuel cells. Much development has occurred in proton-exchange membrane fuel cells (PEMFCs), which are now able to produce electricity with suitable current and through potentially viable product lifespans to compete with ICEs [1].

PEMFCs promise efficient and low emission energy generation, compared to ICEs. PEMFCs have a theoretical maximum efficiency of 83%, and actual attained efficiency in the range of 50 – 70% [2]. Even in applications where impure hydrogen fuel source affects efficiency, it is possible to achieve efficiencies of 40% [2]. PEMFCs are also pegged as an environmentally friendly solution to energy production, due to their near-zero emission of greenhouse gasses (GHGs). If operated using pure hydrogen, the only by-products of a PEMFC system are heat and water. Indeed, even when hydrogen is generated from hydrocarbon fuels, the emissions can be limited to CO_2 and a small quantity of hydrocarbons during start-up. This contrasts with ICEs, which typically achieve an efficiency of 20 – 25 %, and may produce significant environmental pollutants, such as NO_x [3-5].

In the absence of a functioning hydrogen economy, a critical issue in the deployment of PEMFC systems is availability of hydrogen feedstock. While much research has been undertaken into hydrogen storage, these technologies still experience significant shortcomings, primarily low volumetric and gravimetric storage density [6].

Industrially, hydrocarbon-to-hydrogen processing is performed on an extremely large scale, typically utilising nickel-based catalysts for the important process step of reforming [7]. Such catalysts have complicated pre-operational reduction procedures, are pyrophoric on exposure to air and are run with extended periods of time-on-stream. Another important aspect is the inherent safety of equipment. Nickel catalysts are pyrophoric, which is acceptable in industrial settings where the opening of the reactor can be highly controlled, but this is not the same for ‘basement’-style settings, where the reactor may be broken and/or opened, accidentally or otherwise.

Consequent to demand for supply of hydrogen for PEMFCs, research into fuel-to-hydrogen processing technology is needed. An alternative means of availing hydrogen for use in PEMFC systems is through the processing of hydrocarbons through catalytic reforming in small scale productions. The design requirements for a small-scale distributed hydrogen production system are significantly different from those in industrial settings. A key change in design requirements is that the reactors need to be scaled down and simplified. It is not feasible for energy to be transferred to reactors in the same manner as in industrial settings.

The development of smaller portable processing technology has significantly different design requirements than those found in industrial settings. The nature of the proposed applications requires catalysts which do not have elaborate pre-operational procedures, are safe on accidental exposure to air, and are stable through frequent start-up and shut-down cycles.

Consequently, research into PGM reforming catalysts, such as supported ruthenium catalysts is ongoing. PGM reforming catalysts overcome many of the shortcomings of nickel-based catalysts, such as deactivation, safety, and scalability.

There is strong interest in alumina-supported ruthenium catalysts because of the high activity of ruthenium and its relatively low cost in comparison to other platinum group metals. However, catalyst deactivation remains a concern in all catalytic systems with the consequent desire to mitigate this deactivation through optimising operating conditions, feed composition, reactivation techniques or catalyst reformulation.

The literature consensus is that the primary cause of deactivation of Ru/Al_2O_3 catalysts is through coking/carbon deposition. For this reason, the introduction of small quantities of air into the reformer feed is proposed to enhance the rate of carbon gasification, thus mitigating the deactivation.

1.2. Problem statement

The production of reformate is a key step in the production of a hydrogen fuel source for PEMFCs. However, deactivation of reforming catalysts remains a key issue to be controlled, since catalytic performance stability is essential to the implementation of fuel processor technology, particularly when this is intended outside of an industrial setting. In this regard, ruthenium catalysts are reported to be both highly active and stable in steam reformer applications. Nonetheless, for the extended catalyst lifetimes necessary for fuel processor deployment, further mitigation of catalyst deactivation via carbon laydown is essential and, to this end, the inclusion of a low concentration oxygen (air) co-feed for enhanced carbon removal is worthy of evaluation.

In addition, fuel processor deployment in remote settings brings the additional constraint of the limited availability of sufficiently pure water, much of it to be recovered from the fuel processor effluent streams. Consequently, with reformer steam-to-carbon ratio impacting carbon laydown, the effect of steam-to-carbon ratio on catalyst performance and deactivation behaviour is also to be investigated.

1.3. Scope of Study

This study encompasses the construction and commissioning a packed-bed reactor system capable of evaluating the performance of an Ru/Al_2O_3 catalyst for the steam reforming of propane, over extended periods, with provision for co-feeding air (oxygen). Experiments were

conducted to evaluate the performance of an in-house prepared 5 wt% Ru/Al_2O_3 catalyst, and comparative experiments were performed to evaluate the impact of co-feeding air and varying reactor steam-to-carbon ratio on catalytic performance and deactivation.

1.4. Research Objectives

The scope of this study included:

- synthesis and characterisation of a 5 wt% Ru/Al_2O_3 steam reforming catalyst
- investigation into whether the introduction of small quantities of air (specifically the co-feeding of air at 1 – 3%) into the steam reformer feed effects of feed composition on the performance and deactivation of the catalyst, specifically whether it slows the rate of carbon deposition on the catalyst and therefore slows down or prevents catalyst deactivation
- investigation into the effect of altering the S/C ratio on the rate of deactivation
- characterisation of the used and deactivated catalyst to ascertain the mechanism of deactivation

1.5. Hypothesis

It was hypothesised that feeding air in small proportions, i.e., 1 to 3%, of the total dry feed of the reforming reaction could serve to enhance carbon removal from the catalyst, and in so doing improve both the catalyst activity and stability.

2. Literature review

2.1. Fuel cell technology

A fuel cell is an electrochemical device used to convert the chemical energy of a fuel directly into utilisable electrical energy [1]. Fuel cells combine a fuel with oxygen through redox reactions to produce electricity. Hydrogen is used in most fuel cell types, with the exception of Direct Methanol Fuel Cells (DMFCs) . Hydrogen is an attractive fuel source because it is highly reactive on an appropriate catalyst, has by-products of only heat and water, and has a higher energy density and efficiency in comparison to other fuels [8].

2.1.1. Types of fuel cells

Fuel cells are classified primarily by the kind of electrolyte that they employ. The electrolyte determines the kind of electrochemical reactions that occur in the cell, the catalysts required, the operating temperature range, the fuel required, and other factors as shown in Table 2.1 [9].

Table 2.1: Types of fuel cells and their electrolytes, fuels, electrocatalysts and operating temperature ranges, adapted from Carrette et al. [8] and Barbir [1].

Type of fuel cell	***Common electrolyte***	***Fuel***	***Electrocatalysts***	***Temp. range***
Proton exchange membrane (PEMFC)	Persulfonated acid polymer	Hydrogen	Pt-alloy/C, often PtRu	60-80°C
Direct methanol (DMFC)	Acidic membrane	Methanol	Pt-alloy/C	>80°C
Alkaline (AFC)	KOH in water	Hydrogen	Pt-alloy/C	<100°C
Phosphoric acid (PAFC)	H_3PO_4 in matrix	Hydrogen	Pt-alloy/C	150-200°C
Molten carbonate (MCFC)	Molten carbonate in alumina matrix	Hydrogen	Ni/Al or Ni/Cr	600-700°C
Solid oxide (SOFC)	Ceramics	Hydrogen	Ni/YSZ $(La,Sr,Ca)MnO_3$	500-1000°C

Under the electrolyte classification, DMFCs are technically a form of PEMFC, however, they are often categorised separately.

Figure 2.1 depicts the mechanism by which various types of fuel cells operate and what ions pass through the electrolyte.

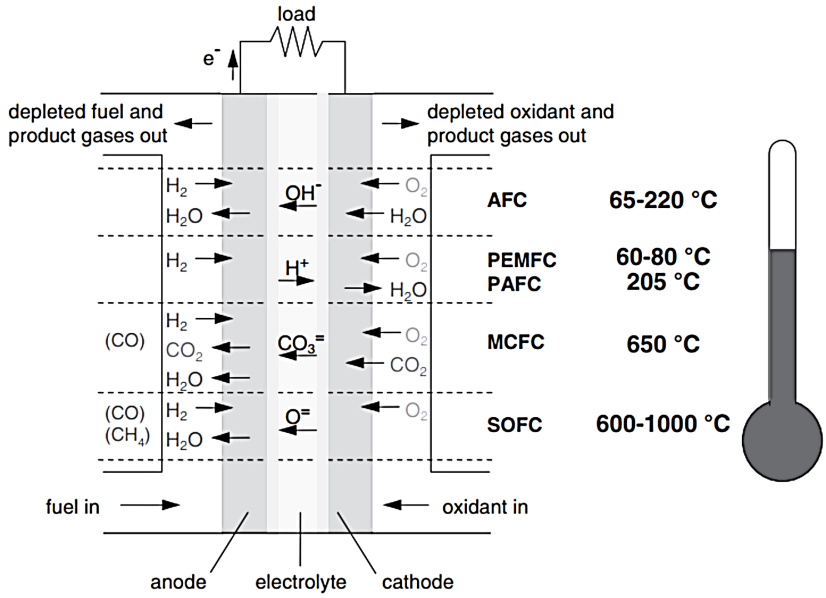

Figure 2.1: Fuel cell types, their reactions and operating temperatures, taken from Barbir [1]

The different types of fuel cells exhibit various advantages and disadvantages. For instance, AFCs are regarded as having the highest electrical efficiencies of all fuel cells [8], but they are extremely sensitive to poisoning due to carbonate formation, making them unsuitable for use with reformate hydrogen streams.

Proton exchange membrane fuel cells (PEMFCs), also called polymer electrolyte membrane fuel cells, have attracted much attention relative to other types of fuel cells due to several advantages. They deliver high power density and offer lower weight and volume when compared to other fuel cells. They also operate at lower temperatures (80°C) than other fuel cells, resulting in a faster warm up-time and thus faster start-up. Furthermore, they can be used with a reformate stream containing hydrogen. The current disadvantage of PEMFCs is that they are susceptible to catalyst poisoning and sintering, which limits their lifespan.

2.1.2. Structure and operation of PEM fuel cells

The fuel for a PEM fuel cell may be generated in several ways. The purity of the hydrogen source will influence the efficiency of the fuel cell. Hydrogen may be externally produced, purified, and stored, providing a high purity hydrogen stream. Hydrogen may also be produced on site by electrolysis. Alternatively, hydrogen may be used in the form of a reformate, from the steam reforming of methane, LPG or methanol [8].

A fuel cell consists of two electrodes (an anode and a cathode) which are separated by an electrolyte. Oxidation and reduction reactions occur on the surface of the electrodes. The electrodes possess a layer of catalyst to increase the rate of the reactions. A typical PEM fuel cell contains electrodes which are composed of platinum particles supported on carbon, or carbon-based materials.

In operation, hydrogen enters the fuel cell and moves towards the anode via diffusion and/or convection. Hydrogen adsorbs onto the active phase surface, where it dissociates to form hydrogen ions and electrons [1]. The reaction proceeds per equation (2.1).

$$H_2 \rightleftharpoons 2H^+ + 2e^- \tag{2.1}$$

Protons from the oxidation reaction pass through the selectively-permeable membrane (electrolyte) to the cathode. A voltage is produced, and electrons pass through an external circuit to reach the cathode. Oxygen enters the system and is combined with the protons and electrons at the cathode to form water. The reaction proceeds per equation (2.2).

$$½\ O_2 + 2H^+ + 2e^- \rightleftharpoons H_2O \tag{2.2}$$

The overall reaction is represented by equation (2.3): [1]

$$H_2 + ½\ O_2 \rightarrow H_2O \tag{2.3}$$

The voltage that can be achieved by a fuel cell is dependent on temperature. For a fuel cell operating at 25°C, the maximum theoretical voltage that can be achieved is 1.23 V. Below 100°C, the changes in potential due to temperature are small and practically negligible, but for fuel cells operating at higher temperatures such as solid oxide fuel cells, the effect cannot be neglected.

In practical applications, the maximum theoretical voltage is not typically achieved, and the actual value is approximately 1 V. Since typical applications require an output voltage of 6 V to 200 V or higher, cells may be combined in series in what is called a fuel cell stack.

The use of reformate has several effects on PEMFC performance. These include the loss of potential due to lower hydrogen partial pressure, and catalyst poisoning via CO adsorption and other compounds. The loss in potential due to the decreased partial pressure of hydrogen can be calculated using the *Nernst equation [1]*, a simplified version of which is shown in equation (2.4):

$$E = E_0 + \frac{RT}{nF} \ln\left(\frac{P_{H_2} P_{O_2}^{0.5}}{P_{H_2O}}\right) \tag{2.4}$$

Where E is the half-cell potential, $E^0$is the standard half-cell potential, R is the universal gas constant, T is the absolute temperature in K, n is the is the valance of the electrode material, F is the Faraday constant, and $P_{species}$ represents the partial pressure of that chemical species.

2.2. Fuel processing for PEMFCs

Fuel processing encompasses the steps by which hydrocarbons are processed to a hydrogen-rich stream. The exact steps involved in fuel processing depend on the composition of the feed, the requirements of the downstream fuel cell, and the scale of the operation. The objectives of fuel processing are to maximise the yield of hydrogen while removing catalyst poisons affecting the fuel cell [10].

Since PEMFCs are highly sensitive to poisoning by CO, processing equipment for these fuel cells will seek to eliminate as much carbon monoxide as possible before the stream enters the fuel cell [8].

A typical fuel processing train, as seen in Figure 2.2, will consist of a reforming stage in which hydrocarbons are converted to syngas, a shift stage in which carbon monoxide is reacted with water to produce more hydrogen, and a CO clean-up stage comprising either of a preferential oxidation or selective methanation stage which seeks to eliminate any remaining carbon monoxide.

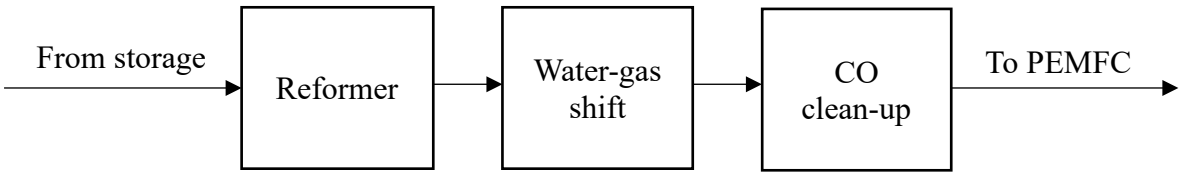

Figure 2.2: Block flow diagram of fuel processing train

2.2.1. Reforming

Reforming encompasses the reactions by which a hydrocarbon feedstock is converted to synthesis gas. Reforming is a primary focus of this research study and is discussed in greater detail in Section 2.3.

Reforming is generally performed in a single step; however, it may be split into two steps when heavier hydrocarbons are reformed. In such applications, a 'pre-reformer' may be used to break down heavier hydrocarbons into methane and carbon-oxides. Higher hydrocarbons are more likely to give rise to coke formation than lighter hydrocarbons [11]. Advantages of pre-reformers are the mitigation of carbon deposition due to cracking in downstream processes, and the selective adsorption of sulfur [12].

Pre-reformers typically operate adiabatically on nickel-based catalysts at temperatures between 380 – 500°C, and are able to process full range naphtha [11].

2.2.2. Water gas shift

The water gas shift (WGS) reaction is a critical step in fuel processers as a primary CO clean-up and additional hydrogen generation step [10]. WGS occurs downstream of the reformer. The reaction proceeds per equation (2.5).

$$CO + H_2O \rightleftharpoons CO_2 + H_2 \mid H^0_{298K} = -41.2\,kJ/mol \quad (2.5)$$

Per equation (2.5), WGS is an exothermic reaction and as such, under adiabatic conditions, is a thermodynamically limited reaction. However, it is kinetically favoured at higher temperatures. For this reason, WGS is typically conducted sequentially in separate high temperature (HTS) and low-temperature water gas shift (LTS) stages.

In industrial applications with long periods of continuous operation, the classical catalyst formulations are Fe/Cr oxide for the HTS stage and $Cu/ZnO/Al_2O_3$ for the LTS stage. Newer formulations have investigated PGMs supported on rare-earth metal oxides, particularly Pt/CeO_2. The Pt/CeO_2 formulation is of interest for fuel processor applications because of its activity in the medium-temperature range [10].

2.2.3. Carbon monoxide clean-up

Carbon monoxide in the PEMFC suppresses the performance of the fuel cell due to CO poisoning. Pt formulations are highly sensitive to CO poisoning, with concentrations as low as 100 ppm resulting in practically no current-generating ability [1]. PtRu formulations have demonstrated better resistance to CO poisoning, with only limited performance deterioration at CO concentrations as high as 100 ppm [13]. For optimal performance, it is preferable to operate with CO concentrations lower than 50 ppm [10]. A CO clean up-stage, in which CO is brought to minimal levels is therefore employed.

There are a variety of approaches that have been employed for the CO clean-up step: preferential CO oxidation, selective CO methanation and Pd-membrane separation. Preferential oxidation is reported as being the lowest-cost method to attain CO concentrations at the desired level, without excessive hydrogen consumption [14, 15]. However, the performance of the different process routes is similar and there is no definitive answer on which is preferred [16].

2.2.3.1. Preferential carbon monoxide oxidation

Preferential CO oxidation (PROX) is the process by which CO is preferentially oxidised instead of H_2. Since the reaction must be selective towards oxidising CO and not H_2, the reaction is always performed over a catalyst. PROX takes advantage of the strong adsorption of CO on the catalyst surface. The reaction typically takes place at moderate temperatures, around 200°C [17]. The reaction proceeds per equation (2.6), however, the significant and unwanted side-reaction of hydrogen oxidation proceeds per equation (2.7).

$$CO + ½O_2 \rightleftharpoons CO_2 \mid H^0_{298K} = -283\ kJ/mol \tag{2.6}$$

$$H_2 + ½O_2 \rightleftharpoons H_2O \mid H^0_{298K} = -242 kJ/mol \tag{2.7}$$

Other reactions affecting the performance of the PROX reactor are the WGS and methanation reactions.

PROX catalysts are typically supported PGMs or copper, sometimes with promoters. An example is Pt/α-Al_2O_3, which is common because of its wide range of operating temperatures and low selectivity for methanation [17]. Issues affecting PROX catalysts are catalyst lifetime and sensitivity to poisoning. Contaminants in the reformate, particularly sulfur, can render the catalyst inactive. The catalysts are also temperature-sensitive, and if an over-temperature event occurs, the performance and longevity of the catalyst can be severely compromised [17].

2.2.3.2. Selective carbon monoxide methanation

Selective CO methanation (SMET) is the process by which CO is preferentially hydrogenated over oxidation into CO_2 to remove the CO poison from a syngas stream. The reaction is mildly exothermic. The reaction proceeds per equation (2.8), with the unwanted side-reaction of the methanation of CO_2 proceeding per equation (2.9).

$$CO + 3H_2 \rightleftharpoons CH_4 + H_2O \mid H^0_{298K} = -206\ kJ/mol \tag{2.8}$$

$$CO_2 + 4H_2O \rightleftharpoons CH_4 + 2H_2O \mid H^0_{298K} = -164\ kJ/mol \tag{2.9}$$

The primary aim of selective methanation is to drive down the concentration of CO to an acceptable level without incurring unwanted hydrogen usage due to CO_2 methanation. The reaction occurs slowly on its own and must be performed in the presence of a catalyst.

Methanation is typically performed on supported nickel catalysts in industrial applications, but other metals, including molybdenum, cobalt and PGMs, have been investigated and found to possess methanation activity. Even so, nickel has been preferred industrially because it is relatively cheap, and because it possesses the greatest selectivity. Ni/Al_2O_3 catalysts are used in reactors operating in the temperature range of 165 – 205°C [18]. Supports have a significant impact on methanation activity and dehydrating agents such as Al_2O_3 have a beneficial effect on activity [18]. Al_2O_3 is the most commonly used methanation catalyst support [19].

Selective methanation carries with it the intrinsically associated problem of hydrocarbon emissions, which detracts from the goal of an environmentally-friendly FC unit.

2.3. Reforming

Reforming is the process by which hydrocarbons are reacted with gaseous water, oxygen and/or carbon dioxide to produce synthesis gas/reformate. Reforming encompasses many reactions since the reactions occurring are dependent on the feed composition.

Reforming is a costly process in terms of capital cost and often also in terms of operating cost. For instance, the typical steam reforming syngas production system will account for 54% of the capital expenditure in methanol production plants [20]. Furthermore, because of the strongly endothermic nature of the steam reforming reaction, significant energy must be supplied to the reformer to fuel the reaction, incurring large operating costs.

The exact reactions that occur in a reformer are dependent on the composition of the feed. For instance, bio-gas, containing both methane and carbon dioxide sourced from decomposing organic vegetal matter, typically undergoes dry reforming unless carbon dioxide can be separated out from the feed [21]. The principal reactions occurring in the reformer are summarised in Table 2.2.

Table 2.2: Summary of reactions occurring in reformers

Reaction	***Methane case***	***Generalised case***
Partial Oxidation	$CH_4 + ½\ O_2 \leftrightarrow CO + 2H_2$	$C_nH_m + {}^{n}/_{2}\ O_2 \rightarrow\ nCO + mH_2$
Steam Reforming	$CH_4 + H_2O \leftrightarrow CO + 3H_2$	$C_nH_m + nH_2O \rightarrow\ nCO + \left(n + {}^{m}/_{2}\right)H_2$
Dry Reforming	$CH_4 + CO_2 \leftrightarrow 2CO + 2H_2$	–
Water Gas Shift	$CO + H_2O \leftrightarrow CO_2 + H_2$	–

Combinations of the above reactions include autothermal reforming, in which steam reforming and partial oxidation are combined [22]; bi-reforming, in which dry reforming and steam reforming are combined [23, 24]; Oxy-CO_2 reforming, in which dry reforming and partial oxidation are combined [24]; and tri-reforming, in which dry reforming, partial oxidation, steam reforming and water-gas shift are combined [25, 26].

For fuel cell applications, it is desirable to attain the greatest possible hydrogen composition in the reformate because of the impact of hydrogen partial pressure on the electric potential of the PEMFC (see Nernst equation (2.4) on page 6). Consequently, in applications where pure hydrocarbons are available, steam reforming is generally preferred because of the greater quantity of hydrogen it produces per mole of feed.

Consequently, the three primary routes which have been employed for reforming are steam reforming (SR), partial oxidation (POX) and autothermal reforming (ATR). POX is not favoured because of its lower yield of hydrogen. ATR combines oxidation and steam reforming in a single unit, with the energy released by the POX reaction fuelling the steam reforming

reaction. Consequently, ATR has been of interest because of the size reduction and reduced heat transfer limitations in comparison to SR. Other advantages of ATR over SR include faster start-up and lower coking [10].

2.3.1. Steam reforming

2.3.1.1. Chemistry and thermodynamics of steam reforming

Steam reforming of LPG involves a combination of several reactions: the reforming short-chain alkanes, the reforming of methane, and the water gas shift reaction. The reforming of short-chain alkanes is non-reversible, whereas methane reforming and water-gas shift are reversible. Methane cracking may also occur under reaction conditions. These reactions are described by equations (2.10 – 2.13) below:

$$C_nH_m + nH_2O \rightarrow nCO + \left(n + {}^{m}/_{2}\right)H_2 \mid \Delta H^0_{298K} > 0 \quad (2.10)$$

$$CH_4 + H_2O \rightleftharpoons CO + 3H_2 \mid \Delta H^0_{298K} = 205.9\,kJ/mol \quad (2.11)$$

$$CO + H_2O \rightleftharpoons H_2 + CO_2 \mid \Delta H^0_{298K} = -41\,kJ/mol \quad (2.12)$$

$$CH_4 \rightarrow C + 2H_2 \mid \Delta H^0_{298K} = 74.6\,kJ/mol \quad (2.13)$$

It is typical for the steam reforming reaction to reach near total conversion, whereas it is not typical for the water-gas shift reaction to reach complete conversion and, consequently, the net reaction is strongly endothermic.

LPG is comprised of ethane, propane, and n-butane. The steam reforming of ethane, propane and n-butane are described by equations (2.14 – 2.16):

$$C_2H_6 + 2H_2O \rightarrow 5H_2 + 2CO \mid \Delta H^0_{298K} = 374.3\,kJ/mol \quad (2.14)$$

$$C_3H_8 + 3H_2O \rightarrow 7H_2 + 3CO \mid \Delta H^0_{298K} = 497.7\,kJ/mol \quad (2.15)$$

$$n\text{-}C_4H_{10} + 4H_2O \rightarrow 9H_2 + 4CO \mid \Delta H^0_{298K} = 651.3\,kJ/mol \quad (2.16)$$

However, under reaction conditions, several other reactions such as cracking into hydrogen and carbon, followed by gasification, and cracking into methane also occur [27]. Methane formation can also form by methanation of carbon monoxide with H_2. Cracking into carbon and hydrogen is described by equations (2.17 – 2.19), cracking into methane described by (2.20) and methanation described by (2.21).

$$C_2H_6 \rightarrow 3H_3 + 2C \mid \Delta H^0_{298K} = -84.7\,kJ/mol \quad (2.17)$$

$$C_3H_8 \rightarrow 4H_2 + 3C \mid \Delta H^0_{298K} = 103.8\,kJ/mol \quad (2.18)$$

$$n\text{-}C_4H_{10} \rightarrow 9H_2 + 4C \mid \Delta H^0_{298K} = 126.2\,kJ/mol \quad (2.19)$$

$$C_nH_m + xH_2O \rightarrow yH_2 + (n-1)CO + CH_4 \quad (2.20)$$

$$CO + 3H_2 \rightarrow CH_4 + H_2O \mid \Delta H^0_{298K} = -206\,kJ/mol \quad (2.21)$$

The stoichiometric ratio of steam-to-carbon (S/C) in steam reforming is 1:1, and 2:1 for the overall reaction including water gas shift. However, it is industrially a common practice to operate at steam-to-carbon ratios in the region of 2.5 – 4.0 [28]. This is done for multiple reasons, one being that the presence of excess steam drives the equilibrium conversion forward, but the primary stated reason is the suppression of carbon deposition. Figure 2.3 depicts the effect that S/C ratio has on the conversion of methane for varying temperatures and pressures, indicating the increased conversion attained by operating at a higher S/C ratio.

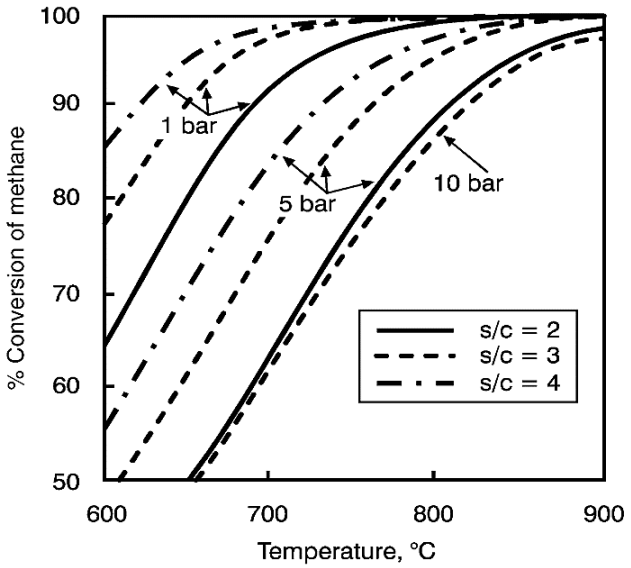

Figure 2.3: Equilibrium conversion of methane against temperature, pressure and steam/carbon ratios, taken from Joensen et al. [29]

The specific mechanism by which the reforming reactions proceed are dependent on the catalyst that is used. The catalyst support, active metal, and promoters all have an impact on the exact mechanism of the reaction.

2.3.1.2. Mechanism of steam reforming

The mechanism of LPG steam reforming is different to that of methane steam reforming, in that the rate determining step of the two reactions is different. In the steam reforming of methane, the activation of the C-H bond by dissociative adsorption is the rate determining step. The mechanism of the methane steam reforming reaction is reported in equations (2.22 – 2.30) below. In the reforming of LPG, the rate determining steps have been proposed as the C-C bond rupture or the oxidation of the adsorbed CH_n species, though studies have reported different results [27].

The above notwithstanding, the mechanism of methane steam reforming is important to understanding the mechanism of LPG reforming, especially if one takes the cracking to methane as an important step in the LPG reforming process.

The mechanism of steam reforming of methane is reported in Subramani *et al.* [27] from Joensen *et al.* [29] and Chorkendorff *et al.* [30]. Methane adsorbs, progressively dissociates, and then reacts with oxygen from dissociated water. The reaction occurs per equations (2.22 – 2.30) below:

$$CH_4 + 2* \rightarrow CH_3* + H* \quad (2.22)$$

$$CH_3* + * \leftrightarrow CH_2* + H* \quad (2.23)$$

$$CH_2* + * \leftrightarrow CH* + H* \quad (2.24)$$

$$CH* + * \leftrightarrow C* + H* \quad (2.25)$$

$$H_2O + 2* \rightarrow OH* + H* \quad (2.26)$$

$$OH* + * \leftrightarrow O* + H* \quad (2.27)$$

$$C* + O* \leftrightarrow CO* + * \quad (2.28)$$

$$CO* \leftrightarrow CO + * \quad (2.29)$$

$$2H* + 2* \leftrightarrow H_2 + 2* \quad (2.30)$$

Note that the asterisk (∗) denotes the adsorption site on the catalytic surface.

The mechanism of steam reforming of higher hydrocarbons has also been reported by Subramani *et al.* [27]. Over nickel catalysts, it is thought to involve adsorption of the hydrocarbon onto the active surface, followed by the formation of C_1 species by the successive α-cleavage of the carbon-carbon bonds. The adsorbed C_1 species are subsequently dehydrogenated on the active surface into carbon atoms. At this stage, carbon atoms may dissolve into the nickel crystal and, when the concentration exceeds saturation, nucleate, and grow as a carbon whisker, typically between the support and the nickel crystal.

The steps involved are reported by Subramani *et al.* [27] from Avcı *et al.* [31],

$$C_nH_m + 2* \rightarrow 2*C_nH_y \quad (2.31)$$

$$2*C_nH_y + * \rightarrow *CH_x + 2X_n - 1H_z \quad (2.32)$$

$$2*C_nH_y \rightarrow n*C \quad (2.33)$$

$$*CH_x \rightarrow *C \quad (2.34)$$

$$*C \leftrightarrow [C, Ni]_{bulk} \rightarrow \text{whisker carbon} \quad (2.35)$$

$$H_2O + * \leftrightarrow *O + H_2 \quad (2.36)$$

$$*CH_x + *O \rightarrow \text{gas} \quad (2.37)$$

$$*C + *O \rightarrow \text{gas} \quad (2.38)$$

$$H_2 + 2* \leftrightarrow 2*H \quad (2.39)$$

Where the asterisk (∗) denotes the adsorption sites on the catalytic surface.

The steam reforming mechanism of over PGM-based catalysts has been reported as being similar to the reaction mechanisms proposed above [27].

2.3.1.3. Partial oxidation and autothermal reforming reactions

2.3.1.3.1. Chemistry and thermodynamics of POX and ATR

Partial oxidation of LPG is a combination of two primary reactions: the partial oxidation of chain alkanes and the partial oxidation of methane. Partial oxidation is a much faster reaction than steam reforming, enabling smaller reactors and higher throughputs [10]. The reaction proceeds per equations (2.40 – 2.41):

$$C_nH_m + {}^{n}/_{2}\,O_2 \rightarrow nCO + {}^{m}/_{2}\,H_2 \mid \Delta H^0_{298K} < 0 \tag{2.40}$$

$$CH_4 + \frac{1}{2}O_2 \rightleftharpoons CO + 2H_2 \mid \Delta H^0_{298K} = -36\ \mathrm{kJ/mol} \tag{2.41}$$

The mechanism of partial oxidation is dependent on a variety of factors. It is possible for the reaction to proceed in the absence of a catalyst, and the reaction mechanism will be different for catalysed reactions.

The exact mechanism of reaction is an open question in partial oxidation research. Some have proposed a direct model, in which the reaction proceeds per reactions (2.40) and (2.41) above, whereas others have proposed an indirect mechanism in which there exist two zones in the reactor, a zone in which CH_4 combusts strongly exothermically at the reactor entrance, and followed by strongly endothermic dry reforming and steam reforming downstream.

The autothermal reforming process combines partial oxidation and steam reforming. Kolb [32] discussed the problem of the development of overheating at the front of the reactor, due to the oxidation reaction occurring faster than the steam reforming reaction. This may lead to the decrease in activity for that volume due to catalyst sintering from excessive heat. Kolb [32] further suggests that the addition of air at low oxygen-to-carbon ratios to prevent coke formation on the catalyst, however, a specific relative quantity is not provided.

2.4. Catalysts for steam reforming

2.4.1. Composition of catalysts

A comprehensive review of reforming catalysts for hydrogen production in fuel cell applications is given by Cheekatamarla *et al.* [33]. They categorise catalysts for reforming light hydrocarbons into two categories: those for reforming methane, and those for reforming ethane, propane, and butane (LPG). For the reforming of methane, it is more common to use nickel and cobalt catalysts, as their activity is sufficient, and their cost is less. For the reforming of LPG, more PGM catalysts were reported.

The relative activities of various precious metals and nickel on alumina supports for the reforming of methane and ethane were reported by Trimm *et al.* [34]. The reported order of activity for methane steam reforming was:

Rh (1.6) > Ru (1.4) > Ni (1) > Pd (0.6) > Pt (0.5)

And for ethane:

Rh (13) > Ru (9.5) > Pd (1.0) ~ Ni (1.0) > Pt (0.9).

The greater activity of rhodium and ruthenium for ethane may be extrapolated to propane and butane. Rhodium is consistently more expensive than ruthenium by a significant margin, and thus ruthenium is preferred despite its marginally lower activity.

Many studies have investigated rhodium on various supports. Italiano *et al.* [35] investigated rhodium dispersed on a series of high surface area mesoporous supports (CeO_2, CeO_2-Al_2O_3, Al_2O_3) and found the activity of all catalysts to be strongly related to catalyst specific surface area and metal dispersion. Mei *et al.* [36] investigated rhodium and iridium dispersed on spinel-type supports, through a combined experimental and theoretical investigation. They found that the strong metal-support interaction greatly improved the stability of the active metal dispersion.

Several studies [37 – 40] have investigated the performance of ruthenium dispersed on various supports in monolith catalysts. Other studies have focused on [41, 42] the effects of different supports and metal cation dopants on the activity and deactivation resistance of the catalysts.

2.4.2. Preparation of catalysts

Traditional methane steam reforming catalysts for industrial production of hydrogen and synthesis gas are based on nickel/nickel oxide or cobalt compositions on refractory alumina or supports such as magnesium alumina spinel, often promoted with alkali or alkaline-earth compounds to accelerate carbon removal [10]. Others include precious metals (Rh, Ru, Pt, Pd, Re) on γ-alumina, particularly ceria [10]. van Niekerk [43] reported that the most used catalysts for steam reforming in industrial settings are nickel or cobalt used as an egg-shell catalyst. The catalysts were prepared by precipitating the active metal salt in the presence of the support material, typically chosen from aluminates, silicates and other metal oxide compounds. van

Niekerk [43] also reported that another common catalyst preparation technique is through wet impregnation.

γ-Alumina is the most common support, because of its low cost, high BET surface area, and thermal stability throughout the steam reforming operating temperature range. However, it has been reported that the acidity of alumina catalysts contributes to the deactivation of the catalyst though catalysing the formation of stable cokes, making spinel supports a common alternative.

2.5. Deactivation of steam reforming catalysts

Catalyst deactivation describes various processes by which catalysts lose their activity and/or selectivity. Catalyst deactivation is a ubiquitous problem and nearly all catalytic processes must address deactivation at some point in the operational lifespan of equipment. There are 6 intrinsic mechanisms of catalyst decay: (1) poisoning, (2) fouling, (3) thermal degradation, (4) vapor compound formation/leaching leading to transport of the active phase from the catalyst, (5) vapor-solid and/or solid-solid reactions, and (6) attrition/crushing [44], as seen in Table 2.3.

Mechanisms 1, 4 and 5 are chemical in nature, and mechanisms 2 and 6 are mechanical in nature. The causes of deactivation are threefold: chemical, mechanical, and thermal.

Table 2.3: Mechanisms of catalyst deactivation, taken from Argyle et al. [44]

Mechanism	***Type***	***Brief definition/description***
Poisoning	Chemical	Strong chemisorption of species on catalytic sites which block sites for catalytic reaction
Fouling	Mechanical	Physical deposition of species from fluid phase onto the catalytic surface and in catalyst pores
Thermal degradation and sintering	Thermal/ Thermo-chemical	Thermally induced loss of catalytic surface area. support area, and active phase-support reactions
Vapour formation	Chemical	Reaction of vapor, support, or promoter with catalytic phase to produce inactive phase
Vapour-solid and solid-solid reactions	Chemical	Reaction of vapor, support, or promoter with catalytic phase to produce inactive phase
Attrition/crushing	Mechanical	Loss of catalytic material due to abrasion; loss of internal surface area due to mechanical-induced crushing of the catalyst particle

It is widely reported that the primary cause of deactivation in steam reforming catalysts is through fouling in the form of carbon deposition/coking [27, 45]. However, depending on reactor operating conditions, other forms of deactivation may also occur. For instance, in reactors operating at high temperature and with high steam-to-carbon (S/C) ratios, sintering is a common form of deactivation.

2.5.1. Coking of steam reforming catalysts

Catalyst deactivation, carbon deposition and carbon deposition on steam reforming catalysts have been reviewed thoroughly in various works [44 – 49]. The most thorough review to date is provided by Argyle *et al.* [44].

Different kinds of carbonaceous deposits may form through different mechanisms and at different reaction conditions. The terms coke and carbon are often used interchangeably, though they are equally often used to differentiate different kinds of deposition; with coke referring to the product of cracking and condensation of heavier hydrocarbons, and carbon referring to the product of CO disproportionation [44].

The structure and location of a coke/carbon will have more impact than quantity on catalyst deactivation [50]. Different kinds of coke that vary in morphology and reactivity are formed through different mechanisms. Table 2.4 provides an overview of the different kinds of carbon that form from the decomposition of CO on a metallic surface. Note that the final column provides the temperature at which a peak is observed in TPR.

Table 2.4: Forms and reactivities of carbon species formed by decomposition of CO on an active metal surface, adapted from Argyle et al. [44]

Structural type	***Designation***	***Temp. Formed (°C)***	***Peak temp observed in reaction with H_2 (°C)***
Adsorbed, atomic (surface carbide)	C_α	200-400	200
Polymeric, amorphous films or filaments	C_β	250-500	400
Vermicular filaments, fibres and/or whiskers	C_v	300-1000	400-600
Metal carbide (bulk)	C_γ	150-250	275
Graphitic (crystalline) platelets or films	C_c	500-550	550-850

Different kinds of carbon can convert to other kinds under certain conditions. For instance more reactive carbons formed at low temperatures, such as adsorbed or polymeric carbons, can convert at high temperatures to less reactive graphic forms, which are more resistant to removal through gasification [45]. The process by which carbon laydown resulting from CO disproportionation can occur and transform is depicted in Figure 2.4.

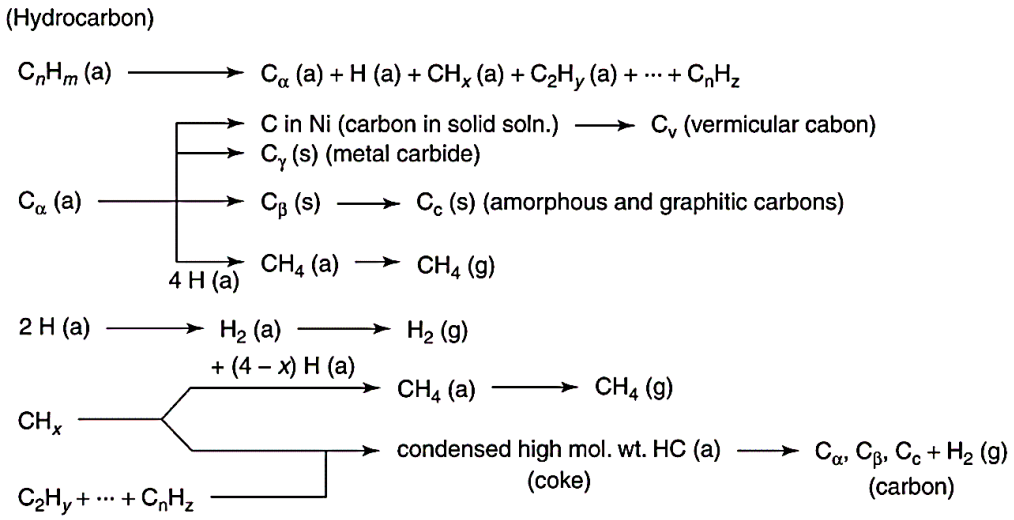

Figure 2.4: Formation and transformation of coke on metal surfaces, taken from Argyle et al. [44] (a, g, and s refer to adsorbed, gaseous and solid states, respectively)

Vermicular carbon forms when adsorbed carbon diffuses into the metal crystal, reaches saturation, and starts depositing between the metal and the support. Thermal or mechanical shock can then dislodge the metal crystal, leading to the loss of those active sites. Other than CO disproportionation, other carbon forms that affect steam reforming catalysts are an encapsulating film and pyrolytic carbon. Encapsulating films form through slow polymerisation of hydrocarbon radicals on the catalytic surface. Pyrolytic carbon forms from cracking, especially of higher hydrocarbons such as propane and butane. It is also reported that acidic catalyst supports aid in the formation of cokes by acting as a carbocation generating agent. The conditions and mechanisms of carbon species affecting steam reforming on nickel catalysts are summarised in Table 2.5. This may reasonably be extrapolated to other metals.

Table 2.5: Carbon species formed in steam reforming of hydrocarbons on nickel catalysts, taken from Argyle et al. [44]

Attribute	***Encapsulating film***	***Whisker-Like***	***Pyrolytic carbon***
Mechanism of formation	Slow polymerisation of C_nH_m radicals on metal surface, into encapsulating film	Diffusion of C though metal crystal, nucleation, and whisker growth with metal crystal at top	Thermal cracking of hydrocarbon; deposition of C precursors on catalyst
Effects	Progressive deactivation	No deactivation of Ni surface. Breakdown of catalyst and increasing ΔP	Encapsulation of catalyst particle; deactivation and increasing ΔP
Temp. Range (°C)	<500	>450	>600
Critical parameters	Low temperature, low H_2O/C_nH_m, low H_2/C_nH_m, aromatic feed	High temperature, low H_2O/C_nH_m, no enhanced H_2O adsorption, low activity, aromatic feed	High temperature, high void fraction, low H_2O/C_nH_m, high pressure, acidic catalyst

The temperature range at which the different kinds of carbon formation occur means that at normal operating temperature (800 – 850°C), whisker-like and pyrolytic carbons are more likely to form.

2.5.2. Chemistry of carbon deposition

Coking in LPG steam reforming will occur due to three types of reactions: hydrocarbon cracking (2.42 – 2.45), the Boudouard reaction (CO disproportionation) (2.46), and CO reduction (2.47).

$$CH_4 \rightarrow C + 2H_2 \mid \Delta H^0_{298K} = 74.6\,kJ/mol \quad (2.42)$$

$$C_2H_6 \rightarrow 3H_3 + 2C \mid \Delta H^0_{298K} - 84.7\,kJ/mol \quad (2.43)$$

$$C_3H_8 \rightarrow 4H_2 + 3C \mid \Delta H^0_{298K} = 103.8\,kJ/mol \quad (2.44)$$

$$n\text{-}C_4H_{10} \rightarrow 9H_2 + 4C \mid \Delta H^0_{298K} = 126.2\,kJ/mol \quad (2.45)$$

$$2CO \rightarrow CO_2 + C \mid \Delta H^0_{298K} = -172.4\,kJ/mol \quad (2.46)$$

$$CO + H_2 \rightleftharpoons C + H_2O \mid \Delta H^0_{298K} = -131.3\,kJ/mol \quad (2.47)$$

Of these reactions, hydrocarbon cracking and CO disproportionation are believed to contribute most to carbon laydown.

2.5.3. Strategies for mitigating deactivation

Various strategies for mitigating deactivation due to carbon deposition have been proposed and tested. Subramani *et al.* [27] list several approaches for industrial steam reforming on nickel:

- Use of high steam-to-carbon ratio
- Catalyst with smaller crystal sizes
- Addition of promoters
- Use of noble metals instead of nickel (or other base metals)
- Alloying of nickel with other base metals or noble metals
- Passivation, with sulfur, of nickel surfaces that favour carbon formation
- Use of a pre-reformer
- Conducting reaction under oxidative conditions or oxidative steam reforming

Industrially, potassium hydroxide is added as a promoter to nickel based catalysts as a means of mitigating deactivation. This mitigates the acidity of the support (generally Al_2O_3), and catalyses the gasification reaction [44]. However, it has been documented that potassium hydroxide is volatile under steam reforming reaction conditions, making this a less viable mitigation strategy in non-industrial application settings.

It has been observed that noble metals such as Pd, Pt, Rh, Ru and Ir are relatively more resistant to coking deactivation in comparison to Ni, and it has been proposed that this is due to the lower solubility of carbon in these metals [51].

Another strategy has been the use of alternative supports such as magnesium aluminate spinel [36], or rare earth metal oxides [52, 53]. There are several mechanisms by which this may prevent carbon deposition: stronger metal-support interaction leads to greater resistance to whisker formation and promotes better dispersion, and alkalinity of the support promotes gasification. Specifically in the case of ceria [42], it is believed that enhanced oxygen mobility further enables gasification.

Kolb [32] suggests the introduction of small quantities of air into the steam reformer feed as a mitigate carbon deposition, however, this claim cannot be corroborated from other sources explicitly.

3. Experimental

3.1. Catalyst preparation

100 g of a 5 wt% Ru/Al_2O_3 (5 g Ru, 95 g Al_2O_3) catalyst was prepared by wet impregnation, as described below. Assuming a salt metal content of 40%, based on the composition suggested on the packaging, a total of 12.5 grams of ruthenium (III) chloride hydrate (Sigma-Aldrich: 40 wt% Ru salt) was dissolved in an appropriate quantity of de-ionised water which was subsequently added drop-wise to 95 g of commercially available γ-alumina powder (Sasol PURALOX SCCa-150/200 : 185 – 215 m^2/g , average particle diameter of 150 μm), with constant stirring to form a well-mixed paste. Subsequently, this paste was dried and calcined in static air to form the respective metal oxide. The procedure involved heating the respective impregnated alumina sample from 25°C to 90°C at 1°C/min, holding at that temperature for 1 h, heating further to 120°C at a rate of 1°C/min and holding for 30 min, and then heating further to 800°C at a rate of 2°C/min, and holding at the elevated temperature for 5 h, before cooling again to room temperature.

For the purposes of gathering the most useful data for interpreting the physicochemical properties of the fresh catalyst, two samples of catalyst underwent in-situ treatment in the reactor prior to characterisation, following the processes described in Section 3.2.5.1. The catalyst which was untreated is referred to as **F**resh **C**alcined **Cat**alyst (FC-Cat), the catalyst which was reduced is referred to as **C**alcined/**R**educed **Cat**alyst (CR-Cat), and the catalyst which was reduced and steamed is referred to as **C**alcined/**R**educed/**S**teamed **Cat**alyst (CRS-Cat). Instead of the introduction of dry feed, the samples were allowed to cool to room temperature in flowing nitrogen (400 sccm). These are collectively referred to as the fresh catalyst samples to differentiate them from the spent catalyst samples.

3.2. Reforming reactor system

3.2.1. Reactor system setup

The reactor system comprises of a fixed-bed reactor tube held in an electrically-heated furnace block with separate systems for gas (C_3H_8, N_2, Ar, H_2, air – mass flow controllers) and liquid (water – HPLC pump) feed streams. Post-reactor, a condenser/catch-pot system serves to knock-out water prior to the dry effluent stream proceeds to on-line chromatographic analysis. A piping and instrumentation diagram is provided in Figure 3.1 below:

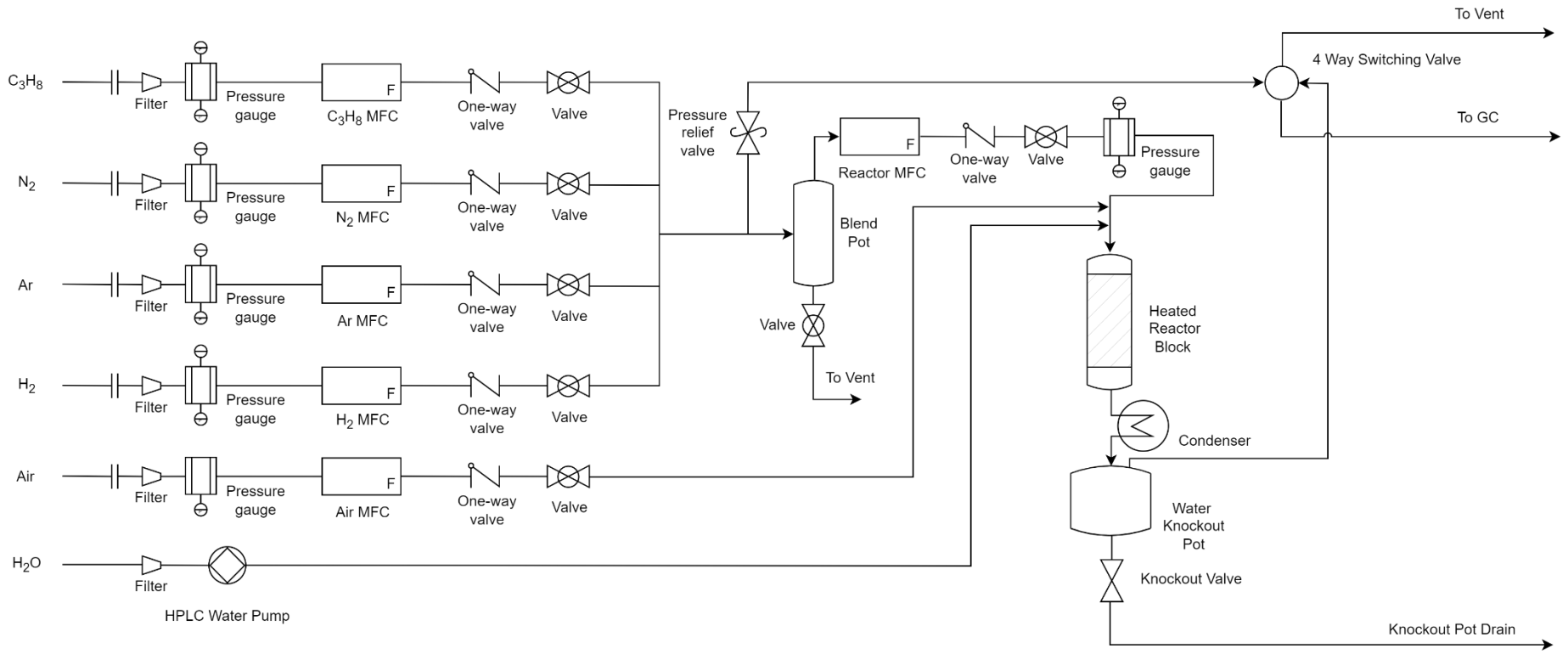

Figure 3.1: Piping and Instrumentation Diagram of the propane steam reforming reactor configuration

3.2.2. Feed gas and liquid delivery

All dry gasses were supplied by Air Liquide South Africa or Air Products South Africa, except for propane, which was supplied by Afrox.

The flowrates of each gas into the system were regulated using individual Brookes Instruments mass flow controllers (MFCs, T97692 series) that were calibrated for standard temperature and pressure conditions (STP). Gasses, other than air, were supplied in their required proportions to a blend pot in excess of that directed to the reactor, such that the excess mixed gas stream (bypass stream) could be analysed, via the online gas chromatograph, as required throughout the experiment for confirmation of the dry feed gas composition. The flowrate of air is controlled by a separate MFC which connected directly to the reactor (at the entrance to the internal packed SiC bed), as a precaution to avoid a potentially flammable/explosive mixture of gasses in the relatively large volume gas blending pot.

Deionised water was fed directly into the reactor tube using an HPLC pump.

3.2.3. Temperature profiles through the reactor

As the reactor tube used for the experiments did not have a fixed thermowell, the operating temperature profile was determined in advance by inserting an $1/8^{th}$ inch diameter stainless steel tube via the bottom of the reactor, filling the remaining reactor annular space with SiC and inserting a thermocouple into the stainless-steel tube with the reactor furnace temperature controllers set to 750°C.

The reactor temperature profiles determined in this manner are shown in Figure 3.2 for conditions of both a stagnant tube (no flow) and water flow at typical reaction conditions (since steam was the dominant feed component and the component with the highest heat capacity). It can be seen from Figure 3.2 that, in both circumstances, the temperature profile was constant at the set-point throughout the position of the catalyst bed. It was further observed that, in the case of water feed, the fully developed temperature profile was shifted slightly further down the reactor packing, as might be expected due to the heat required to boil the water feed and raise the resulting steam to temperature at the entrance, and the additional heat carried by the steam likewise extended the heated zone towards the reactor exit.

Figure 3.2 confirms the reactor temperature profile as per the set-point, inclusive of vaporising water and raising steam prior to the catalyst bed. However, the propane steam reforming heat of reaction is some 6-fold greater than that required for raising steam (assuming complete propane conversion to syngas) under the standard reaction conditions of this study. Although no temperature profile could be determined with reforming in progress, reactor furnace readings did not indicate temperatures lower than the set-point other than when furnace heating cartridges failed – and for which experiments were suspended pending repairs.

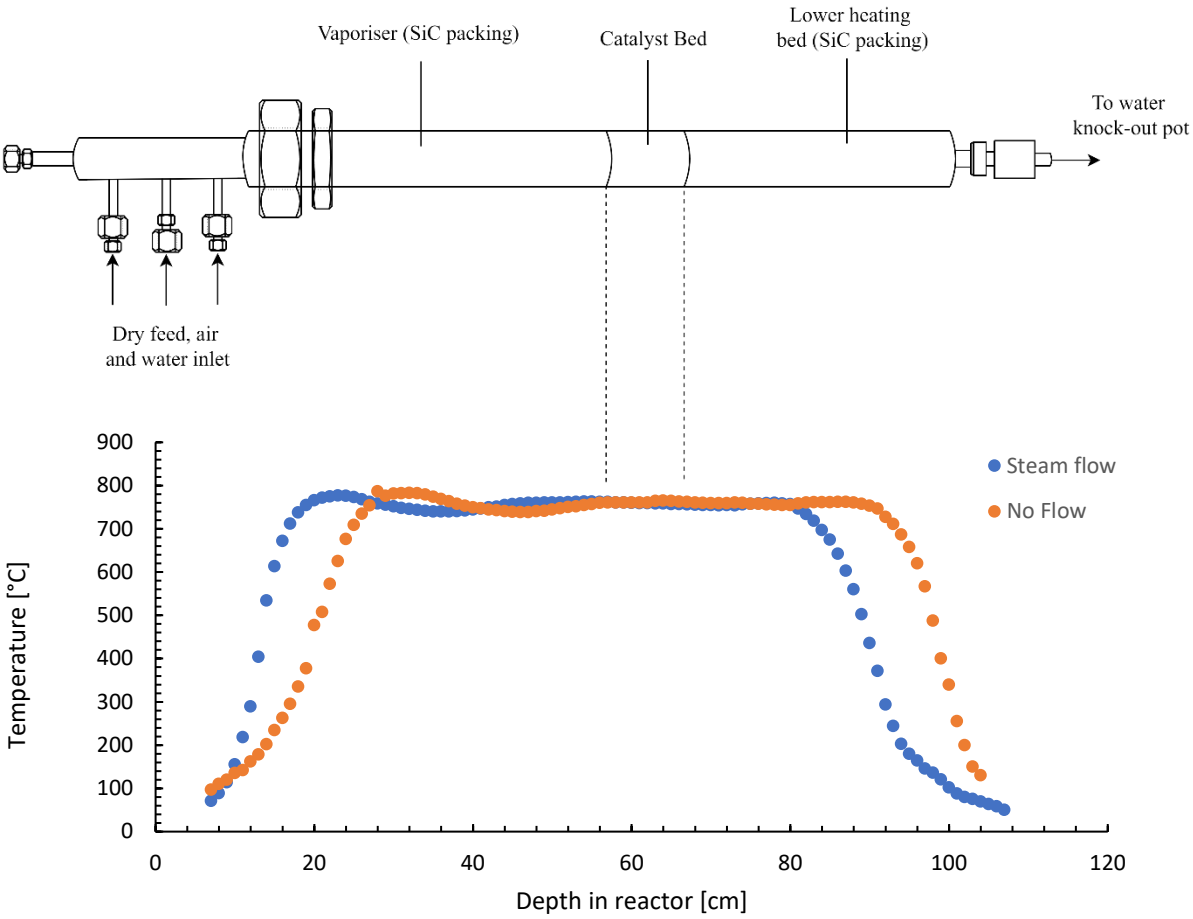

Figure 3.2: Temperature profile through reactor with and without steam flow indicating catalyst bed position

3.2.4. Reactor packing and assembly

When in use for experiments, the entire reactor volume was filled with a granular packing comprising of three distinct zones, *viz*., from the top, the vaporiser, catalyst bed and lower heating zones, with the position of the catalyst bed determined from the reactor temperature profile (Figure 3.2). The catalyst bed itself was comprised of 1 g of catalyst (particle size < 250 µm) mixed with 12 g SiC (average particle size 300 µm) such that the catalyst could be retrieved post-reaction from the packing by sieving.

A small layer of quartz wool was used to cover the bottom exit of the reactor and the lower heating zone was packed with 1000 µm SiC to the level necessary for correct placement of the catalyst bed within the reactor tube, followed by another layer of quartz wool, the catalyst/SiC mixture, a further layer of quartz wool and, finally, additional 1000 µm SiC to fill the reactor to above the level of the air inlet. The reactor tube body was then joined to the reactor head via a Swagelok VCR gasket assembly.

The completely assembled reactor was placed into position in the furnace block and the feed and effluent lines were connected via VCR couplings, and the reactor pressurized statically to 5 bar_g with nitrogen. The system was deemed leak-tight if no measurable pressure drop was observed over 1 h.

3.2.5. Reactor operation

3.2.5.1. Start-up procedure

Two differing start-up procedures were followed. One in which the dry feed was introduced directly to the catalyst following reduction, and another in which the reduced catalyst was steamed for 24 h prior to the start of the dry feed introduction.

3.2.5.1.1. Reduced catalyst start-up procedure

The experiment was started by reducing the 1 g of catalyst in a flowrate of 5% H_2 (20 sccm) in N_2 (400 sccm) while the furnace was heated to 750°C over 12 h. Reduction was completed by flowing 100 % H_2 (20 sccm) over the catalyst for 1 h, followed by 100% nitrogen (400 sccm) to displace the hydrogen from the system. At this point, the dry gas feed mixture was introduced into the blending pot via the propane and argon mass flow controllers and vented through the bypass line via a back-pressure regulator. The water pump was started (1.23 ml/min) and allowed to pump for 10 min (the amount of time required from initiating the water flowrate to steam exiting the reactor - determined by the temperature rise in the reactor exit lines), prior to the initiation of the dry feed flowrate to the reactor. The dry feed was comprised of propane (127 sccm) and argon (14.1 sccm). The total intended wet SGHSV was 100 000 ml/(gr.hr).

3.2.5.1.2. Steamed catalyst start-up procedure

The experiment was started by reducing the catalyst in a flowrate of 5% H_2 (20 sccm) in N_2 (400 sccm) while the furnace was heated to 750°C over 12 h. Reduction was completed by flowing 100% H_2 (20 sccm) over the catalyst for 1 h. The catalyst was then steamed in the presence of air for 24 h by introducing 1.227 ml/min water feed and 1.43 sccm air. After the catalyst had been steamed for 24 h, the dry feed was introduced in addition. The dry feed was comprised of propane (127 sccm) and argon (14.1 sccm). The total intended wet SGHSV was 100 000 ml/(gr.hr).

3.2.5.2. On-line procedures

When changes to a reaction condition were made,

i. Changing the S/C ratio
   - i.i. Decreasing the S/C ratio
     - i.i.i. The HPLC pump flowrate was adjusted
     - i.i.ii. The dry gas feed was made up with nitrogen to maintain the same space velocity. The reactor MFC was adjusted in accordance with the changing flowrate and the new gas correction factor
   - i.ii. Increasing the S/C ratio

i.ii.i. The HPLC pump flowrate was increased. It was not possible to retain the same space velocity

ii. Changing the flowrate of air

ii.i. The air MFC was switched off/on at the appropriate value without adjustment of other flows since in all cases the air flow rate was small by comparison (below 3% of dry gas flowrate).

3.2.5.3. Shut down procedure

The objective of the shut down procedure was to terminate the flow of reagents to the catalyst bed, then to introduce an inert flowrate so that the catalyst could be recovered in the state that it was at the termination of the experiment.

i. When shutting down an experiment, the dry gas feed was terminated by switching off the propane, argon, and air mass flow controllers.
ii. The HPLC pump was switched off to terminate the flow of steam.
iii. Nitrogen flow at 400 sccm was started to completely remove any reactants from the system.
iv. Heating was switched off by switching off the reactor furnace and allowing approximately 12 h for the reactor to cool down to room temperature under flowing nitrogen.

However, it was found that in the event of significant coking, which led to significant pressure build-up in the reactor (>2 bar_g), it was challenging to remove the catalyst and surrounding SiC from the reactor since the coke 'cemented' the packed contents inside of the reactor. In this event, steam and air were flowed over the catalyst at 750°C until the pressure build-up in the reactor was less than 2 bar_g, following which the system was cooled to room temperature under flowing nitrogen as above.

3.2.5.4. Catalyst recovery

Following the termination of an experiment and the cooling of the reactor tube to room-temperature under a flow of nitrogen, the reactor tube was disconnected from the gas inlets and removed from the furnace. SiC was removed until the top layer of quartz wool was exposed. The quartz wool was then removed, and the catalyst and SiC mixture was removed and recovered.

For characterization, the catalyst and SiC mixture was sieved using a 250 µm mesh, to remove as much of the SiC as possible. Since the SiC was previously sieved to remove all particles < 250 µm, the catalyst could then be recovered with minimal contamination.

3.2.6. Sizing and calibration of MFCs

Brookes Instruments Smart mass flow controllers were used to synthesise a gas mixture to perform calibration of the GC, as well as to provide a steady flowrate of reactants to the reactor. Mass flow controllers were selected to maintain a wet SGHSV of 100 000 ml/(g.hr).

Whereas propane, argon, air, hydrogen and nitrogen were used in experiments and their MFCs were part of the reforming test unit (see Figure 3.1), the CO, CO_2 and CH_4 MFC from other

equipment were used for gas chromatographic calibrations and C_2H_4 and C_2H_6 chromatographic calibrations were performed using MFCs used for other components. Table 3.1 indicates the specifications of all the mass flow controllers used in the experiments and for calibrations, with flowrates normalised to STP.

Table 3.1: Mass Flow Controller Specifications

MFC	*Type*	*Specified flowrate*	*Calibration Compound*	*5-95% flowrate (STP)*
Reactor	N_2	0 – 1000 ml/min	N_2	61.5 – 1030 ml/min
N_2	CH4	0 – 1000 ml/min	N_2	69.2 – 1280 ml/min
H_2	H2	0 – 300 ml/min	H_2	19.0 – 287 ml/min
CO_2	CO_2	0 – 300 ml/min	CO_2	17.9 – 289 ml/min
CO	N2	0 – 400 ml/min	CO	25.5 – 399 ml/min
CH_4	H2	0 – 100 ml/min	CH_4	9.11 – 75.1 ml/min*
C_3H_8	CH4	0 – 1000 ml/min	C_3H_8	13.4 – 436 ml/min
Ar	Ar	0 – 30 ml/min	Ar	1.21 – 25.8 ml/min
Air	Ar	0 – 30 ml/min	Air	0.28 – 4.21 ml/min

*10-95%

When the reactor was running, the individual component MFCs were set to 105% of their intended flowrate, and the reactor MFC was used to provide a steady flowrate of the reactant mixture, consisting of argon and propane. Gas factors were used to determine the appropriate setting on the reactor mass flow controller.

3.3. Gas chromatographic configuration and calibration

As the Agilent 490 Micro-GC used in this study makes use of thermal conductivity detectors (TCDs), and the reformate product from the reactor system contained both argon and hydrogen, different carrier gases were required in the various analytical columns for complete reformate product stream analysis. Thus, hydrogen was analysed in a column using argon as a carrier gas, and argon was analysed in a column using hydrogen as a carrier gas. The columns which were used in the system are provided in Table 3.2.

Table 3.2: Specifications of columns used in Agilent CP-490 Micro-GC system

	Injector	*Length*	*Column Type*	*Carrier gas*	*Backflush*
Channel 1	Heated	10 m	5A Molsieve column	Argon	Yes
Channel 2	Heated	20 m	5A Molsieve Column	Hydrogen	Yes
Channel 3	Heated	10 m	PPQ column (coated)	Hydrogen	No

3.3.1. Calibrating the back flush settings

A backflush was a technique used to prevent later-eluting compounds from reaching the analytical column and detector – so preventing contamination of the analytical column and reducing analytical time.

The backflush system consists of a guard pre-column and an analytical column, in series. The columns are coupled at a 'pressure point', where it was possible to reverse the carrier gas flow direction through the pre-column. When all compounds desired to be quantified have passed through the pre-column, the backflush valve was engaged to reverse the flow in the pre-column and flush any remaining components to vent. In the analytical column, where the flow was not reversed, the chromatographic separation proceeds unaffected.

In this study, backflush was used only for the MS5 columns, which are adversely affected by water, CO_2, and heavy hydrocarbons. Detailed procedures regarding the calibration may be found in Appendix II – Backflush Calibration.

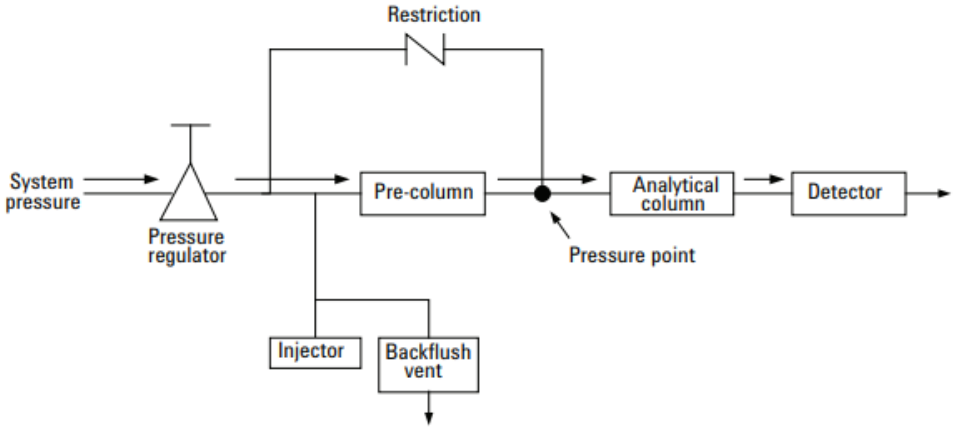

Figure 3.3: Normal GC flows, taken from Agilent [54]

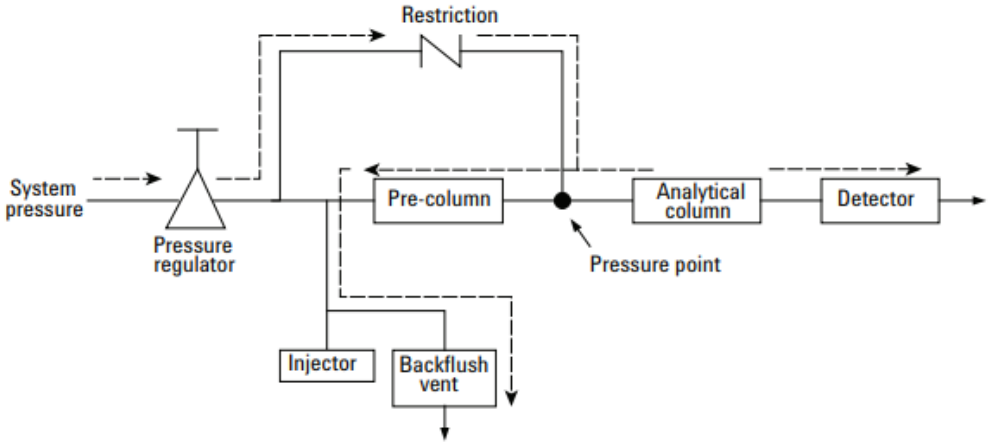

Figure 3.4: Backflush GC flows, taken from Agilent [54]

3.3.2. Calibrating the RRFs for the GC

GC chromatogram peak areas were related to volumetric flowrate of individual gasses via the use of an internal standard gas (Ar) of known volumetric flowrate, and the use of a compound specific relative response factor (RRF).

$$\mathrm{RRF_i} = \frac{\left(\frac{\mathrm{F_i}}{\mathrm{F_{Ar}}}\right)}{\left(\frac{\mathrm{Area_i}}{\mathrm{Area_{Ar}}}\right)} \tag{3.1}$$

Where RRF_i represents the measured relative response factor for component i, F_i represents the flowrate of component i, F_{Ar} represents the flow of argon (the internal standard), $Area_i$ represents the chromatographic area of component i, and $Area_{Ar}$ represents the chromatographic area of argon (the internal standard).

To determine the RRF for a species, a series of calibrated gas mixtures were created using the available calibrated MFCs, with differing concentrations of the components corresponding to differing conversions of propane. The conversions ranged from 0–70%. The chromatograms were processed, and the areas and volumes were used to produce a graph of $\frac{F_i}{F_{Ar}}$ vs. $\frac{Area_i}{Area_{Ar}}$, with the gradient of the graph taken as the relative response factor for that component. A sample graph is provided below in Figure 3.5, as was used in this study.

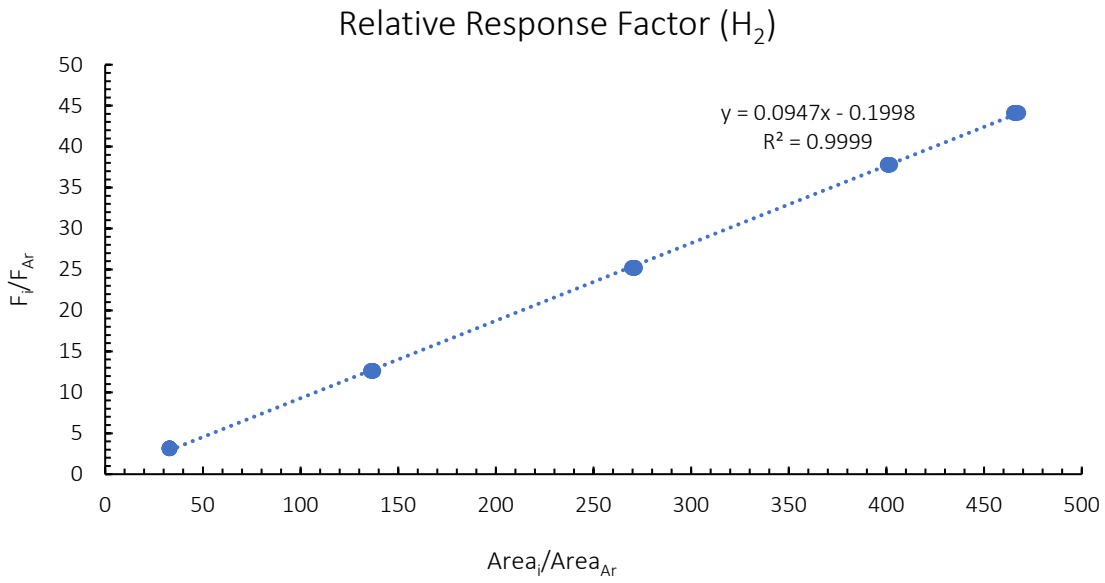

Figure 3.5: Sample Relative Response Factor graph for Hydrogen as used in this study

The RRFs for the components are presented in Table 3.3 and the remaining calibration curves are provided in Appendix II: Relative Response Factor Calibration Data.

Table 3.3: Relative Response Factors for components on GC columns

Component	*Channel*	*Relative Response Factor*
H_2	1	0.0947
CH_4	1	0.383
CO	1	1.16
N_2	1	0.920
CH_4	2	1.11
CO	2	1.24
N_2	2	1.01
C_3H_8	3	0.0993
C_3H_6	3	0.0993 *
CO_2	3	0.132
CH_4	3	0.141
C_2H_4	3	0.125
C_2H_6	3	0.130

*Taken to be the same as C_3H_8

3.3.3. Chromatographic Data Workup

From equation (3.1) above, the following equation was used to determine the flowrate for each of the components:

$$\mathrm{F_i} = \mathrm{F_{Ar}} \cdot \mathrm{RRF_i} \cdot \left(\frac{\mathrm{Area_i}}{\mathrm{Area_{Ar}}}\right) \tag{3.2}$$

Where F_i represents the flowrate of component i, F_{Ar} represents the flowrate of argon (the internal standard), RRF_i represents the measured relative response factor for component i, $Area_i$ represents the chromatographic area of component i, and $Area_{Ar}$ represents the chromatographic area of argon (the internal standard).

Three different calculations were performed for conversion, a propane conversion (3.3), a C_3 conversion (3.4) and a 'total-hydrocarbon-conversion' (THC) (3.5).

Although propane conversion (3.3) was an appropriate measure of catalytic performance, the difficulty in consistently separating propane and propene chromatographic peaks made accurate measurement of propane conversion unreliable. Propane conversion was defined as follows:

$$\mathrm{X_{C_3H_8}} = \frac{\mathrm{n_{C_3H_8,i}} - \mathrm{n_{C_3H_8,e}}}{\mathrm{n_{C_3H_8,i}}} \tag{3.3}$$

Where $\mathrm{X_{C_3H_8}}$ represents propane conversion, $\mathrm{n_{C_3H_8,i}}$ represents the amount of moles of propane in the feed, and $\mathrm{n_{C_3H_8,e}}$ represents the amount of moles of propane in the product.

Consequently, C_3 conversion (3.4) was calculated to determine what proportion of propane was being cracked or reformed, as opposed to being dehydrogenated. C_3 conversion was defined as follows:

$$X_{C_3} = \frac{n_{C_3H_8,i} - n_{C_3H_8,e} - n_{C_3H_6,e}}{n_{C_3H_8,i}} \tag{3.4}$$

Where X_{C_3} represents C_3 conversion, $n_{C_3H_8,i}$ represents the amount of moles of propane in the feed, and $n_{C_3H_8,e}$ and $n_{C_3H_6,e}$ represent the amount of moles of propane and propene in the product, respectively.

Total hydrocarbon conversion (3.5) measured what proportion of carbon entering as propane was reformed to CO_x products as opposed to remaining unreacted or being cracked to alkanes or alkenes.

$$X_{THC} = \frac{3 \cdot n_{C_3H_8,i} - 3 \cdot n_{C_3H_8,e} - 3 \cdot n_{C_3H_6,e} - 2 \cdot n_{C_2H_6,e} - 2 \cdot n_{C_2H_4,e} - 1 \cdot n_{CH_4,e}}{3 \cdot n_{C_3H_8,i}} \tag{3.5}$$

Where X_{THC} represents total hydrocarbon conversion, $n_{C_3H_8,i}$ represents the amount of moles of propane in the feed, and $n_{C_3H_8,e}$, $n_{C_3H_6,e}$, $n_{C_2H_6,e}$, $n_{C_2H_4,e}$ and $n_{CH_4,e}$ represent the amount of moles of propane, propene, ethane, ethene and methane in the product, respectively. The coefficient next to the amount of moles of each species represents the number of carbon atoms in that particular species.

Selectivity towards species containing carbon was defined as the concentration of each species in the reactor product over the concentration of all species containing carbon, multiplied by factor i which is the number of carbon atoms in the corresponding species.

$$S_{C_n} = \frac{n_{C_iH_{j,e}} \cdot i}{\sum n_{C_iH_{j,e}} \cdot i} \tag{3.6}$$

Where S_{C_n} represents selectivity towards a particular class of alkanes, $n_{C_iH_{j,e}}$ represents the amount of moles of a particular species, and i and j represent the number of carbon and hydrogen atoms in that species.

Thus, selectivity towards C_1 alkane products is defined as:

$$S_{C_1} = \frac{n_{CH_4,e}}{n_{CH_4,e} + n_{CO,e} + n_{CO_2,e} + 2 \cdot n_{C_2H_4,e} + 2 \cdot n_{C_2H_6,e} + 3 \cdot n_{C_3H_6,e}} \tag{3.7}$$

Where S_{C_1} represents the selectivity towards C_1 alkanes (methane), and $n_{CH_4,e}$, $n_{CO,e}$, $n_{CO_2,e}$, $n_{C_2H_4,e}$, $n_{C_2H_6,e}$ and $n_{C_3H_6,e}$ represent the amount of moles of methane, carbon monoxide, carbon dioxide, ethene, ethane and propene in the product, respectively. The coefficient next to the amount of moles in a species represents the number of atoms of carbon in that species.

Selectivity towards C_2 products was defined as:

$$S_{C_2} = \frac{2 \cdot n_{C_2H_4,e} + 2 \cdot n_{C_2H_6,e}}{n_{CH_4,e} + n_{CO,e} + n_{CO_2,e} + 2 \cdot n_{C_2H_4,e} + 2 \cdot n_{C_2H_6,e} + 3 \cdot n_{C_3H_6,e}} \quad (3.8)$$

Where S_{C_2} represents the selectivity towards C_2 alkanes (ethene and ethane), and $n_{C_2H_4,e}$, $n_{C_2H_6,e}$, $n_{CH_4,e}$, $n_{CO,e}$, $n_{CO_2,e}$ and $n_{C_3H_6,e}$ represent the amount of moles of ethene, ethane, methane, carbon monoxide, carbon dioxide, and propene in the product, respectively. The coefficient next to the amount of moles of each species represents the number of carbon atoms in that species.

Propene was defined as a C_3 product. Therefore, selectivity towards C_3 products was defined as:

$$S_{C_3} = \frac{3 \cdot n_{C_3H_6,e}}{n_{CH_4,e} + n_{CO,e} + n_{CO_2,e} + 2 \cdot n_{C_2H_4,e} + 2 \cdot n_{C_2H_6,e} + 3 \cdot n_{C_3H_6,e}} \quad (3.9)$$

Where S_{C_3} represents the selectivity towards C_3 alkanes (propene), and $n_{C_3H_6,e}$, $n_{CH_4,e}$, $n_{CO,e}$, $n_{CO_2,e}$, $n_{C_2H_4,e}$ and $n_{C_2H_6,e}$ represent the amount of moles of propene, methane, carbon monoxide, carbon dioxide, ethene, and ethane in the product, respectively. The coefficient next to the amount of moles of each species represents the number of carbon atoms in that species.

Selectivity towards CO_x products is defined as:

$$S_{CO_x} = \frac{n_{CO,e} + n_{CO_2,e}}{n_{CH_4,e} + n_{CO,e} + n_{CO_2,e} + 2 \cdot n_{C_2H_4,e} + 2 \cdot n_{C_2H_6,e} + 3 \cdot n_{C_3H_6,e}} \quad (3.10)$$

Where S_{CO_x}represents the selectivity towards CO_x products, and $n_{CO,e}$, $n_{CO_2,e}$, $n_{CH_4,e}$, $n_{C_2H_4,e}$, $n_{C_2H_6,e}$ and $n_{C_3H_6,e}$ represent the amount of moles of carbon monoxide, carbon dioxide, methane, ethene, ethane and propene in the product, respectively. The coefficients next to the amount of moles of a species represents the number of carbon atoms in that species.

Selectivity towards hydrogen is defined as the concentration of hydrogen in the reactor effluent over the concentration of all products containing hydrogen, multiplied by factor j which is the number of hydrogen atoms in the corresponding molecule. Measurement accuracy for this selectivity was found to be less reliable and is consequently not reported in the results.

$$S_{H_2} = \frac{n_{H_2,e}}{n_{H_2,e} + \frac{j}{2} \cdot n_{C_iH_j,e}} \quad (3.11)$$

Where S_{H_2}represents the selectivity towards hydrogen, $n_{H_2,e}$ represents the amount of moles of hydrogen in the product, $n_{C_iH_j,e}$ represents the amount of moles of a particular species in the product, and i and j represent the number of atoms of carbon and hydrogen in that species, respectively.

Thus, selectivity towards hydrogen is defined as:

$$S_{H_2} = \frac{n_{H_2,e}}{n_{H_2,e} + 2 \cdot n_{CH_4,e} + 2 \cdot n_{C_2H_4,e} + 3 \cdot n_{C_2H_6,e} + 3 \cdot n_{C_3H_6,e}} \quad (3.12)$$

Where S_{H_2} represent the selectivity of hydrogen, and $n_{H_2,e}$, $n_{CH_4,e}$, $n_{C_2H_4,e}$, $n_{C_2H_6,e}$ and $n_{C_3H_6,e}$ represent the amount of moles of hydrogen, methane, ethene, ethane and propene in the product, respectively. The coefficient next to the amount of moles of each species represents the number of hydrogen atoms contained in that species, divided by two.

3.4. Catalyst characterisation

The following section details the characterisation techniques that were used in this study. Note the different samples of catalyst as described in Section 3.1.

3.4.1. Thermogravimetric measurements

Thermogravimetric and differential thermogravimetric analysis (TGA-DTG), and differential thermal analysis (DTA) were performed on the fresh catalyst, as well as spent catalyst, using a TA Instruments Discovery Series SDT650 instrument controlled by TA instruments v4.2.1.36612 software. All analyses were performed in 90 µL alumina crucibles using approximately 10 – 20 mg of sample. The TA Instruments Trios Software was used to analyse the DTG curves and percentage weight losses.

For the fresh catalyst, these thermogravimetric measurements were used to determine the temperature of reduction of the catalyst, as well as weight loss due to physisorbed water and decomposition of precursor compounds. Temperature-Programmed-Reduction (TPR) was performed in an H_2 atmosphere at a flowrate of 200 sccm, and at a heating rate of 10°C/min, from room temperature to 800°C. Temperature-Programmed-Oxidation (TPO) was performed in an air atmosphere at a flowrate of 10 sccm, and at a heating rate of 3°C/min, with additional replications at 10°C/min.

For the recovered spent catalyst, these thermogravimetric measurements were used to quantify and characterise coke formation. TPO was performed in an air atmosphere at a flowrate of 10 sccm, and at a heating rate of 3°C/min, with additional replications at 10°C/min. Coking may be classified into two distinct kinds: coke which is volatilized, and carbon which is only removed at a higher temperature through burning [55].

3.4.2. Brunauer-Emmett-Teller (BET) Surface Area and Barret-Joyner-Halenda (BJH) Pore Size Distribution and Volume Analysis

A Micromeritics TriStar II Surface Area and Porosity Analyser was used to conduct N_2 physisorption to perform a Brunauer-Emmett-Teller (BET) surface area analysis and Barrett-Joyner-Halenda (BJH) pore size distribution and volume analysis.

Analysis was performed using approximately 200 mg of catalyst. The sample was loaded into a labelled sample tube and degassed at 200°C for at least 3 h in a VacPrep 061 to remove physisorbed water and as much physisorbed gas as possible. The N_2 adsorption-desorption isotherms were measured at -196°C. Micromeritics TriStar II 3020 software (Micromeritics Instrument Corporation, 2007) was used to fit the BET and BJH equations. As the fitting strategy significantly affected the results obtained from the analysis, the data points were selected carefully. For the BET analysis, points were selected visually from the linear range of the BET surface area plot, and for the BJH analysis, data points were selected visually from the linear range of the t-plot.

3.4.3. X-ray Diffraction (XRD)

X-ray diffraction was used to characterise the crystallinity, atomic structure, and phase of the fresh and recovered catalyst samples. Powder diffractograms of the samples were recorded using a Bruker D8 Advance Laboratory X-ray Diffractometer, equipped with a cobalt source ($\lambda_{K\alpha1}$ = 0.178897 nm, slit width = 1.0 mm) and a position-sensitive detector (LYNXEYE XE, Bruker AXS) at 20 kV and 5 mA.

The reference patterns from the International Centre for Diffraction Data (2008) (ICCD) were used to identify the compounds and phases contained within the samples. The reference patterns were matched using the Diffrac.Eva software. Furthermore, the mean crystallite sizes were determined from the X-ray line broadening of the reflection peak using the Scherrer equation [56]

$$d = \frac{K\lambda}{\beta\cos(\theta)} \tag{3.13}$$

where d is the crystallite size, K is the shape factor, λ is the radiation wavelength, θ is the maximum diffraction peak angle, and β is the full width at half maxima (FWHM) of the peak.

The crystallite sizes of the Ru, RuO_2 and Al_2O_3 particles was determined using the line broadening of the most intense non-overlapping reflection for the respective compound.

3.4.4. Inductively-Coupled Plasma – Optical Emission Spectrometry (ICP-OES)

Inductively-Coupled Plasma–Optical Emission Spectroscopy (ICP-OES) was performed on the fresh catalyst to confirm the ruthenium loading. A Varian 730 ES ICP-OES Spectrometer was used to perform the analysis.

Due to difficulties which arose when attempting to perform a standard acid digestion, it was determined that it was necessary to use a fusion digestion method.

3.4.4.1. Fusion Catalyst Digestion

The fusion method was adapted from the method described by Suoranta *et. al.* [57]. 100 mg of sample was combined in a crucible with 0.38 g KOH and 0.65 g KNO_3, and heated to 450°C in a muffle furnace for 2 h. After cooling down overnight, 50 mg of $(NH_4)_2S_2O_8$ was added to stabilise the Ru compounds, and the sample was dissolved using a minimal amount of deionised water and transferred to a 50 ml volumetric flask. 10 ml of 1 M KOH solution was added, and the volumetric flask was filled to the mark with deionised water. 10 ml of this solution was then transferred to a 25 ml volumetric flask containing 5 ml of concentrated HCl, used to stabilise the Ru compounds as a chloro-complex ($RuCl_6^{2-}$), and the volumetric flask was filled to the mark. This sample solution was then submitted to the lab where a 1 ml of the solution was pipetted into a 10 ml volumetric flask and filled to the mark with 2 wt% aqueous HNO_3. The ultimate dilution was 100 mg of sample in 125 ml solution.

3.4.5. Chemisorption

CO chemisorption was used to determine the metal surface area of the fresh catalyst. The CO chemisorption was performed using a Micromeritics ASAP 2020 Surface Area and Porosity Analyser. The samples were degassed under vacuum at 120°C overnight. Approximately 0.15 g of catalyst was used for the analysis. The analysis was performed at 35°C.

3.4.6. Transmission Electron Microscopy (TEM)

Transmission-Electron-Microscopy (TEM) was used to obtain highly magnified images of the fresh and spent catalyst samples. The FEI T20 and the Technai Osiris TEM instruments at the Electron Microscope Unit of the University of Cape Town were used to collect bright field images of the samples. Quantifoil carbon film supported on copper TEM grids was used to study the samples. The powder samples were suspended in absolute ethanol and added dropwise onto the grids. The extent of suspension was examined visually, and highly concentrated suspensions were dropped onto the grid 3 – 4 times, while less concentrated suspensions were dropped onto the grid 5 – 6 times. The ethanol was allowed to completely dry off before the samples were ready for viewing. The images collected were then used to obtain a particle size distribution of the fresh catalyst, to determine the extent of sintering during reaction, and to determine the type of carbon deposition that was occurring on the catalyst. EDX was used to determine the chemical composition of certain features observed in the samples.

4. Results

4.1. Fresh Catalyst Characterisation

4.1.1. Thermogravimetric Measurements

Thermogravimetric analysis of the fresh catalyst was used to determine the reduction behaviour of the catalyst, and the extent of weight loss due to the removal of physisorbed water. The TGA-DTG-DTA curves are shown below for the oxidation of the fresh catalyst in air in Figure 4.1 and for the reduction of the fresh catalyst in hydrogen below in Figure 4.2.

4.1.1.1. Temperature-Programmed-Oxidation

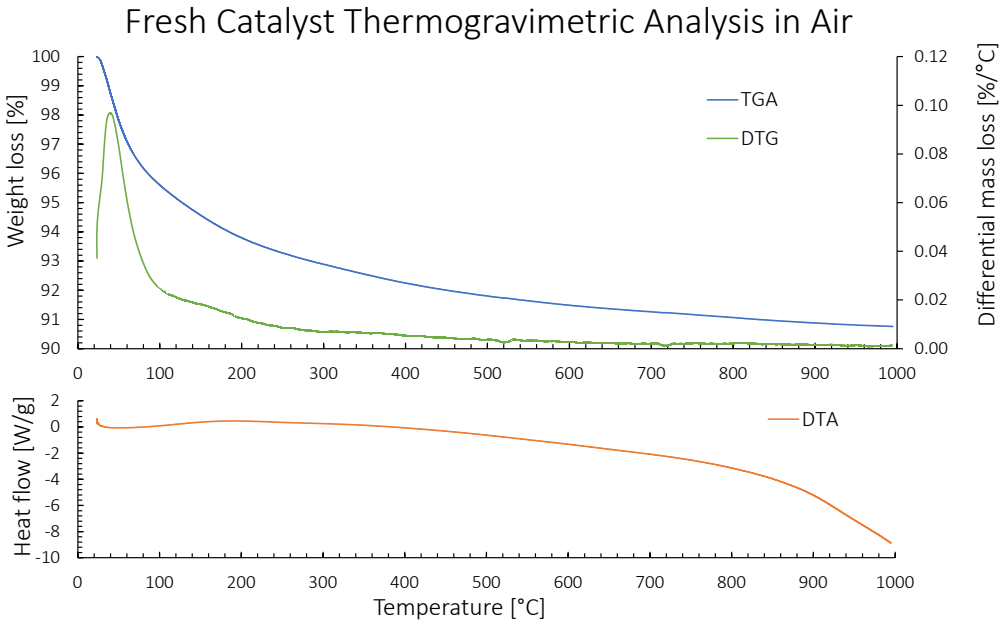

Figure 4.1: TGA-DTG-DTA curves of fresh 5% Ru/Al_2O_3 catalyst (FC-Cat) in Air (10 sccm) at 3°C/min heating rate

Overall mass loss is 9.8%. A peak in the DTG curve is observed at 40°C, which corresponds to the removal of physisorbed water from the catalyst. The DTA indicates an endothermic process at this temperature, consistent with the removal of physisorbed water [58].

4.1.1.2. Temperature-Programmed-Reduction

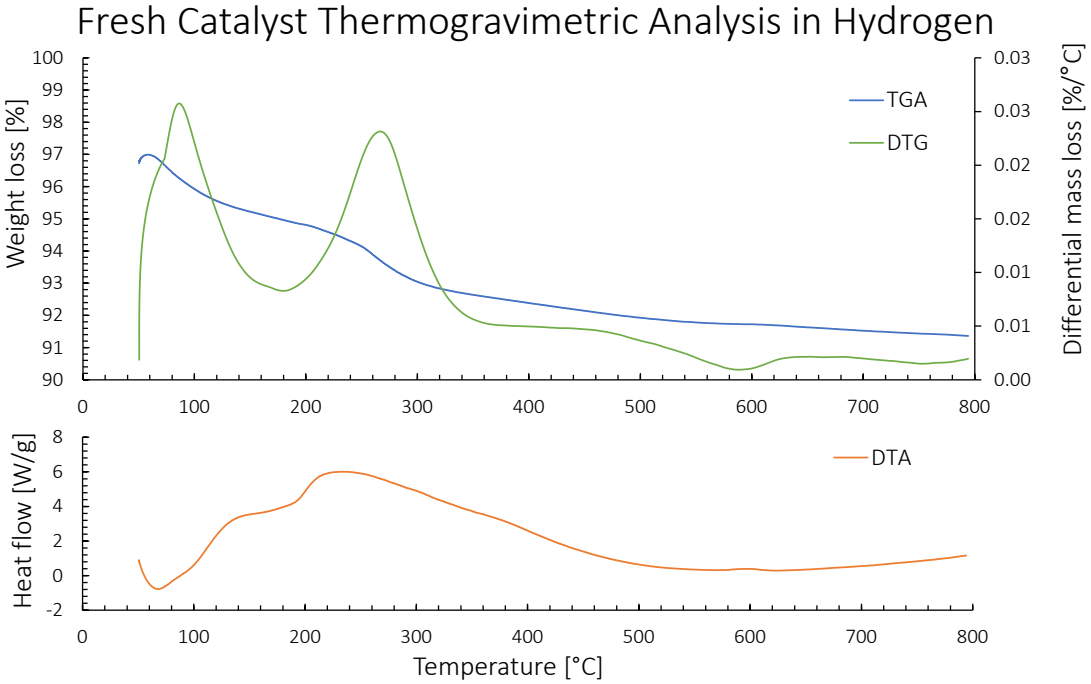

Figure 4.2: TGA-DTG-DTA curves of fresh 5% Ru/Al_2O_3 (FC-Cat) catalyst in H_2 (200 sccm) at 10°C/min heating rate

The TGA-DTG-DTA in hydrogen was performed up to a temperature of 800°C, and the curves are presented in Figure 4.2 above. The sample was equilibrated at 50°C for 20 min prior to the initiation of the TPR program, during which time there was 3% mass loss. Overall mass loss from the catalyst was 8.6%. Two peaks are observed in the DTG curve: the first at 89°C and the second at 270°C. There is a shoulder on the left side of the first peak. The DTA curve indicates that the shoulder on the first peak corresponds to an endothermic process, while the main peak and the entire second peak correspond to exothermic processes. While literature suggests slightly different temperatures – $RuCl_3$ at around 100°C and RuO_2 at around 200°C – the first peak likely corresponds to the reduction of $RuCl_3$ [58] while the second peak likely corresponds to the reduction of RuO_2 [59, 60]. While $RuCl_3$ is unexpected following the high temperature of calcination of the catalyst, it is possible that some remained due to the stagnant conditions of the muffle furnace used to perform the calcination.

4.1.2. BET and BJH Measurements

The FC-Cat was found to have a BET surface area of 168 m^2/g. This is only slightly below the surface area of the γ-alumina used to produce it, reported by the manufacturer at 185 – 215 m^2/g, indicating a decrease in surface area due to calcination. BET surface area of the CR-Cat was 138 m^2/g, a 30 m^2/g loss of surface area due to reduction at 750°C. The CRS-Cat surface area was 97.6 m^2/g, a further 40.4 m^2/g reduction in surface area after steaming at 750°C. The reduction in surface area is explained by sintering of the support, which reduces overall surface area and increases pore size. As the alumina support is exposed to high temperatures, it is anticipated that substantial decreases in support surface area will occur. Loss of surface area proceeds over time and is exacerbated by the presence of steam [61].

Table 4.1: Effect of reduction and steaming on catalyst BET surface area

Sample	*BET Surface area*
γ-Al_2O_3 support	185 – 215 m^2/g
FC-Cat	169 m^2/g
CR-Cat	138 m^2/g
CRS-Cat	97.6 m^2/g

Table 4.2 below indicates that during the reduction process, there was a decrease in pore volume, while there was an increase in pore size which is consistent with the processes described above. During the steaming process, there was a further reduction in pore volume, while there was a more substantial increase in pore size.

Table 4.2: Effect of reduction and steaming on catalyst pore volume and pore size

Sample	*Pore Volume*		*Pore Size (average diameter)*	
	Adsorption	Desorption	Adsorption	Desorption
FC-Cat	0.46 cm^3/g	0.45 cm^3/g	11.0 nm	10.6 nm
CR-Cat	0.40 cm^3/g	0.40 cm^3/g	11.6 nm	11.7 nm
CRS-Cat	0.39 cm^3/g	0.39 cm^3/g	16.1 nm	16.1 nm

4.1.3. Inductively Coupled Plasma – Optical Emission Spectroscopy (ICP-OES)

ICP-OES was performed on the FC-Cat. Following the fusion digestion of the catalyst, ICP-OES indicated a final dilution concentration of 4.0 ppm (of the digested catalyst solution, diluted for use by the analytical lab), indicating a concentration in the initial diluted sample of 40 ppm, confirming that the metal loading on the catalyst is 5 wt%.

$$\frac{40\,\frac{\text{mg}}{\text{l}} \times 0.125\,\text{l}}{100\,\text{mg Catalyst sample}} = \frac{5\,\text{mg Ru}}{100\,\text{mg Catalyst}} = 5\,\text{wt\% Ru} \tag{4.1}$$

4.1.4. CO Chemisorption

The FC-Cat sample was reduced in the Micromeritics ASAP 2020 in 2 stages, up to 100°C at 2.0°C/min, and further up to 350°C at 5.0°C/min. Results from the TPR of the sample (see Section 4.1.1.2) indicate that this reduction procedure should fully reduce the metal particles, accurately representing the state of the catalyst in-situ after reduction. CO chemisorption indicated a low Ru dispersion of 2.9%. This dispersion value is lower than values reported in literature [62], which may be attributed to the use of wetness impregnation as opposed to incipient wetness impregnation. The analysis assumed a weight loading of 5% Ru on the support, which was validated by the previously collected ICP-OES data. Results from the CO chemisorption analysis are presented in Table 4.3 below.

Table 4.3: Metal dispersion and metallic surface area of FC-Cat from CO chemisorption

Property	*Fresh catalyst sample*
Metal dispersion	2.93%
Metallic surface area	0.53 m^2/(g of sample)
Metallic surface area	10.7 m^2/(g of metal)
Crystallite size	37.8 nm

4.1.5. X-ray Diffraction (XRD)

Powder XRD measurements of the fresh catalyst samples were collected to determine the effects of the pre-treatment, in-situ reduction procedure and the steaming procedures. The diffractograms were also analysed to determine the crystallite size of the Ru/RuO_2 particles. The diffraction patterns for the samples can be seen in Figure 4.3 below. The results from the analyses of the crystallite sizes are presented in Table 4.4 below.

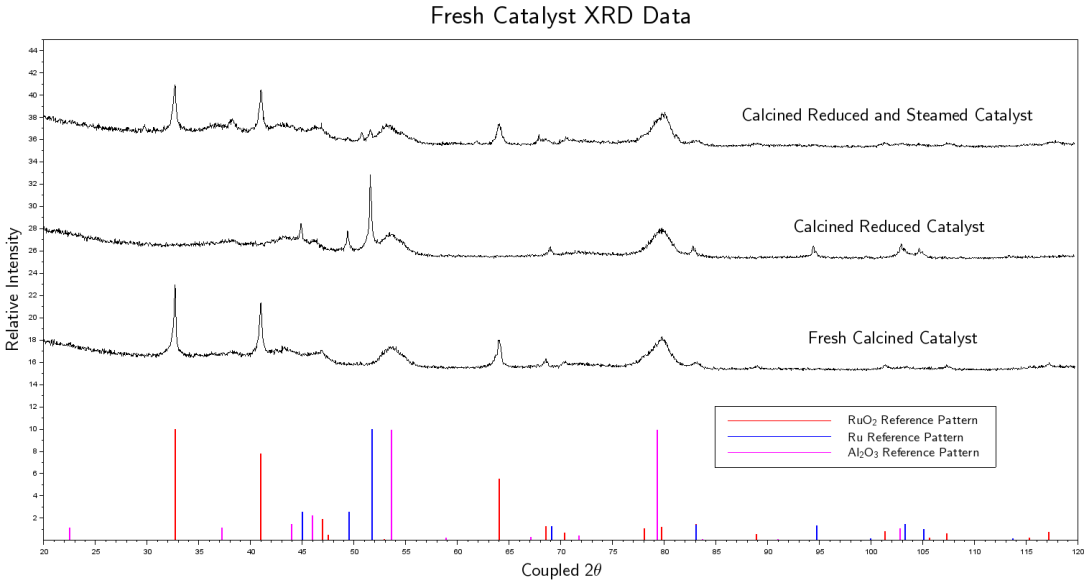

Figure 4.3: XRD pattern data for fresh calcined catalyst (FC-Cat), reduced catalyst (CR-Cat) and reduced and steamed catalyst (CRS-Cat) with reference patterns for Ru, RuO_2 and Al_2O_3

The diffractogram in Figure 4.3 indicates that the ruthenium in the fresh catalyst is in the oxide form, with crystallite size determined by the Scherrer equation to be 46.9 nm. In the reduced catalyst, the ruthenium is confirmed to be reduced, and yields Ru particles with crystallite size 49.7 nm. Following the reduction and steaming procedure, the ruthenium returns to its oxide form, with a reduced crystallite size of 29.3 nm. The alumina support crystallite size is greater in the samples which were held at a higher temperature for a longer time period.

The crystallite sizes of the Ru, RuO_2 and Al_2O_3 particles, as reported in Table 4.4, were determined using the line broadening of the most intense non-overlapping reflection for the respective compound.

Table 4.4: Crystallite size and components of the fresh catalyst samples

Sample	*Crystallite Size (nm)*		
	RuO_2	Ru	Al_2O_3
FC-Cat	46.9		5.06
CR-Cat		49.7	6.49
CRS-Cat	29.3		6.95

4.1.6. Transmission Electron Microscopy (TEM)

Transmission electron microscopy was used to determine the morphology of the particles, as well as particle size distribution of the Ru and RuO_2 particles on the fresh catalyst samples. Where possible, high magnification images were obtained so that the d-spacing of particles of interest could be measured.

Table 4.5: TEM determined particle size for fresh catalyst samples and particles counted

Sample	*Average particle diameter**	*Median particle diameter*	*Particles counted*
FC-Cat	733 ± 579 nm	529 nm	406
CR-Cat	693 ± 486 nm	560 nm	233
CRS-Cat	311 ± 313 nm	223 nm	468

*Average value ± 1 standard deviation, indicating wideness of distribution

The diameter of the particles was measured as the longest line that could be drawn over the particle, which may result in an exaggerated particle size distribution. In particular, for the reduced and steamed catalyst sample, the particles took on a platelet shape, wherein an equivalent particle diameter would correspond to a much smaller particle volume.

4.1.6.1. Fresh Calcined Catalyst (FC-Cat)

TEM images of the FC-Cat are displayed below in Figure 4.4. The left image is representative of the morphology of a majority of the metal oxide particles – jagged and rounded, attached to small support fragments. The particles were clearly identifiable, enabling a confident determination of the particle size distribution. The centre image displays the alumina support with dispersed nanoparticles. Where difficultly arose in determining if particles were part of the metal oxide or part of the support, the particle in question was excluded from analysis. The right image displays the d-spacing observed for one of the metal oxide particles, confirming the identification of the particles as the metal oxide.

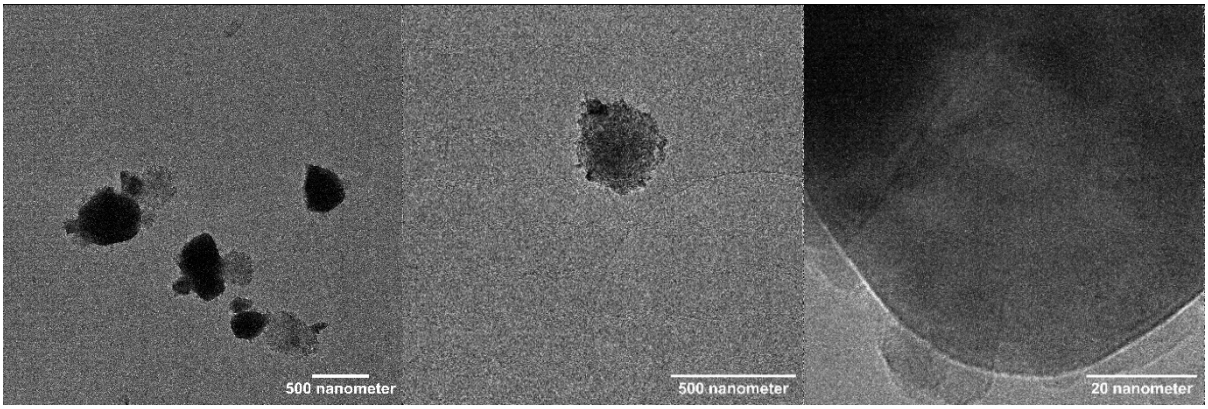

Figure 4.4: TEM images of fresh calcined catalyst (FC-Cat)

The particle size distribution (PSD) for the FC-Cat is displayed below in Figure 4.5. The analysis indicated a broad particle size distribution, with a long tail towards larger particles. The mode of the PSD is in the 200 – 300 nm range. The average particle size was 733 ± 579 nm, indicating the broadness of the distribution.

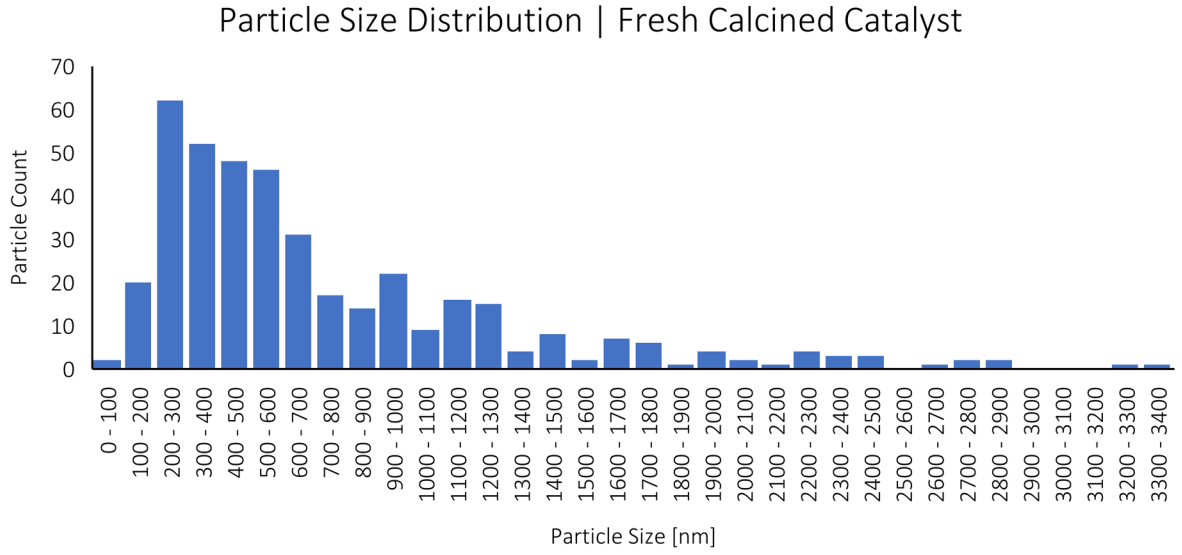

Figure 4.5: Metal oxide particle size distribution for the fresh calcined catalyst (FC-Cat) sample, 406 particles counted

4.1.6.2. Calcined Reduced Catalyst (CR-Cat)

TEM images of the CR-Cat sample are displayed below in Figure 4.6. The left image is of dispersed particles on the support. The middle image shows a larger metal particle situated on the support. The right image displays two large metal particles, not attached to the support. Many of the particles analysed took on a more crystalline shape, reflecting the crystal structure of the ruthenium metal, and indicating the restructuring occurring during the reduction. The metal particles were clearly identifiable, enabling a confident determination of the particle size distribution.

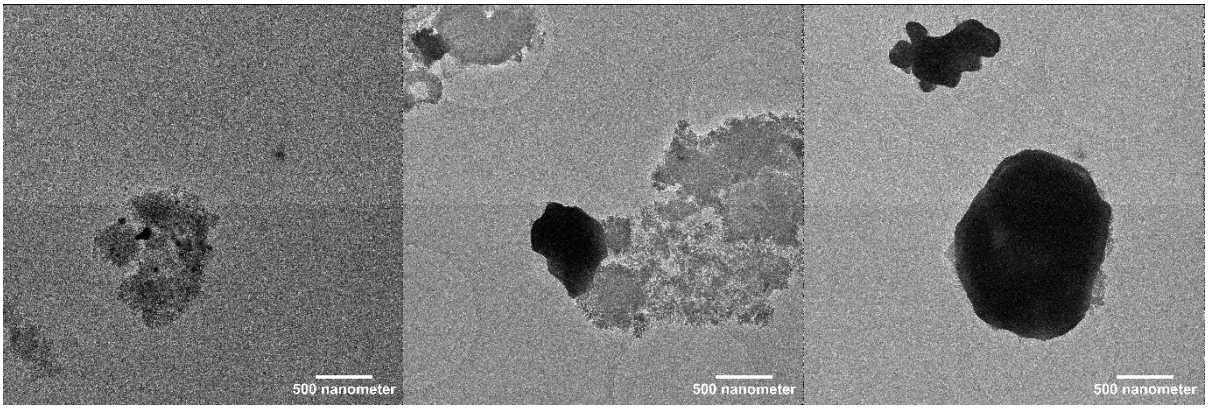

Figure 4.6: TEM images of the reduced catalyst sample (CR-Cat)

The PSD for the CR-Cat sample is displayed below in Figure 4.7. The tail of the distribution has shortened in comparison to the fresh calcined catalyst. The mode of the PSD is in the 300 – 400 nm range, an increase in comparison to the fresh calcined catalyst. The average particle diameter was determined to be 693 ± 486 nm, indicating a reduction in broadness of the distribution in comparison to the FC-Cat sample.

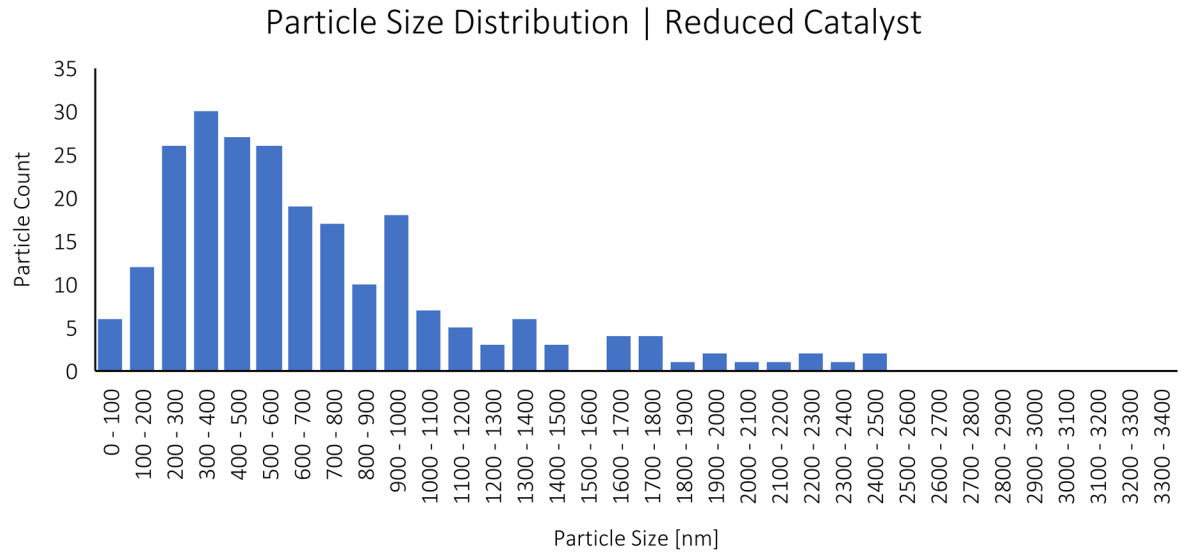

Figure 4.7: Metal particle size distribution for the reduced catalyst sample (CR-Cat), 233 particles counted

4.1.6.3. Calcined, Reduced and Steamed Catalyst (CRS-Cat)

TEM images from the CRS-Cat sample are provided below in Figure 4.8. The left image shows an agglomeration of metal oxide platelets. The middle image shows the d-spacing of a one of the platelets. The right image displays a larger agglomeration of platelets. In contrast to the other samples, a clear morphology change is observed. The platelets were identified due to their low contrast, indicating their thin and flat shape. Where significant overlap between platelets made differentiation between particles difficult, the particles were excluded from analysis.

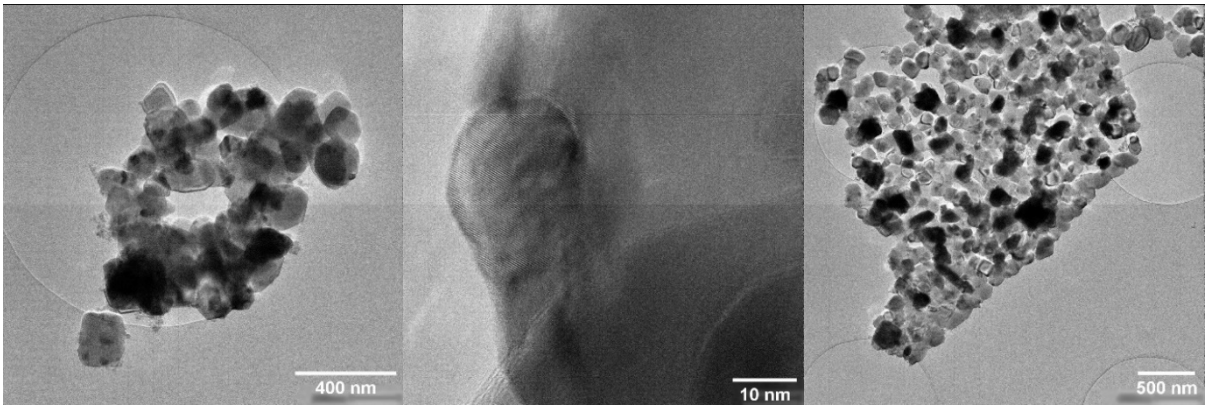

Figure 4.8: TEM images of reduced and steamed catalyst sample (CRS-Cat)

The PSD for the CRS-Cat is provided below in Figure 4.9. The tail of the distribution is radically shortened in comparison to FC-Cat and the RC-Cat. The mode of the PSD is in the 100 – 200 nm range, a decrease in comparison to the reduced catalyst. Since the particles were platelet in shape, and were typically observed in a flat orientation, the apparent diameter of the particles may be smaller still than the measured diameter. Nonetheless, the average particle diameter was determined to be 311 ± 313 nm, indicating a reduction of the distribution in comparison to the reduced catalyst sample, and a substantial reduction in particle size.

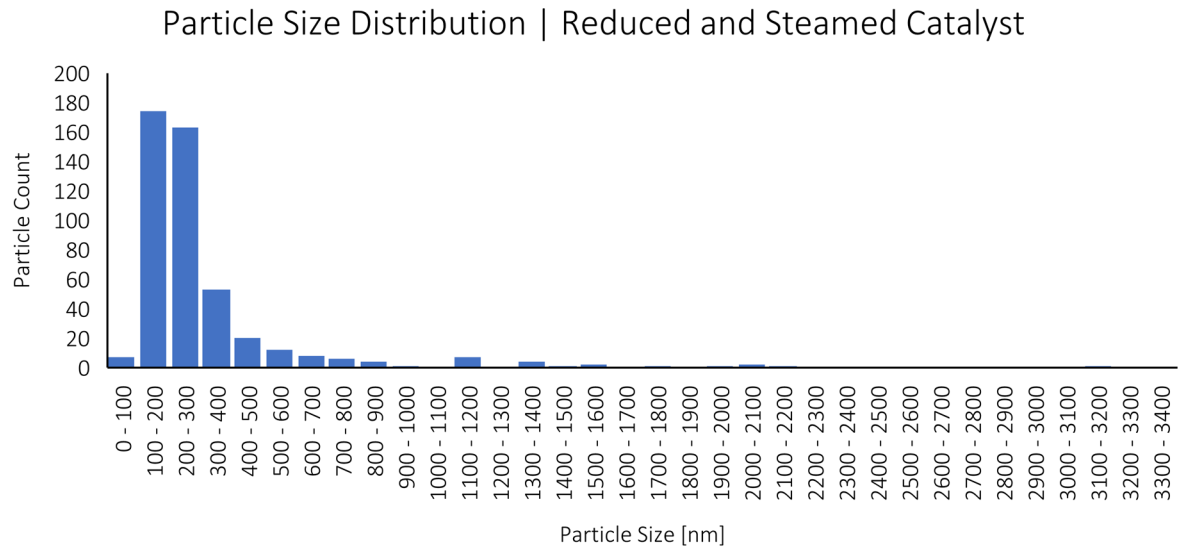

Figure 4.9: Metal oxide particle size distribution for the reduced and steamed catalyst sample (CRS-Cat), 468 particles counted

4.2. Propane Steam Reforming Experiments

A single batch of 5 wt% Ru/Al_2O_3 catalyst was used for all experiments, prepared as described in Section 3.1 and with properties as described in Section 4.1. Unless otherwise stated, testing procedures and conditions are as per those described in Section 3.2.5.

Changes to the standard testing procedures include start-up procedure, air co-feeding (1% and 3% of dry feed composition) and steam-to-carbon ratio (S/C = 3, 3.5, 4, 6), the latter two variables being implemented intermittently during experiments. Experiments were named based on the start-up procedure, using **C**alcined **R**educed (CR) and **C**alcined **R**educed and **S**teamed **C**atalyst **R**un (CRS) as identifiers. A summary of the experiments and the changed variables is presented below in Table 4.6.

Table 4.6: Summary of catalytic performance testing experiments and variables changed

Name	*Time-on-stream [h]*	*Steamed*	*S/C changed*	*Changed air?*
Blank	234	No	No	No
CR-1	498	No	No	No
CR-2	289	No	No	Yes
CR-3	359	No	No	Yes (1% added)
CR-4	715	No	Yes (6)	Yes (3% added then removed)
CRS-1	589	Yes	Yes (3.5, 3)	Yes (1% removed)
CRS-2	165	Yes	No	Yes (1% removed)

4.2.1. Preliminary findings

4.2.1.1. Blank Experiment and Thermal Background Activity

An experiment was performed without catalyst to determine effect of the presence of reactor wall and SiC packing inertness as well as homogeneous reactions given the relatively high temperature of 750°C employed for all catalytic tests. Standard experimental conditions and a reduced catalyst start-up procedure were applied but for the reactor packing containing no catalyst. Conditions remained unchanged throughout the test.

Experimental findings for the blank experiment are provided in Figures 4.10 to 4.15; however, it should be noted from Figure 4.15 that for this experiment the measured water feed rate was slightly lower than that required for the intended standard S/C ratio of 4 and that it declined further from a starting S/C ratio of 3.5 to an S/C ratio of 3, roughly half way through the experiment at around 125 h-on stream. Also noteworthy is the carbon balance in Figure 4.12, which remains constant throughout the experiment, despite the variation in water feed rate, at a particularly high degree of closure, generally between 100 – 103%, but for the initial period up to 20 h time-on-stream. That the initial time-on-stream exhibits transitory behaviour is not surprising as feed and product flow rates and composition (notably feed water rates and product catch pot flushing) may be expected to stabilise during an initial period after experiment

initiation and, indeed, it is a feature of all reaction experiments, with or without catalyst albeit that this period of unsteady-state behaviour differs between experiments.

The C_3 conversion and total hydrocarbon conversion are presented below in Figures 4.10 and 4.11, respectively. But for the initial 20-h period, both are stable throughout the experiment with total hydrocarbon conversion essentially negligible but C_3 conversion at approximately 15%, neither seemingly affected by the change in S/C ratio mid-way through the experiment. Figure 4.13 presents carbon product selectivities which, but for the initial settling-in period, remain stable throughout the remainder of the experiment and which exhibits very little CO_x formation such that the conversion of propane is seen to be roughly half to propene and the remainder to C_2 and C_1 fragments, i.e., due to propane thermal 'cracking'.

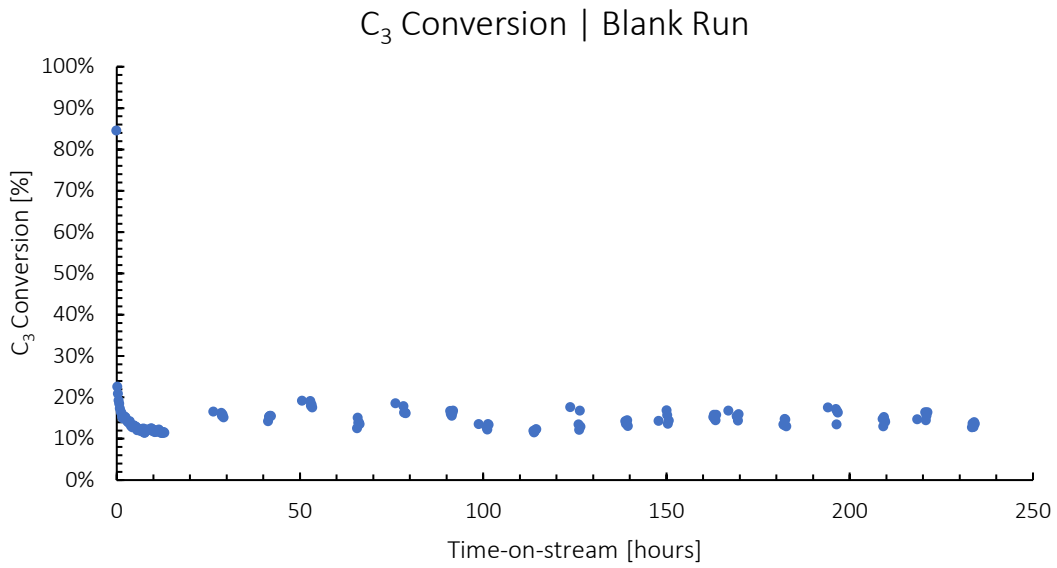

Figure 4.10: C_3 conversion vs. time-on-stream for the blank run at 750°C and 1 bar_g

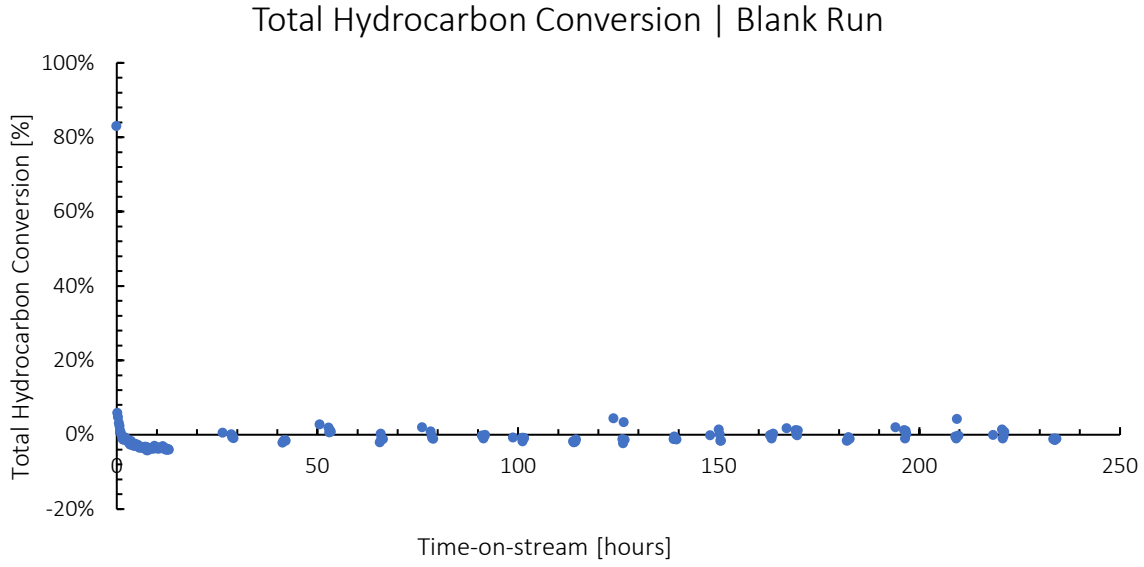

Figure 4.11: Total hydrocarbon conversion for the blank run at 750°C and 1 bar_g

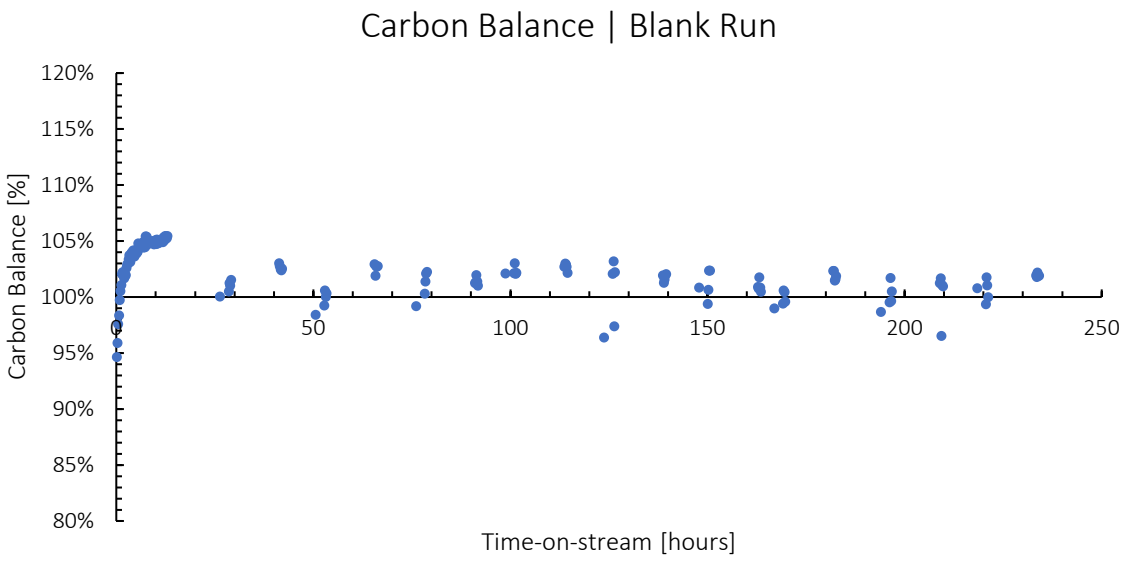

Figure 4.12: Carbon balance vs. time-on-stream for the blank run at 750°C and 1 bar_g

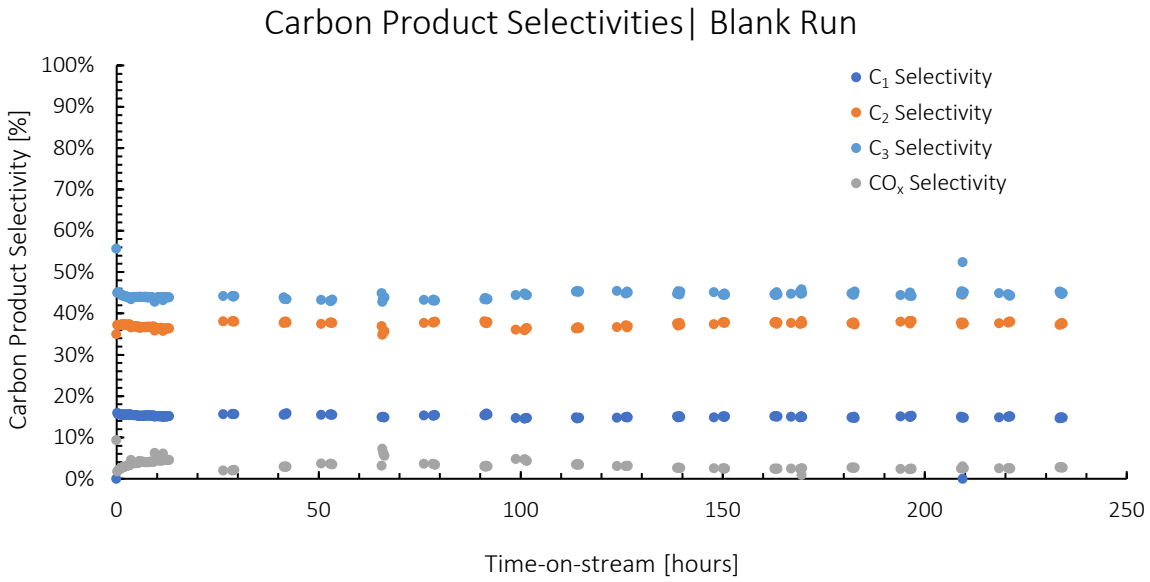

Figure 4.13: Carbon product selectivities for the blank run at 750°C and 1 bar_g

The CO_x data are presented below in Figure 4.14. After the initial 20 h period, the CO:CO_2 ratio continues to decline steadily over 100 h time-on-stream to a steady value of approximately 2 for the remainder of the experiment, albeit that given the very low CO_x selectivity (see Figure 4.13) the ratio between these two minor products is potentially subject to appreciable experimental inaccuracy.

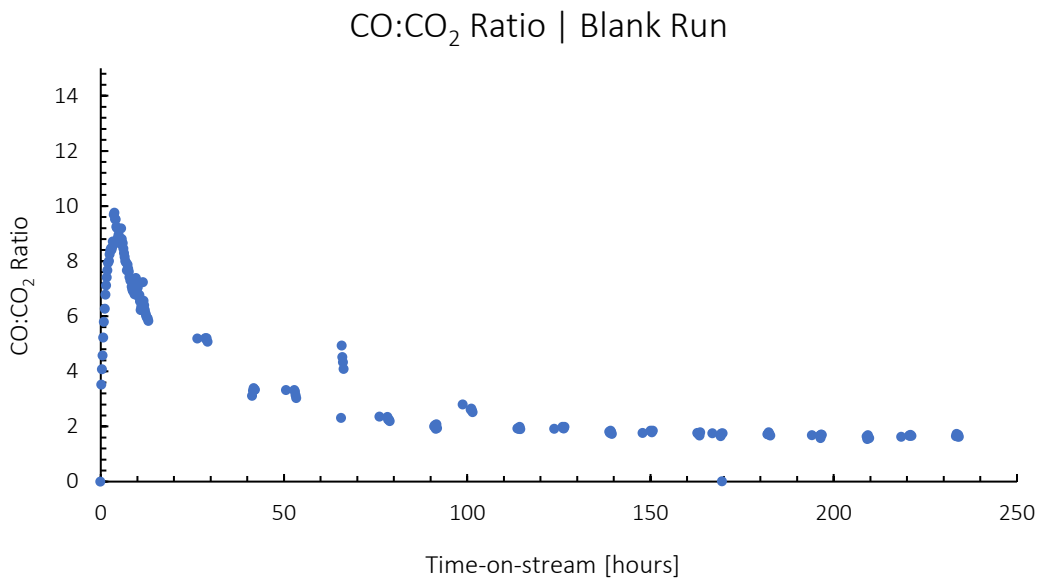

Figure 4.14: $CO:CO_2$ Ratio for the blank run at 750°C and 1 bar_g

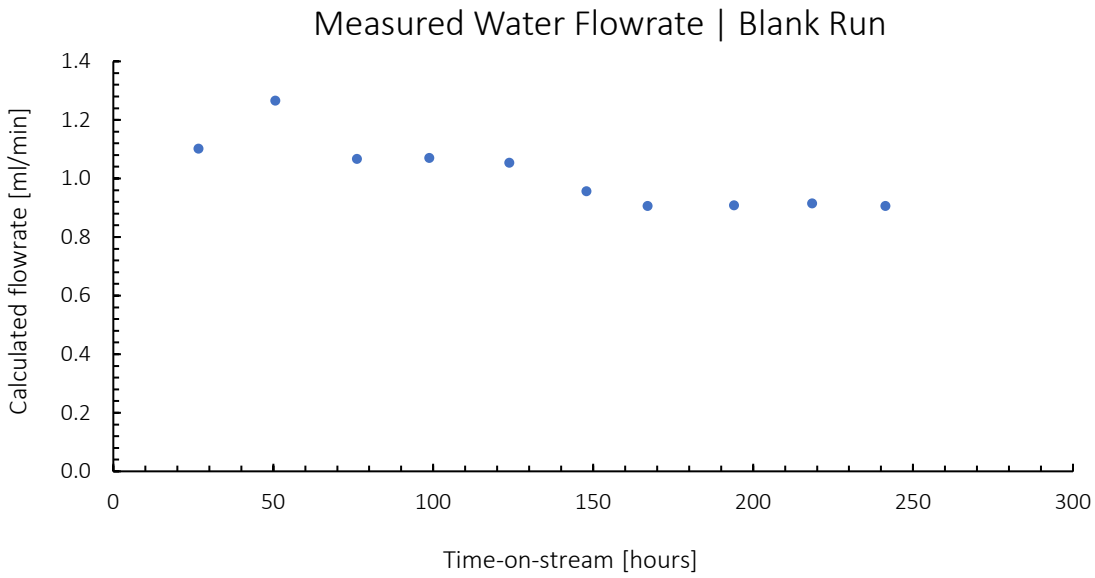

Figure 4.15: Measured water flowrate vs. time-on-stream for the blank run

In summary, but for an initial settling-in period of about 20 h, the results from the blank experiment indicate stable thermal activity of the reaction system, which results in about 30% propane feed conversion, of which roughly half is converted to propene (yielding a 15% C_3 conversion) and the remainder to C_2/C_1 fragments consistent with limited thermal 'cracking' and with essentially negligible CO_x formation, i.e., essentially no hydrocarbon steam reforming.

4.2.1.2. Experimental Difficulties

Several experimental difficulties were encountered during the extended period of this study. These are presented below for the record but where appropriate are noted in the presented data and/or the data ignored for purposes of interpretation of experimental findings.

4.2.1.2.1. Furnace Temperature

The maintenance of stable furnace temperature for long time-on-stream experiments and over the extended period during which experiments were conducted proved challenging and, at times, impacted on experimental integrity. The principal cause for this was failure of the electric heating cartridges used in the furnace heating block surrounding the reactor tube – the cartridges themselves not suited for extended use at the temperature of the experiments (750°C). The consequence was the loss or early termination of experiments due to a loss in furnace heating capable of sustaining the reaction temperature. The issue was further aggravated by the absence of an internal thermowell/thermocouple to read temperatures directly within the catalyst bed – experimental temperatures were thus observed and recorded from the thermocouples embedded in the furnace heating block which, given the furnace reactor design and construction, are reliable measures of the heated reactor zone. Heating cartridge failure was thus observed from measured block temperatures falling below the set-point of 750°C and which, when observed, resulted in termination of experiments and furnace heating cartridge replacement. Nonetheless, some of the experimental data presented may have been affected by such events and where this is possible the case of such deviations from the standard operating temperature is noted in the presented data.

In particular, the furnace temperature of the first three experiments (CR-1, CR-2, and CR-3) was lower than intended because of failure of the heating cartridges used to heat the furnace. The remaining experiments, CRS-1, CRS-2, and CR-4 were less affected by furnace breakdown throughout the experimental run.

4.2.1.2.2. Water Feed

As was seen in the blank experiment (see Section 4.2.1.1), the HPLC pump for water feed to the reactor on occasion did not deliver consistent water feed to the system over the entire duration of the experiments. Indeed, on occasion the feed pump would fail, and water delivery would be halted entirely for limited periods, sometimes leading to abandonment of the experiment. The reason for such failures is simply that given the scale of the catalyst charges employed, the pump operates close to the bottom of its design range such that water feed air bubbles or minor impurities (dirt) easily result in variations in feed rate over the extended experimental periods. Where such deviations from the intended feed rates were observed (from water feed reservoir mass recording), these are noted for the data presented.

4.2.1.2.3. Air Ingress Upon Water Catch Pot Drainage

When the water catch-pot was drained shortly before the initiation of the sampling sequence, it appeared from the chromatograms that some amount of air may have entered the catch-pot,

diluting and contaminating the effluent stream prior to chromatographic analysis. The problem was most pronounced towards the end of the experiments, due to reduced effluent stream flows for reason of lower propane reforming activity. Where significant ingress was observed, data have been ignored for purposes of any interpretation of findings.

4.2.1.2.4. Argon Chromatographic Integrity

On rare occasion, the observation of reduced argon chromatographic peak areas led to the exclusion of such data for purposes of an interpretation of experimental finding, even though it may still be included in the presented data sets – this for reason of argon as the chromatographic internal standard affecting all other component flow determinations.

4.2.1.3. Carbon balance criterion

The carbon balance for the experiments was considered 'good' if it was within 10% of perfect closure (100% mass balance). All experiments presented a similar pattern for the carbon balance – during the initial 'settling-in' period of the catalyst, the carbon balance started relatively low, trending towards 100% for a period of time, thereafter, to deviate again. For some experiments, where the carbon balance deteriorated beyond 10% (i.e., outside the range 90 – 110% balance) it is noted in the data presentation and/or interpretation.

4.2.1.4. *Experimental reproducibility*

There was a degree of variation between experiments with theoretically identical operating conditions. In particular, the general pattern observed for the CR experiments is similar, but the rate of activity decay is different, and the steady state performance also differs. This can be observed in Figure 4.16. Experimental reproducibility was particularly improved for CRS runs, as can be observed in Figure 4.17.

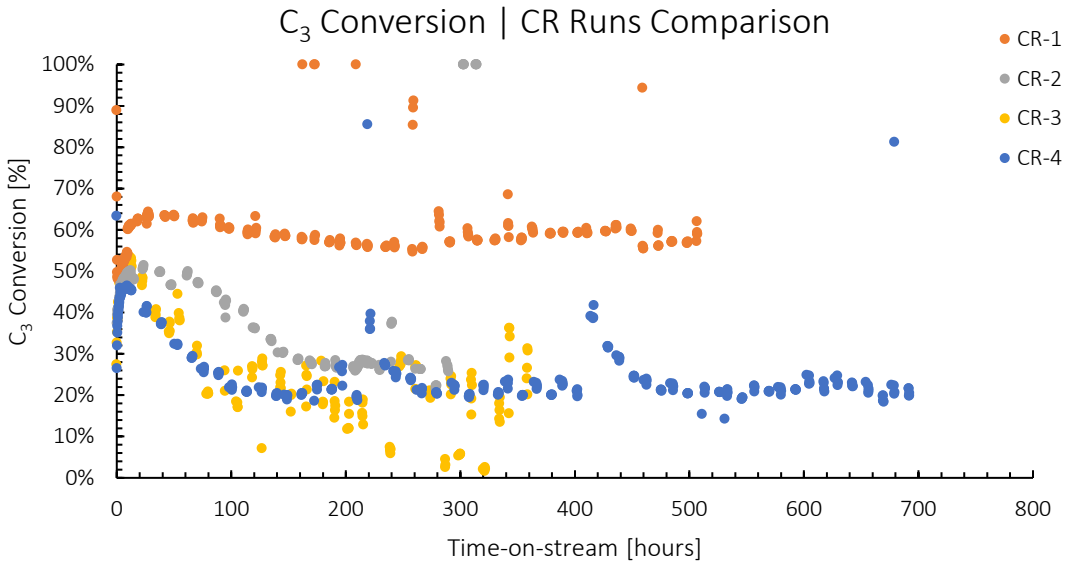

Figure 4.16: C_3 conversion vs time-on-stream comparison between CR experimental runs

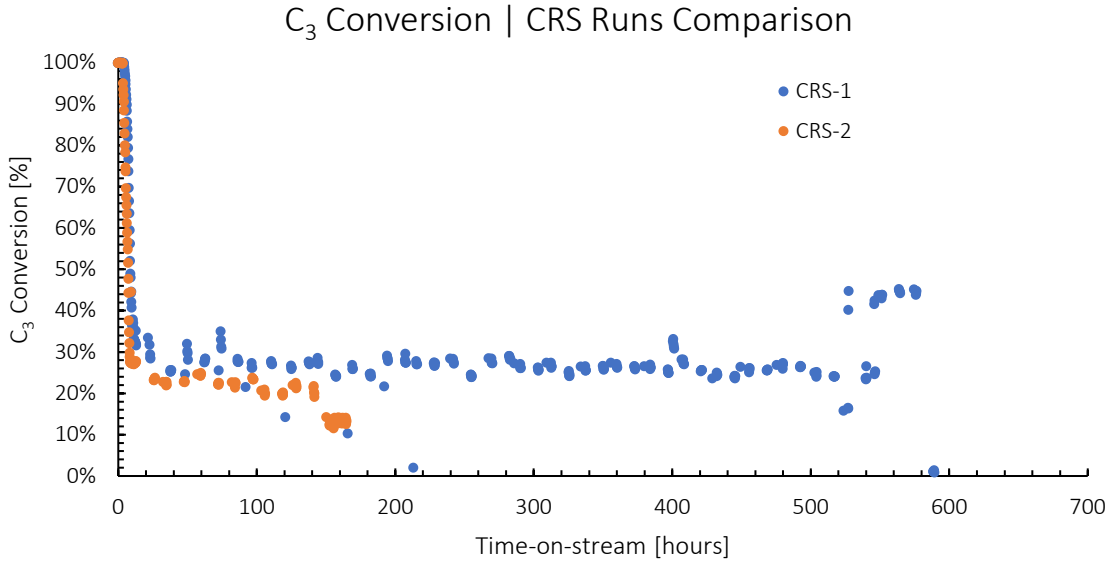

Figure 4.17: C_3 Conversion vs time-on-stream comparison between CRS experimental runs

4.2.2. Experiments using Calcined Reduced Catalyst

4.2.2.1. Experiment CR-1

Experiment CR-1 was performed to establish baseline catalytic performance and stability of the catalyst. The experiment was started following the reduction procedure outlined in Section 3.2.5.1.1. No variables were changed during the experiment, bar those changed incidentally due to malfunction of the water pump. The experiment proceeded until no further changes in reaction products were observed and was terminated at 498 h time-on-stream. The shutdown procedure outlined in Section 3.2.5.3 was followed and the catalyst was recovered as per Section 3.2.5.4.

Experimental findings for CR-1 are provided in Figures 4.18 to 4.25. It should be noted from Figure 4.25 that the S/C ratio was lower than intended, declining gradually from 3.7 to 3 relatively linearly over the course of the experiment, until its correction at 460 h time-on-stream. Also noteworthy is that the carbon balance begins to exceed 10% deviation after 270 h time-on-stream, and the data thereafter may be regarded as less reliable.

C_3 conversion and total hydrocarbon conversion are shown in Figures 4.18 and 4.19, respectively. C_3 conversion increases from 46% to a peak of 64% over the initial 30 h time-on-stream, whereafter it remains stable at 55 – 60% for the remainder of the experiment (~500 h). Likewise, total hydrocarbon conversion increases from 36% to 47% over the initial 30 h time-on-stream, whereafter it declines steadily to approximately 20% at around 270 h and remains stable for the remainder of the experiment. Initially (at the 30-h time-on-stream peak activity), C_3 conversion is approximately 15% higher than total hydrocarbon conversion, consistent with the roughly 15% C_3 conversion observed in the blank experiment (Figure 4.10). However, while C_3 conversion remains relatively high and constant throughout the experiment, the total hydrocarbon conversion falls with time-on-stream to a stable value of roughly 20% (at 270 h) and remains as such for the remainder of the experiment. Hence, whereas C_3 conversion appears stable throughout the experiment, total hydrocarbon conversion (reforming) stabilises only after 270 h, at which point cracking accounts for roughly 60% of all propane conversion, with the balance of 40% being attributed to hydrocarbon reforming. This observation also suggests that, at steady state (i.e., beyond 270 h time-on-stream), the catalyst itself contributes to cracking and that this activity is not solely due to thermal (blank) effects.

It should be that whereas the carbon balance (see Figure 4.20) is essentially 100% after 30 h time-on-stream – when both C_3 and total hydrocarbon conversion peak – it thereafter steadily declines to about 90% at 270 h for the remainder of the experiment, similar to the situation with total hydrocarbon conversion.

Carbon product selectivities are shown in Figure 4.21, indicating increasing reforming selectivity over hydrocarbon cracking in the initial reaction period (notionally 20 – 30 h time-on-stream) after which CO_x selectivity declines rapidly until all selectivities stabilize around 270 h time-on-stream – consistent with C_3 and total hydrocarbon conversion.

The $CO:CO_2$ ratio for CR-1 is presented in Figure 4.22, falling initially to a value of roughly 10 after 30 h time-on stream, then declining constantly to a value of approximately 1.3 when conversion and selectivity stabilize at around 270 h.

The above presented performance data – C_3 conversion (Figure 4.18), total hydrocarbon conversion (Figure 4.19) and selectivity (Figures 4.21 and 4.22) – describe a general pattern of an initial 20 – 30 h period of rapid catalytic change followed by a period of 'linear' change to approximately 270 h time-on-stream, after which essentially stable performance ensues. The initial period may be considered a 'settling-in' period over which some sort of catalyst restructuring and activation occurs – possibly the formation of carbon compounds given the initial low (70%) carbon balance recorded (Figure 4.20). The subsequent 'linearly' declining performance period is perhaps more akin to steady catalyst deactivation of the conventional kind (fouling, sintering, etc.) with the final stable performance phase reflecting some form of steady-state where the catalyst has 'equilibrated' under the prevailing reaction environment.

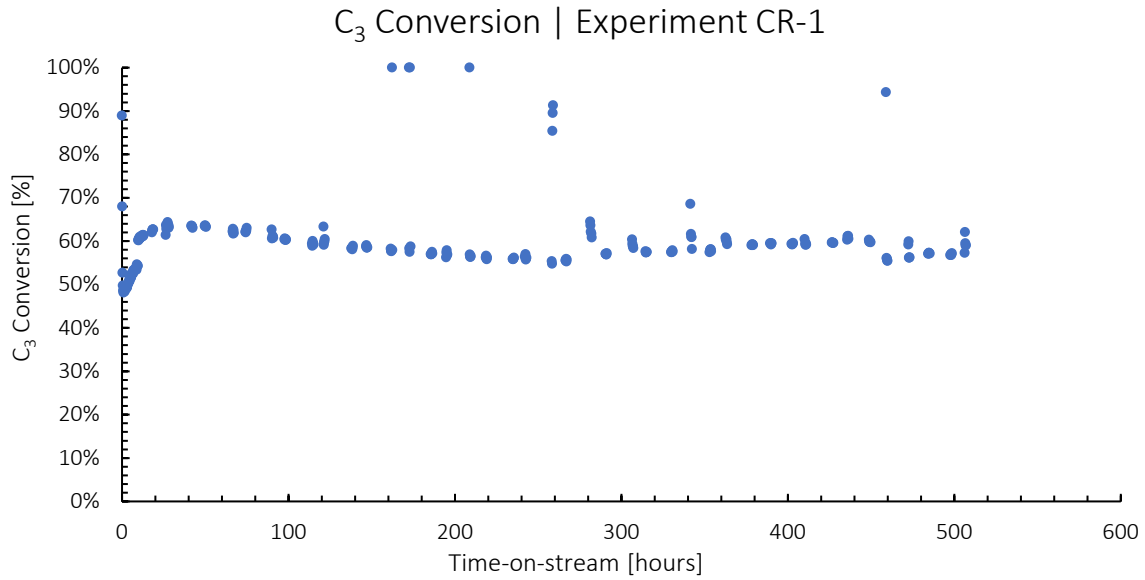

Figure 4.18: C_3 conversion vs. time-on-stream for experiment CR-1 at 750°C and 1 bar_g

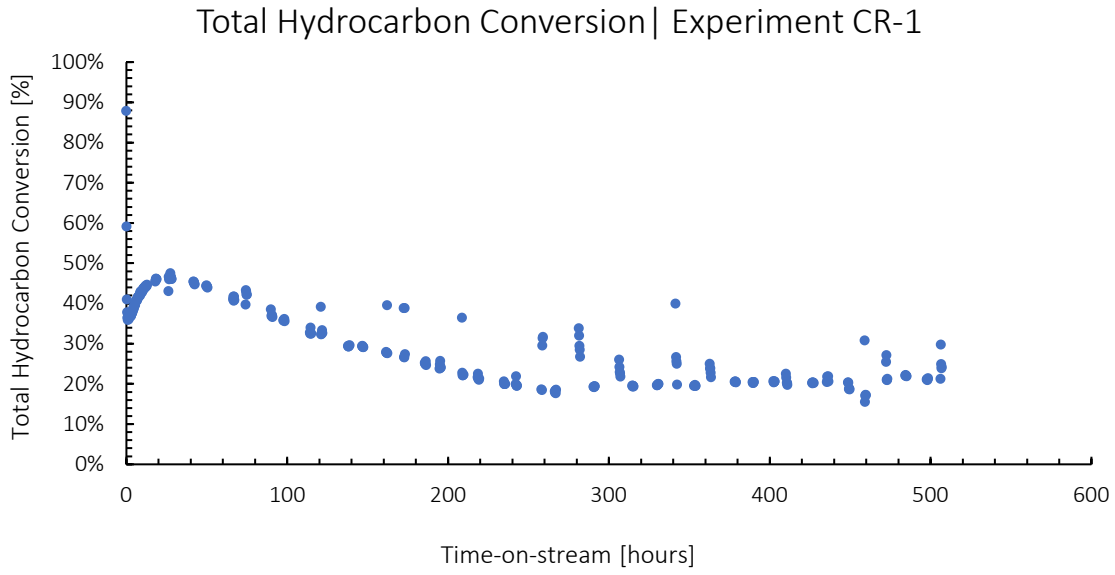

Figure 4.19: Total hydrocarbon conversion vs. time-on-stream for experiment CR-1 at 750°C and 1 bar_g

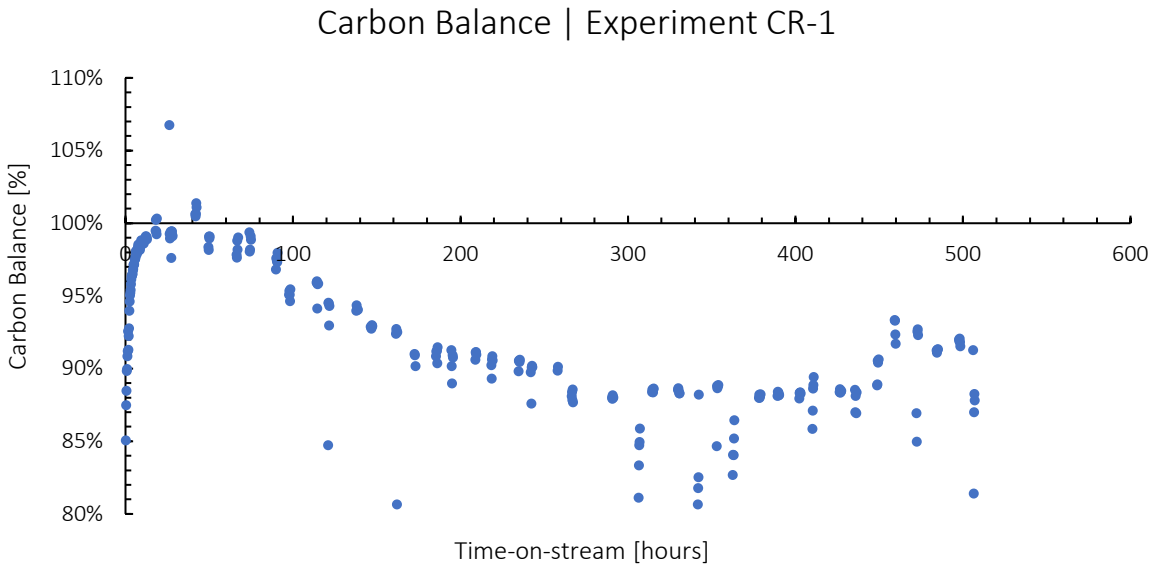

Figure 4.20: Carbon balance vs. time-on-stream for experiment CR-1

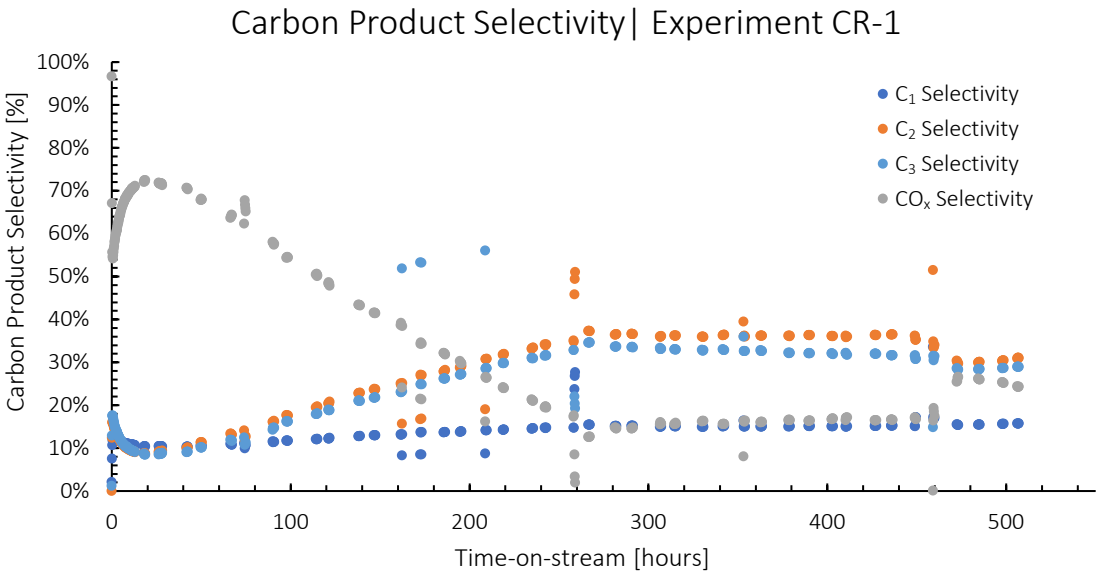

Figure 4.21: Carbon product selectivities vs. time-on-stream for experiment CR-1 at 750°C and 1 bar_g

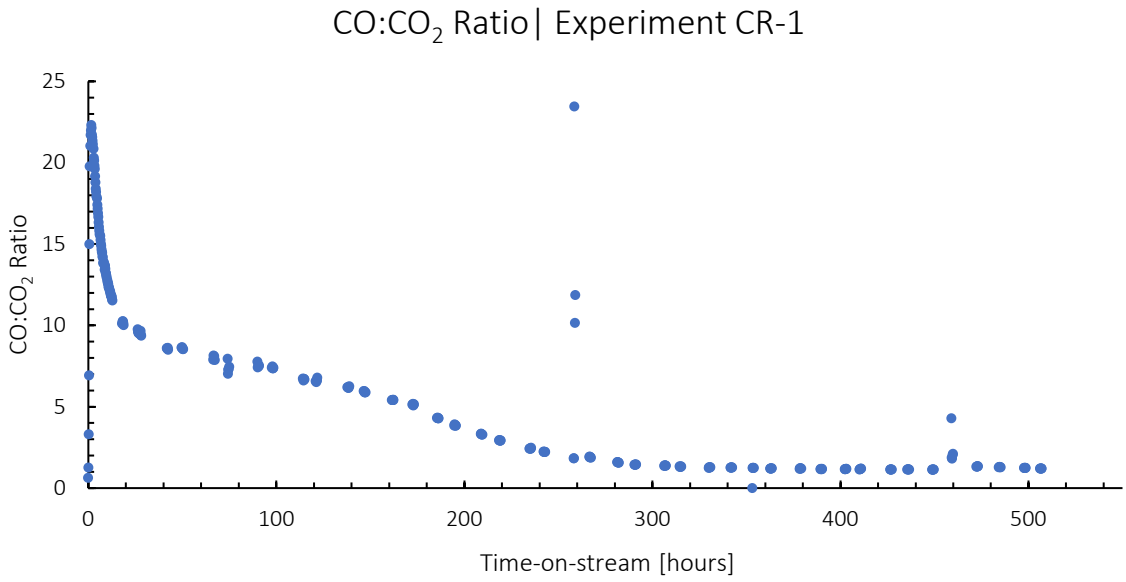

Figure 4.22: $CO:CO_2$ ratio vs. time-on-stream for experiment CR-1 at 750°C and 1 bar_g

Figure 4.23 presents nitrogen flowrate in the product stream over the course of the experiment. Since the feed to the reactor did not contain nitrogen, this supports the hypothesis that air ingress is occurring upon water catch pot drainage, *viz.*, the rapid release of substantial quantities of water leads to air suction into the catch pot. The pattern observed is also consistent with ingress, since the flowrate consistently decreases after a brief spike. Furthermore, as the effluent stream reduces due to decreased conversion, the dilutant nitrogen would be purged from the water-catch pot more slowly, and this is also reflected in the larger spikes in nitrogen towards the end of the run. Even so, these nitrogen flows are relatively small versus the total

reactor effluent flowrate and given the use of argon as chromatographic internal standard should not adversely affect product analyses.

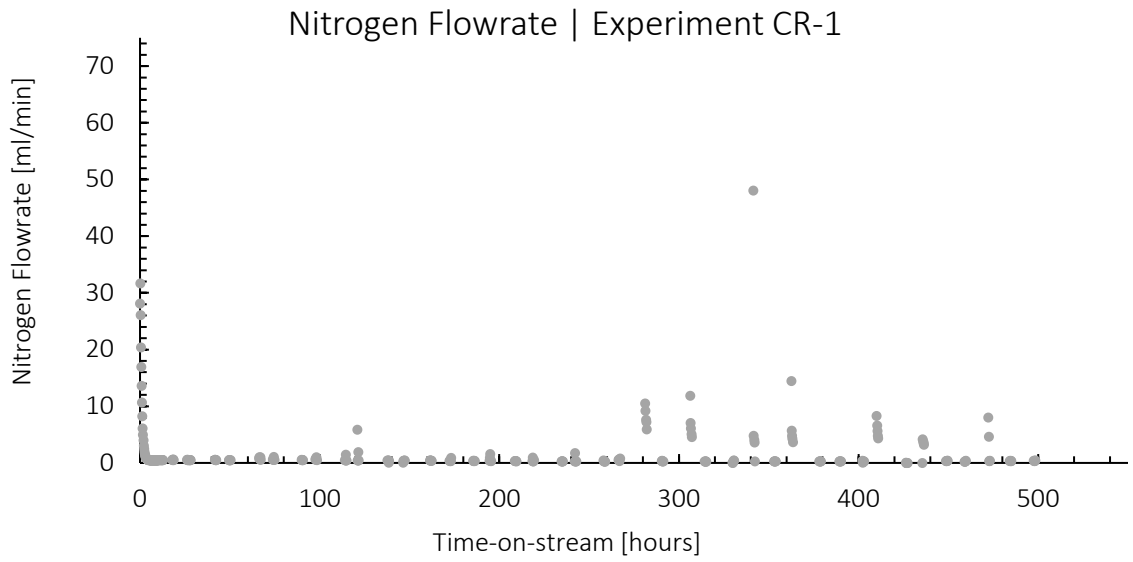

Figure 4.23: Nitrogen flowrate for experiment CR-1 at 750°C and 1 bar_g

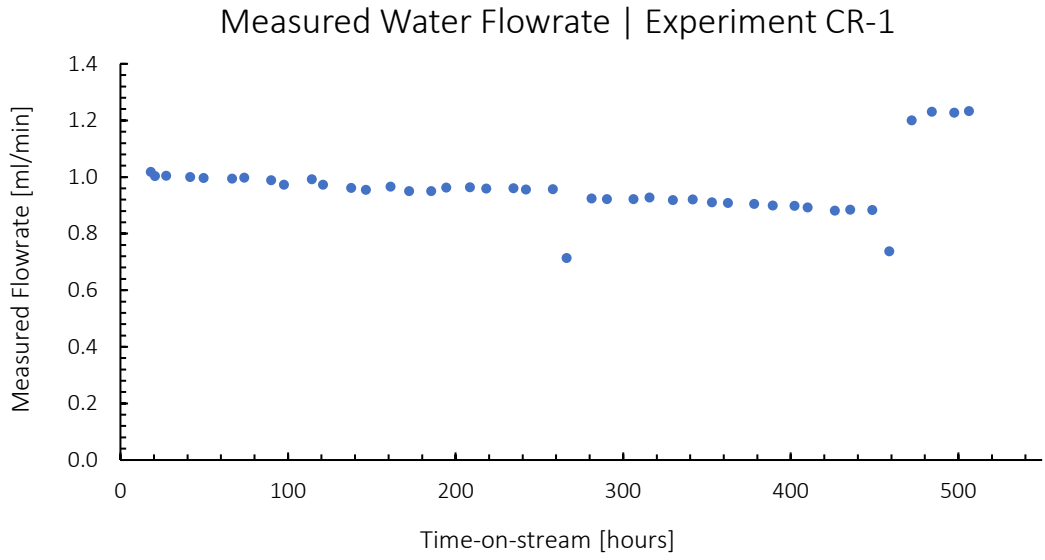

Figure 4.24: Measured water flowrate for experiment CR-1

As indicated previously, the water feed flowrate declined steadily throughout the run, from a steam/carbon ratio of 3.3 to 2.9, before adjustment at roughly 450 h time-on-stream to a value of 3.9 (Figure 4.24). It is worth noting that the variation within this steam/carbon ratio range (3.3 – 2.9) does not seem to effect any noticeable change in catalytic performance. Only with the adjustment at 450 h to an S/C ratio of 3.9, does the system respond slightly as may be anticipated for increased S/C ratio, *viz*., increased carbon balance (Figure 4.20), increased

reforming conversion (Figure 4.19), increased CO_x and decreased C_2 and C_3 selectivities (Figure 4.21).

The measured reactor pressure is presented in Figure 4.25, where it increases linearly from 0.6 to 1.1 bar_g by 460 h time-on-stream. Following the significant adjustment of water feed flow rate at this time (Figure 4.24), the pressure further increased to 1.5 bar_g. It is possible that the constant slow increase in flow-induced reactor back-pressure during the period up to 450 h time-on-stream is an indication of flow restriction due to carbon laydown in the catalyst bed. However, as per the case of water flow rate (Figure 4.24), within the range 0.6 – 1.1 bar_g no noticeable effect was observed on catalytic performance. The influence of increased water flow rate after 450 h and the concomitant increase in reactor backpressure are difficult to separate as both are consistent with the changes in catalytic performance observed at this point.

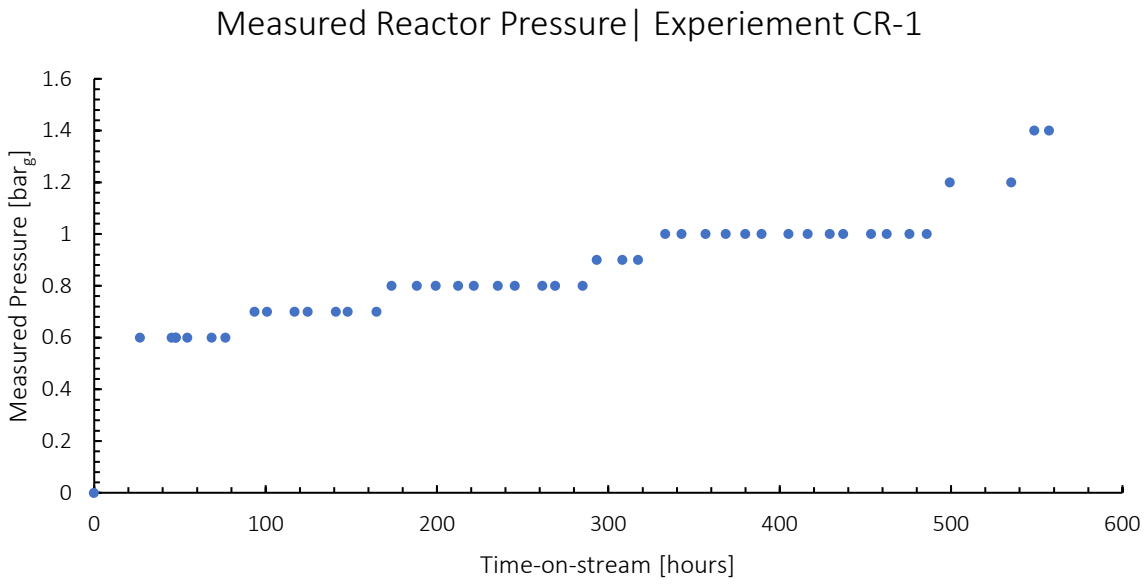

Figure 4.25: Measured reactor pressure data for experiment CR-1

4.2.2.2. Experiment CR-2

CR-2 (standard calcination/reduction procedure as per CR-1) was performed to investigate the effect of the addition, at 208 h on stream, of an air co-feed at 1% of the dry feed flowrate. The experiment was terminated after 290 h due to recorded reactor temperature falling below the 750°C set-point as a result of the furnace heating cartridge failures - the shutdown proceeding as per Section 3.2.5.3 and the catalyst recovered as per Section 3.2.5.4.

Experimental findings for CR-2 are provided in Figures 4.26 to 4.30. It is worth noting that the water flowrate during the experiment (Figure A10.1), though slightly lower at 1.05 ml/min instead of the intended 1.22 ml/min, was constant throughout the experiment, with a S/C ratio of 3.44 close to the average value pertaining in experiment CR-1. Thus, in addition to the effect of air addition, CR-2 also provides a repeat experiment to CR-1 for the first 208 h time-on-stream.

The C_3 and total hydrocarbon conversions are presented below in Figures 4.26 and 4.27, respectively, where both increase to approximately 50% over the initial 'settling-in' period of 20 – 30 h time-on-stream. Both then decline simultaneously to levels roughly half their peak values 208 h time-on-stream – the C_3 conversion at 26% noticeably higher that total hydrocarbon conversion at 18%. By comparison to CR-1, the CR-2 peak conversion levels remain largely constant for an extended period to roughly 100 h in CR-2, during which time C_3 and total hydrocarbon conversions are almost equal, indicating 'complete' reforming during this period. This reforming-rich/cracking-poor behaviour is confirmed also by product selectivities during this period (Figure 4.29). Also noteworthy is that the carbon balance remains essentially 100% throughout this period (Figure 4.28). Beyond roughly 100 h time-on-stream, conversions drop continuously such that by 208 h they are stable at levels of 26% and 18%, respectively for C_3 and total hydrocarbon conversions. Product selectivities also stabilise during this period, the end-point performance of which is very similar to that of CR-1 at the same juncture (end 'linear' deactivation phase – 270 h in the case of CR-1) with the ratio of C_3 conversion to total hydrocarbon conversion being roughly 1.5:1 in both experiments. Also in both experiments, the $CO:CO_2$ ratios of approximately 10 prevail during the peak conversion phase and the carbon balances are essentially 100%, after which both the $CO:CO_2$ ratios decline to stable values in the range 1 – 2 and the carbon balances fall to around 90%. In essence, CR-1 and CR-2 performance closely resemble one another albeit with CR-2 showing an extended period of constant conversion after the initial 'settling-in' period.

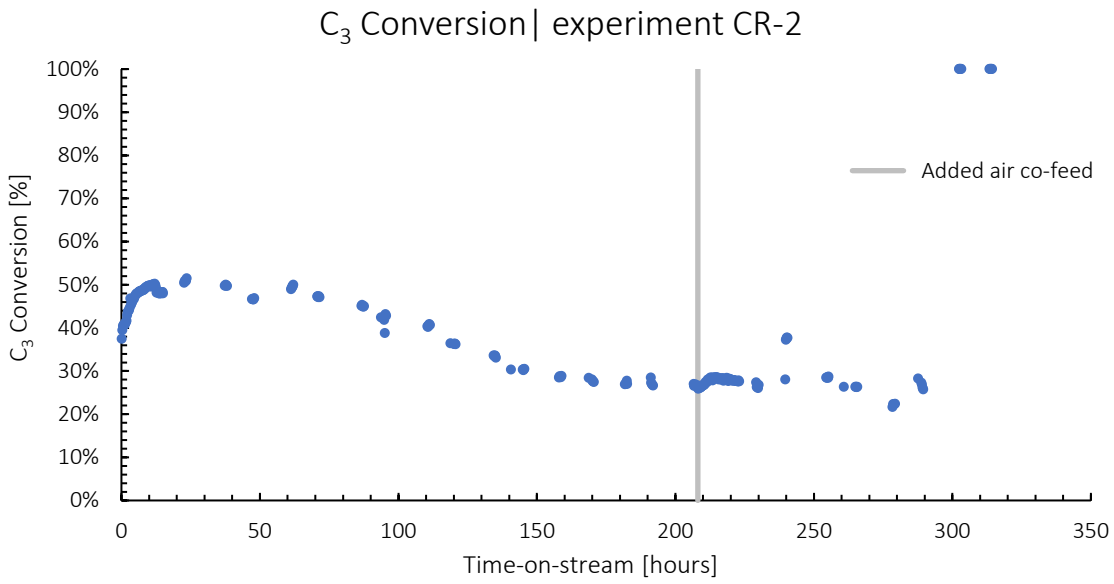

Figure 4.26: C_3 conversion vs. time-on-stream for experiment CR-2 at 750°C and 1 bar_g where the grey line indicates the introduction of an air co-feed at 1% of the dry feed composition

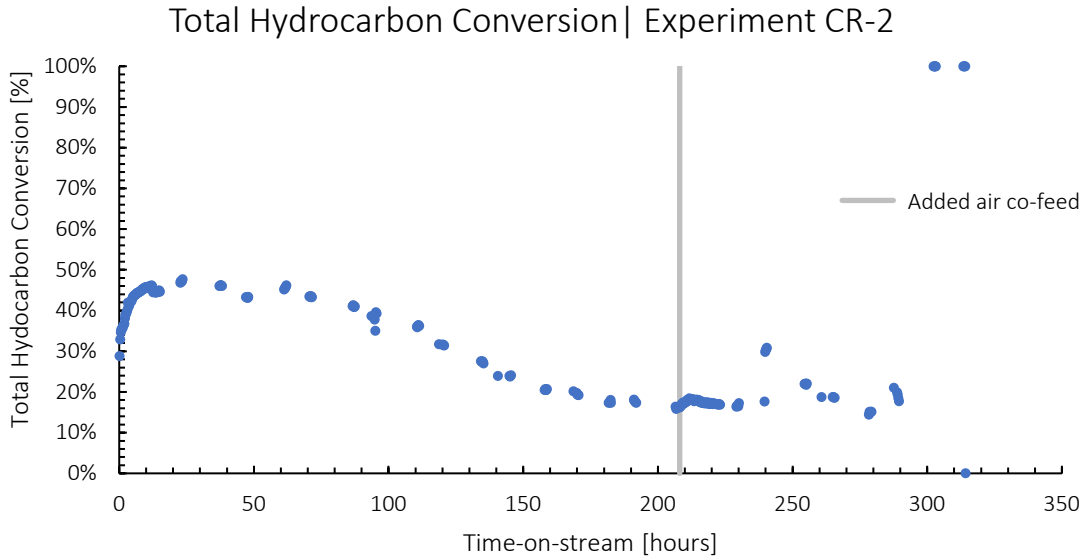

Figure 4.27: Total hydrocarbon conversion vs. time-on-stream for experiment CR-2 at 750°C and 1 bar_g where the grey line represents introduction of an air co-feed at 1% of the dry feed composition

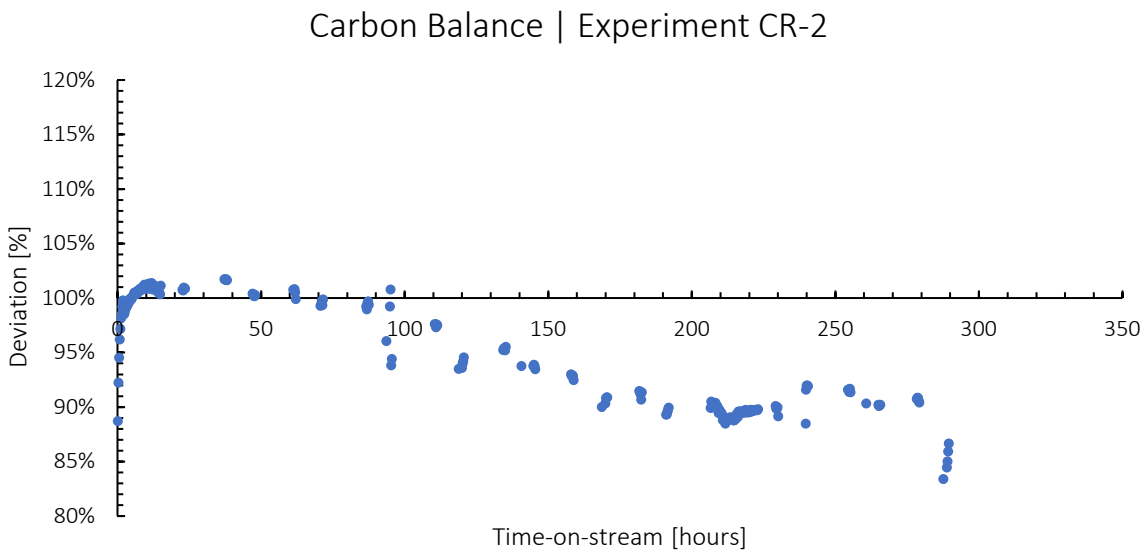

Figure 4.28: Carbon balance vs. time-on-stream for CR-2

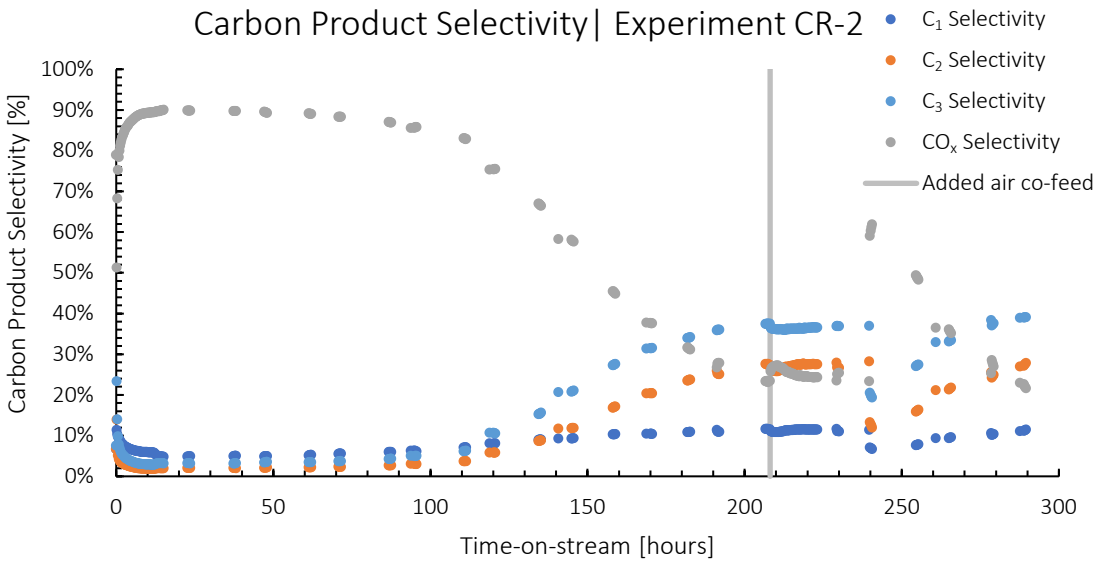

Figure 4.29: Carbon product selectivity vs. time-on-stream for experiment CR-2 at 750°C and 1 bar_g where the grey line represents introduction of an air co-feed at 1% of the dry feed composition

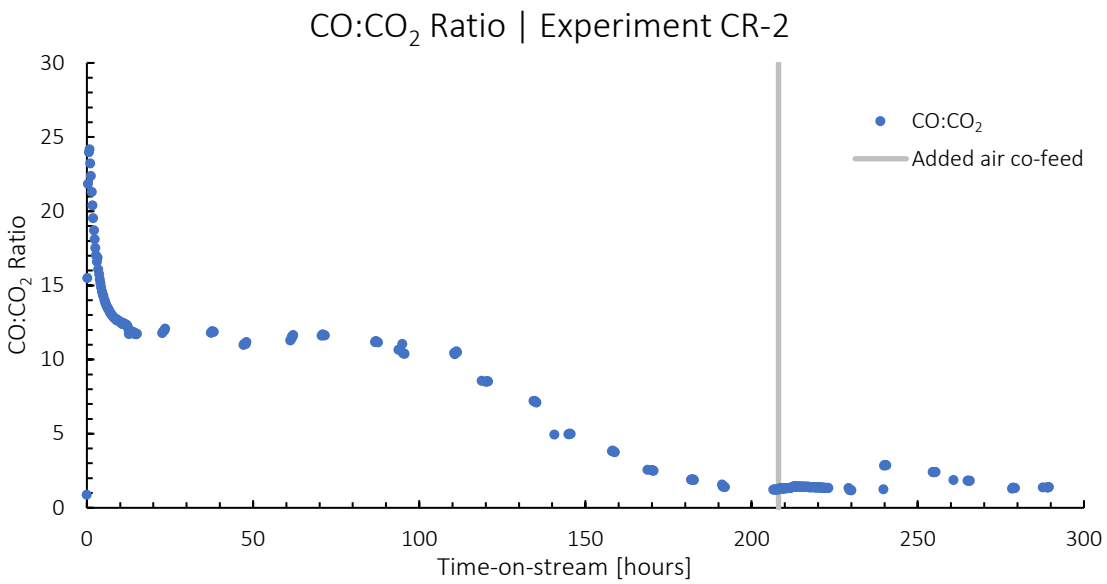

Figure 4.30: $CO:CO_2$ ratio vs. time-on-stream for experiment CR-2 at 750°C and 1 bar_g where the grey line represents introduction of an air co-feed at 1% of the dry feed composition

Initially following the introduction of the 1% air co-feed at 208 h time-on-stream, C_3 and total hydrocarbon conversion increased slightly, concomitantly with product selectivities reflecting improved reforming over cracking activity (Figures 4.29 and 4.30) but the effect is small and short-lived such that by 24 h later performance appears unchanged from before air introduction.

In all the CR-2 performance figures above, the data around 240 h time-on-stream deviates from the general pattern. However, no specific reasons could be ascertained for this momentary deviation.

4.2.2.3. Experiment CR-3

Experiment CR-3 was performed to replicate the effect of the addition of air co-feed at 1% of the dry feed flowrate as per the case of CR-2. The air co-feed was introduced at 127 h time-on-stream. CR-3 was initiated as per the standard procedure as outlined in Section 3.2.5.1.1. The experiment was terminated after 359 h time-on-stream according to the procedure outlined in Section 3.2.5.3 (for the reason of heating cartridge failure) and the catalyst was recovered as per Section 3.2.5.4.

Experimental findings for CR-3 are provided in Figures 4.31 to 4.35. Water flowrate data (see Figure A10.3) indicated that the water flowrate was consistently at 1.22 ml/min, representing a stable S/C ratio of approximately 4 throughout the experiment. In general, the data exhibited greater scatter than the case for CR-1 and CR-2, reasons for which remain undetermined.

The data for the C_3 conversion and the total hydrocarbon conversion are presented below in Figures 4.31 and 4.32, respectively. Prior to the introduction of the air co-feed, the overall performance resembles that of CR-1 more closely than CR-2, in that as for CR-1 there is no extended period of stable high conversions following the initial 'settling-in' phase (i.e., beyond the initial 20 – 30 h time-on-stream). Otherwise, CR-3 closely resembles both CR-1 and CR-2 with peak C_3 and total hydrocarbon conversions of 54% and 42% similar to the prior experiments. However, beyond the initial settling-in period, CR-3 conversions drop steadily to roughly 25% in the case of C_3 conversion and almost to zero in the case of total hydrocarbon conversion, i.e., essentially no remaining reforming activity, by 80 h time-on stream. The carbon balance up to this point, albeit erratic, is close to 100% on average. Product carbon selectivities (Figure 4.34), throughout the period up to the introduction of air co-feed (127 h), closely resemble the same profiles determined for CR-1 and CR-2. The $CO:CO_2$ ratio for CR-3 (Figure 4.35) is likewise similar to that of CR-1 and CR-2, albeit the interim ratio, at maximum conversion, being somewhat higher at 15 than that of 10 for the prior experiments – however, the CR-3 carbon balance at this point is also more erratic.

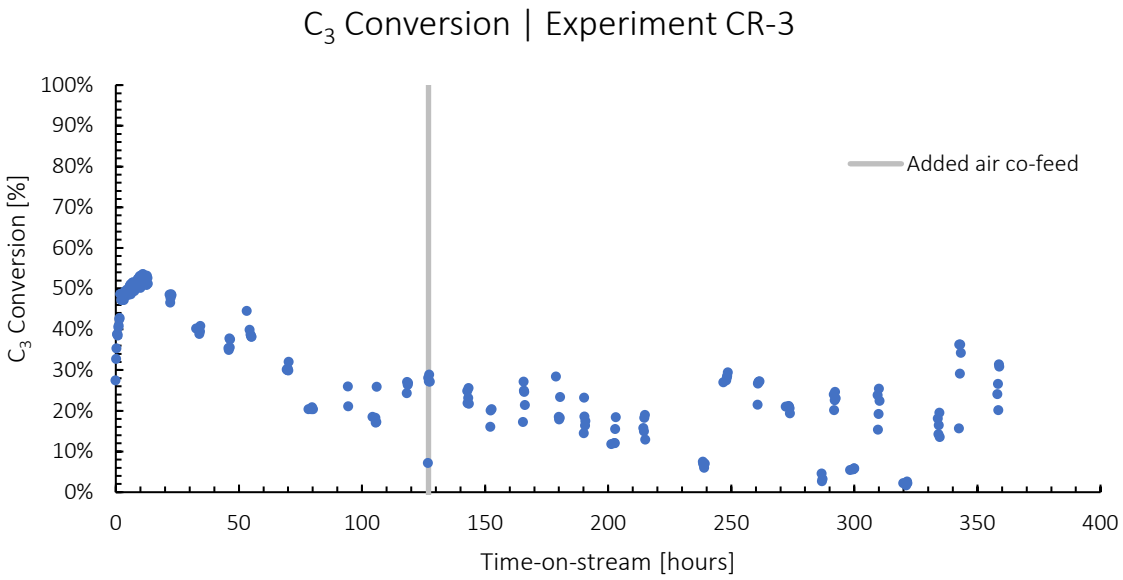

Figure 4.31: C_3 conversion vs. time-on-stream for experiment CR-3 at 750°C and 1 bar_g where the grey line indicates introduction of an air co-feed at 1% of the dry feed composition

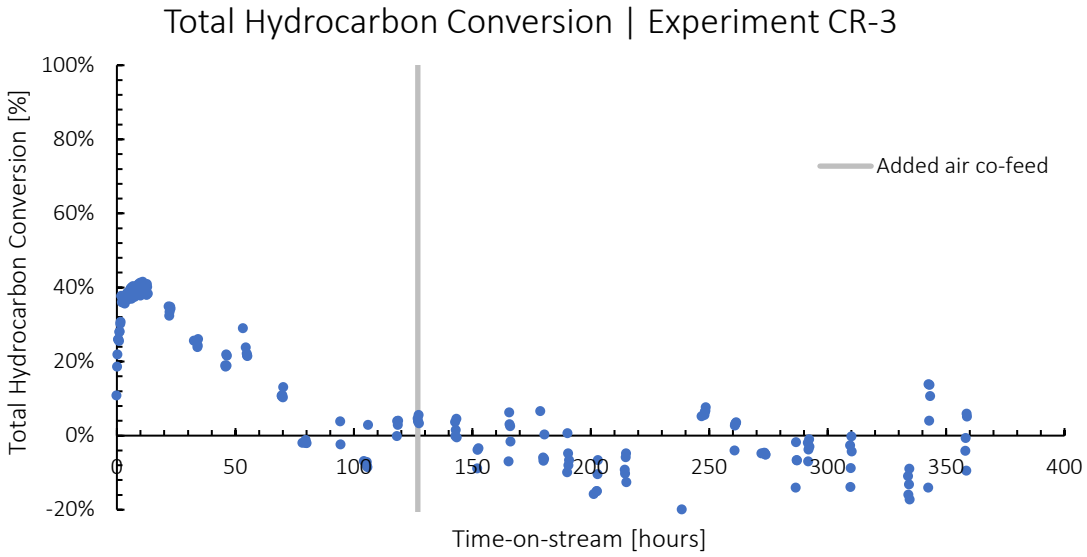

Figure 4.32: Total hydrocarbon conversion vs. time-on-stream for experiment CR-3 where the grey line indicates the introduction of an air co-feed at 1% of the dry feed composition

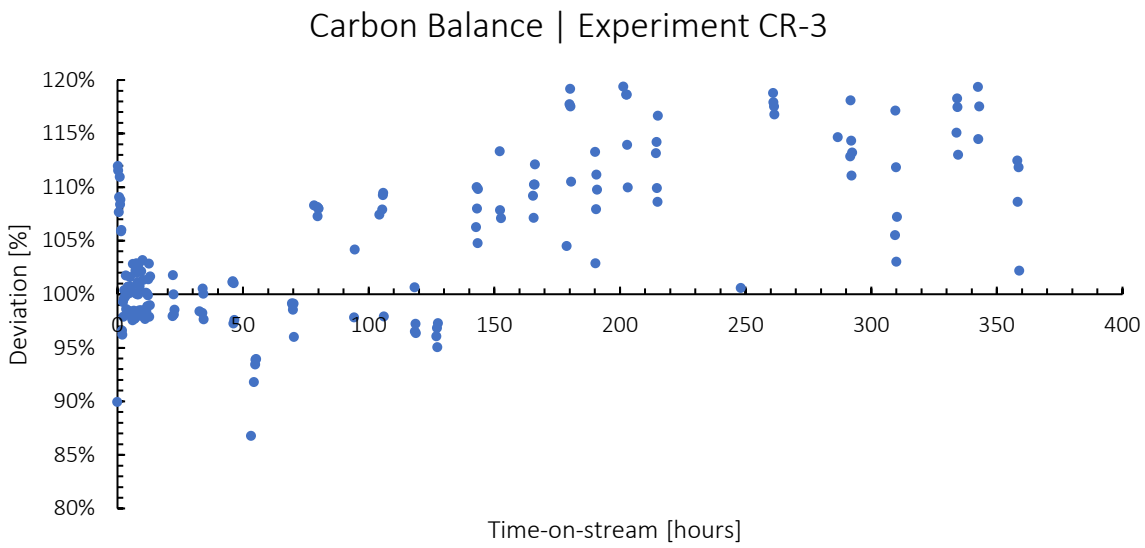

Figure 4.33: Carbon balance vs. time-on-stream for experiment CR-3

Carbon product selectivities are shown in Figure 4.34. Over the first 10 h time-on-stream, the CO_x selectivity increases from 58% to 70%, while C_1, C_2 and C_3 selectivity decreases from 14% to 12%, 13% to 9% and 16% to 10%, respectively. The CO_x selectivity then decreases over the course of 126 h time-on-stream, to nearly 0%. C_1 selectivity increases moderately to 17%, and C_2 and C_3 selectivity increase substantially to 40% and 42%, respectively. Following the addition of the 1% air co-feed at 127 h time-on-stream, there appears to be an increase in CO_x selectivity – though highly scattered, the data points are decidedly higher than the near-0% values from before the addition of the co-feed.

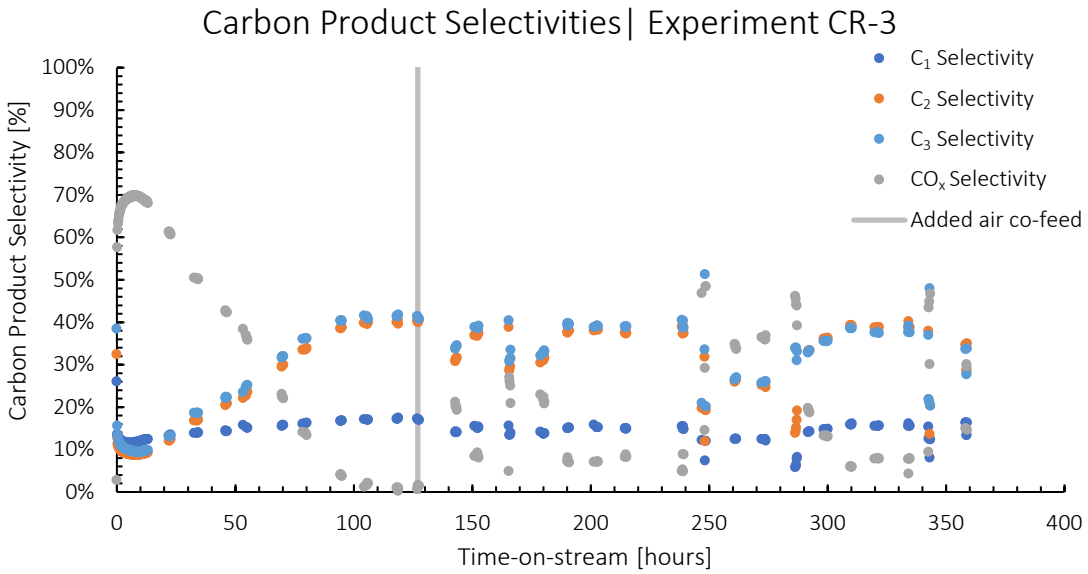

Figure 4.34: Carbon product selectivities vs. time-on-stream for experiment CR-3 at 750°C and 1 bar_g where the grey line represents the introduction of an air co-feed at 1% of the dry feed composition

The $CO:CO_2$ ratio for CR-3 is shown below in Figure 4.35. The $CO:CO_2$ ratio starts at 28 and decreases to a local minimum of 16 at 7 h time-on-stream, before increasing to a local maximum of 17 at 13 h time-on-stream. The $CO:CO_2$ ratio then decreases to ~0.25 by 100 h time-on-stream. Following the addition of the 1% air co-feed, the $CO:CO_2$ ratio appears to increase to ~1.5, indicating that there may be some effect on catalytic activity from the addition of the 1% air co-feed.

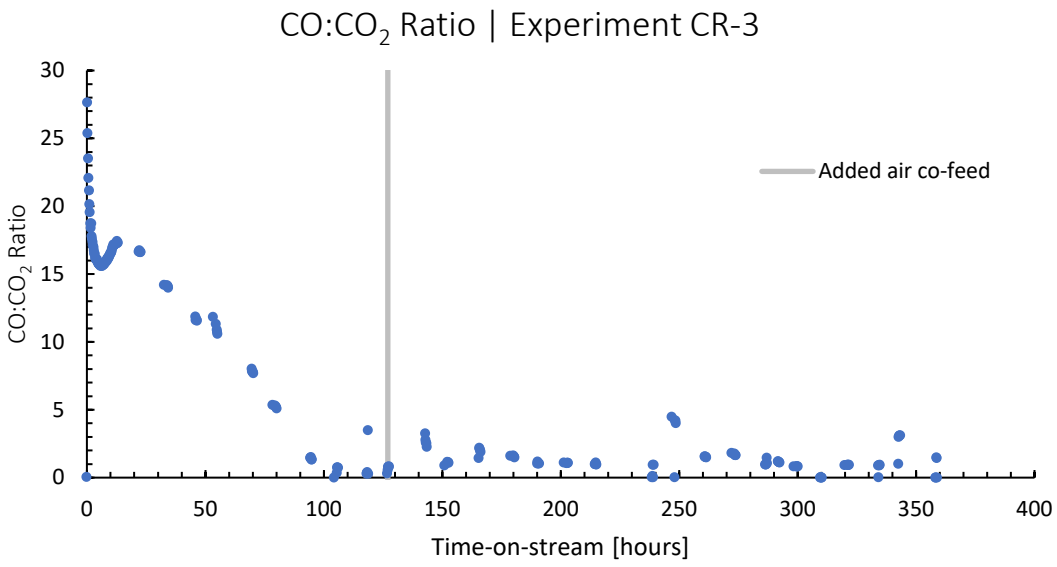

Figure 4.35: $CO:CO_2$ ratio vs. time-on-stream for experiment CR-3 at 750°C and 1 bar_g where the grey line represents the addition of an air co-feed at 1% of the dry feed composition

The effect of the addition of the 1% air co-feed addition did not appear to affect the C_3 conversion (see Figure 4.31), the total hydrocarbon conversion (see Figure 4.32), or carbon product selectivities (see Figure 4.34) in any convincing way, much as was the case for CR-2. The slight increase $CO:CO_2$ ratio (see Figure 4.35) from near-zero to ~1 with the air co-feed addition, possibly indicates some effect, however, the erratic carbon balance throughout the period of air-co-feed makes such a conclusion unreliable. Nonetheless, the CO_x selectivity (Figure 4.34) shows a clear effect despite the erratic carbon balance, albeit an effect perhaps more consistent with simple carbon burn-off – note also the positive carbon balance under conditions of air-co-feed.

4.2.2.4. Experiment CR-4

Experiment CR-4 was performed to investigate the effect of the addition of a larger air co-feed, i.e., at 3% of the total dry feed composition. Also investigated was the effect on catalytic activity of removing the air feed, and the effect increasing the S/C ratio from 4 to 6. The experiment was started following the activation and reduction procedure outlined in Section 3.2.5.1.1. The experiment was terminated after 716 h time-on-stream using the procedure outlined in Section 3.2.5.3, and the catalyst was recovered as per Section 3.2.5.4.

Experimental findings for CR-4 are presented in Figures 4.36 to 4.40. Water flowrate data (Figure A10.3) indicated some deviation from the intended flowrate, which were fully rectified by 300 h time-on-stream.

The general pattern for time-on-stream performance (conversion, selectivity and stability) prior to the introduction of the air co-feed at 220 h time-on-stream is similar to the preceding CR experiments. The total hydrocarbon conversion declines to almost zero just past 100 h time-on stream, leaving only cracking and almost no reforming activity. Worth noting for this experiment is that the carbon balance is stable throughout and close to 100%. Also noticeable in the data are two substantial 'events' at approximately 210 and 410 h time-on-stream, respectively, which despite stable carbon balances show 'spikes' in both conversions and associated disruptions in the pattern of selectivity data. The cause of these 'events' is unknown, however, the experimental data returned to prior values without intervention such that the 'data disruption' associated with these events is simply to be ignored.

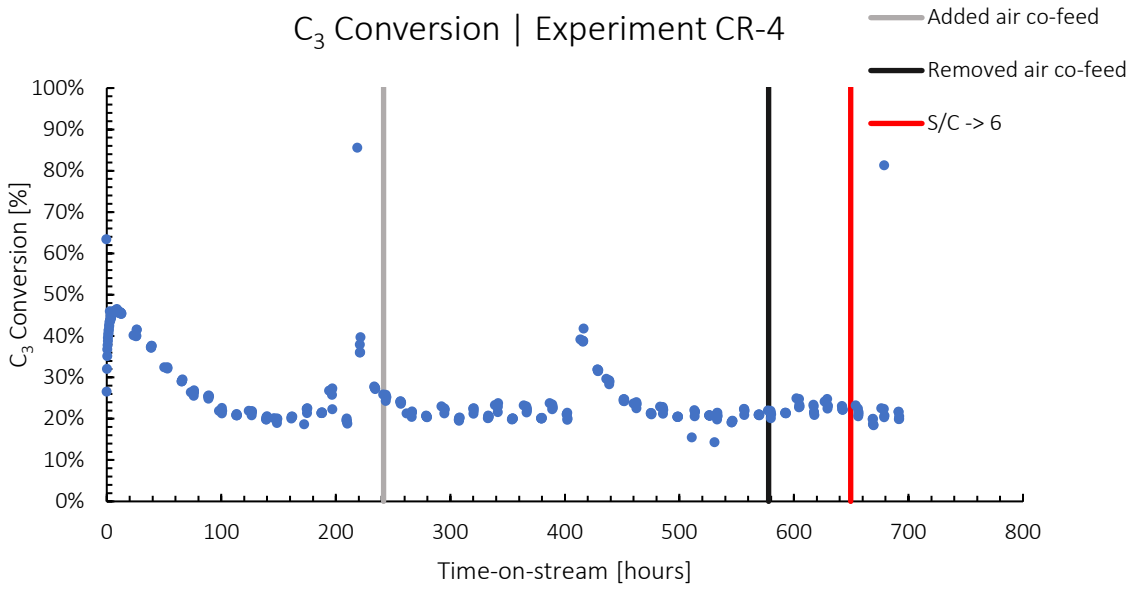

Figure 4.36: C_3 conversion vs. time-on-stream for experiment CR-4 at 750°C and 1 bar_g where the grey line represents the addition of an air co-feed at 3% of the dry feed composition, the black line represents the removal of the air co-feed at 3% of the dry feed composition, and the red line represents changing the S/C ratio from 4 to 6

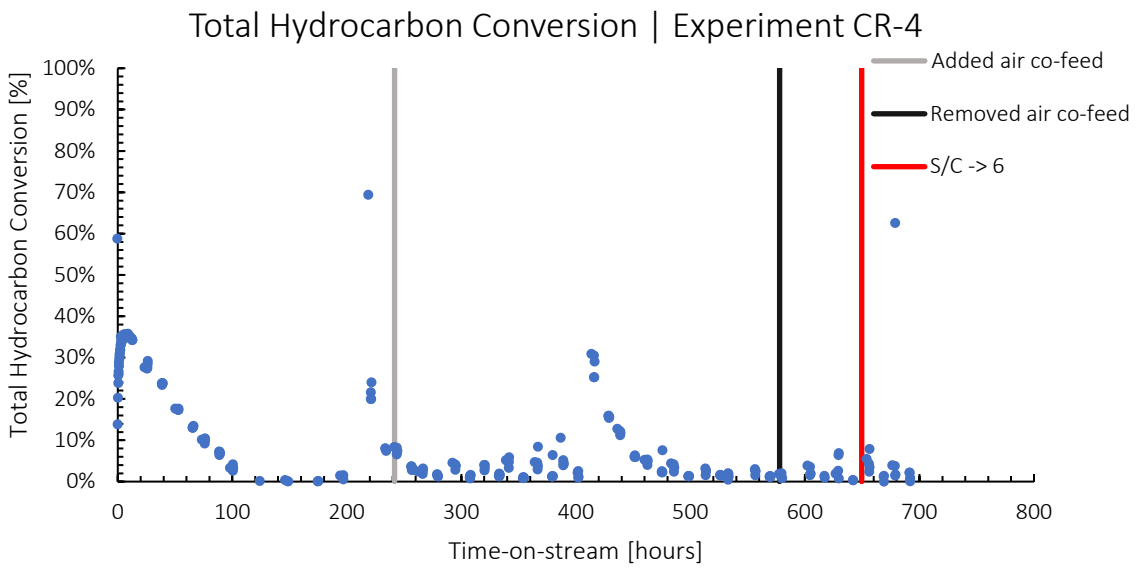

Figure 4.37: Total hydrocarbon conversion vs. time-on-stream for experiment CR-4 at 750°C and 1 bar_g where the grey line represents the addition of an air co-feed at 3% of the dry feed composition, the black line represents the removal of the air co-feed at 3% of the dry feed composition, and the red line represents changing the S/C ratio from 4 to 6

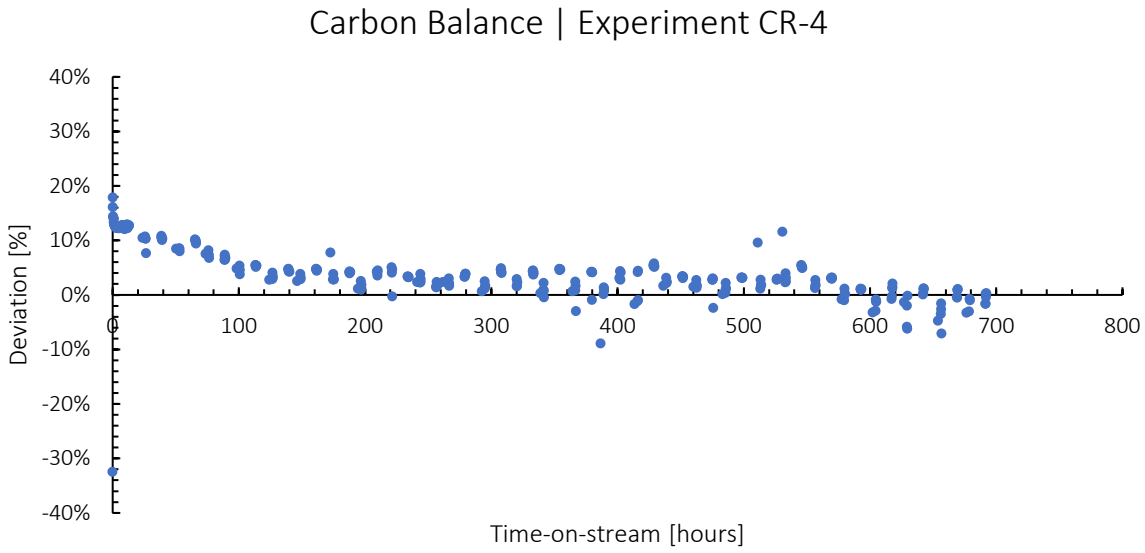

Figure 4.38: Carbon balance vs. time-on-stream for experiment CR-4

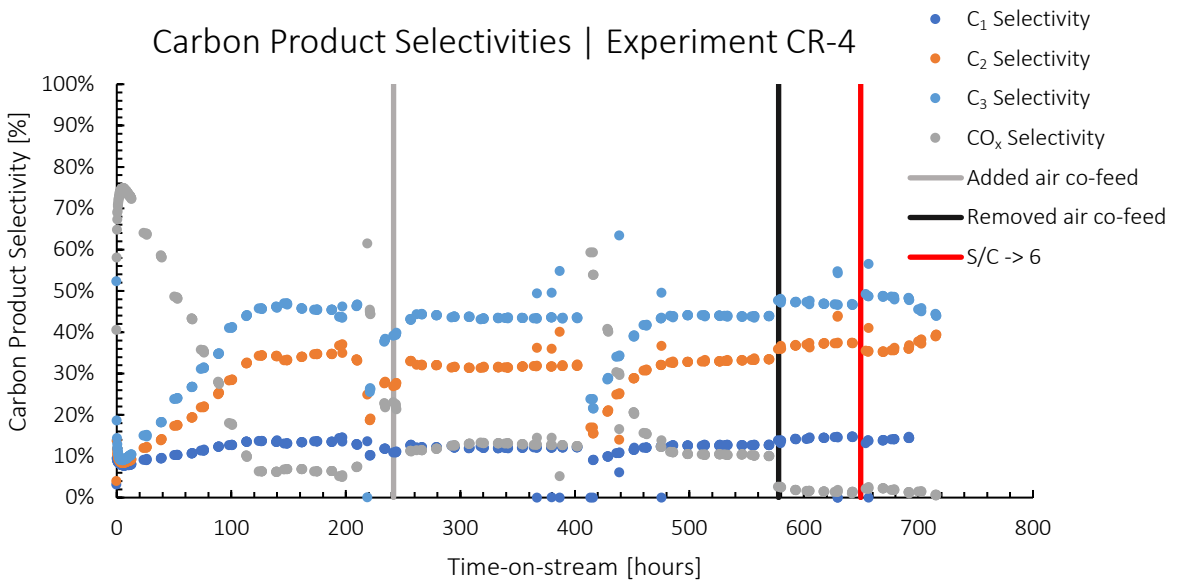

Figure 4.39: Carbon product selectivities vs. time-on-stream for experiment CR-4 at 750°C and 1 bar_g where the grey line represents the addition of an air co-feed at 3% of the dry feed composition, the black line represents the removal of the air co-feed at 3% of the dry feed composition, and the red line represents changing the S/C ratio from 4 to 6

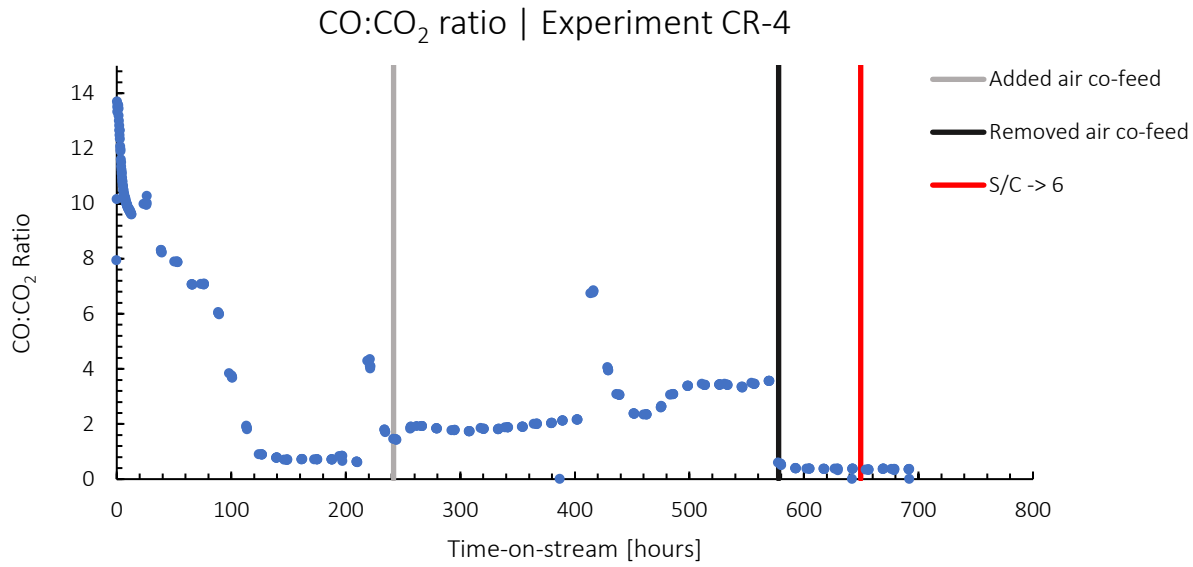

Figure 4.40: CO:CO_2 ratio vs. time-on-stream for CR-4 at 750°C and 1 bar_g where the grey line represents the addition of an air co-feed at 3% of the dry feed composition, the black line represents the removal of the air co-feed at 3% of the dry feed composition, and the red line represents changing the S/C ratio from 4 to 6

The introduction of a 3% air co-feed at 241 h time-on-stream incurred no noticeable change in C_3 conversion (Figure 4.36), and only a slight increase in total hydrocarbon conversion (Figure 4.37). Even so, CO_x selectivity roughly doubles from 6% to 12 % and the $CO:CO_2$ ratio increases from approximately 0.7 to about 1.7 with the introduction of air. Moreover, CO_x selectivity remains constant whilst the $CO:CO_2$ ratio increases further to approximately 3.5 throughout the period during which air co-feed is present. The C_1, C_2 and C_3 selectivities decrease slightly upon air introduction.

Following the removal of the 3% air co-feed at 578 h time-on-stream, both conversions remain essentially unchanged (albeit possibly a slight increase in C_3 conversion) However, there is an abrupt decrease in CO_x selectivity, down from 10 % to 2%, and the $CO:CO_2$ ratio, down from 3.5 to 0.4, while C_1, C_2 and C_3 selectivities increase slightly in similar vein to their decrease upon air addition.

In summary, the introduction of 3% air to the dry feed gas shows essentially the same response as the 1% air introduction in experiments CR-2 and CR-3, however, with the response more pronounced. The presence of air clearly increases CO_x selectivity and, in particular, the $CO:CO_2$ ratio in the product stream. The effect on conversion is less distinct, yet possibly the presence of air lightly favours reforming (total hydrocarbon conversion) over cracking (C_3 conversion). Importantly, the effects of air introduction/removal are seemingly reversible.

The effect of an increase in S/C ratio, from 4 to 6, at 624 h time-on-stream is mostly undiscernible although possibly showing a slight increase in reforming activity (total hydrocarbon conversion – Figure 4.37) and concomitant decrease in cracking activity (C_3 conversion – Figure 4.36) as also evidenced in slight increase in C_3 selectivity and corresponding decrease in C_1 and C_2 selectivities (Figure 4.39). CO_x selectivity (Figure 4.39) and $CO:CO_2$ ratio (Figure 4.40) show negligible change with increased S/C ratio from 4 to 6. These effects are at best small and, taken together with S/C changes in experiments CR-1, CR-2, and CR-3, indicate the system to be largely insensitive to S/C ratio in the range 3 – 6.

4.2.3. Experiments using Calcined Reduced and Steamed Catalyst

4.2.3.1. Experiment CRS-1

Experiment CRS-1 was performed to investigate the effect of the reduction-steaming activation procedure and running a 1% air co-feed from the outset of the experiment. The reduction-steaming pre-treatment is outlined in Section 3.2.5.1.2. The experiment also included the effects of removing the 1% air co-feed and of decreasing the S/C ratio. The experiment was terminated (due to failing furnace heating cartridges) after 546 h time-on-stream following the shutdown procedure outlined in Section 3.2.5.3 and the catalyst was recovered as per Section 3.2.5.4. when the furnace started reading temperatures lower than the set point.

Data for experiment CRS-1 are presented below in Figures 4.41 to 4.45. Measured water flowrate is presented in Figure A10.4. Generally, the measured water flowrate is stable, however, the water pump outright failed around the change of the S/C ratio from 3.5 to 3 (roughly at 525 h time-on-stream), such that data for the S/C ratio of 3 are to be treated with caution.

The carbon balance for the experiment (Figure 4.43), but for the initial 20 – 30 h settling-in period, almost 100% and stable throughout the experiment except for when it falls somewhat after 525 h time-on-stream at the time of the failure of the water pump with the switch to a S/C ratio of 3. This latter observation lends some evidence of carbon retention on the catalyst with falling S/C ratio.

The C_3 conversion and the total hydrocarbon conversion are presented in Figures 4.41 and 4.42, respectively, and it can clearly be seen that catalytic performance differs markedly from that of the calcined/reduced catalysts of experiments CR-1 to CR-4. Notably, over the initial 20 – 30 h time-on-stream period, both conversions decrease from an initial high level, rapidly to a constant low level after this 'settling-in' period – this in contrast to that of the calcined/reduced catalysts where conversions rise from a low value to a medium-level maximum conversion before slowly declining past the 'settling-in' period. After 20 h time-on-stream, both conversions remain essentially stable throughout the experiment but for slight changes upon air removal and S/C ratio changes.

Carbon product selectivities for the experiment are presented in Figure 4.44. These also differ sharply from the time-on-stream profiles for the calcined/reduced catalysts of experiments CR-1 to CR-4. CO_x selectivity starts at 100%, and sharply decreases to 10% over roughly 50 h time-on-stream, while C_1, C_2 and C_3 selectivity concomitantly increase from 0% to approximately 16%, 35% and 35%, respectively. All selectivities remain relatively stable up until 330 h time-on-stream, at which point some change in response to changing reaction conditions in respect of the air co-feed and S/C ratio. The $CO:CO_2$ ratio for CRS-1 is shown in Figure 4.45, starting close to 1 and increasing to a peak of almost 14 over 10 – 20 h time-on-stream, subsequently falling to a roughly constant value of around 3 by 100 h time-on-stream.

The performance data for CRS-1 contrasts with that of experiments CR-1 to CR-4 in that the CRS-1 performance appears to start out at the same point the CR experiments reach only at the end of the their "settling-in" period of 20 – 30 h time-on-stream, i.e. the point of highest conversions and especially of highest reforming activity (total hydrocarbon conversion) is immediately at the start of the CRS-1 experiment (0 h time-on-stream) whereas this situation is reached only after the settling-in period of 20 – 30 h time-on-stream in the case of the CR experiments – also that the peak conversions are significantly higher (almost 100%) in the case of CRS-1 vs. nominally in the range 40 – 60% in the case of the CR experiments. Moreover, that the transition from peak reforming activity (high total hydrocarbon conversion) to minimal reforming activity in the CRS-1 experiment is rapid (10 – 20 h in duration) versus a much slower transition in the case of the CR experiments (generally in the range of 100 – 200 h post peak conversion). These observations are supported throughout also in respect of product carbon selectivities in the case of CRS-1 vs the CR experiments.

Experiment CRS-1 starts with air co-feed from the outset. While it is unlikely to be the cause for the dramatic change in initial time-on-stream behaviour of the CRS system – since CR experiments show little effect on performance in the presence of air or not – it is reflected in the higher CO_x selectivity and $CO:CO_2$ ratio in the CRS-1 effluent stream from the outset. Consequently, the change in performance behaviours of the CRS-1 vs CR systems is likely due to the CRS-1 catalyst having been steamed for several h prior to the start of reaction versus the case for the CR catalysts which are exposed to steam only as part of the feed make-up at the reaction feed stream.

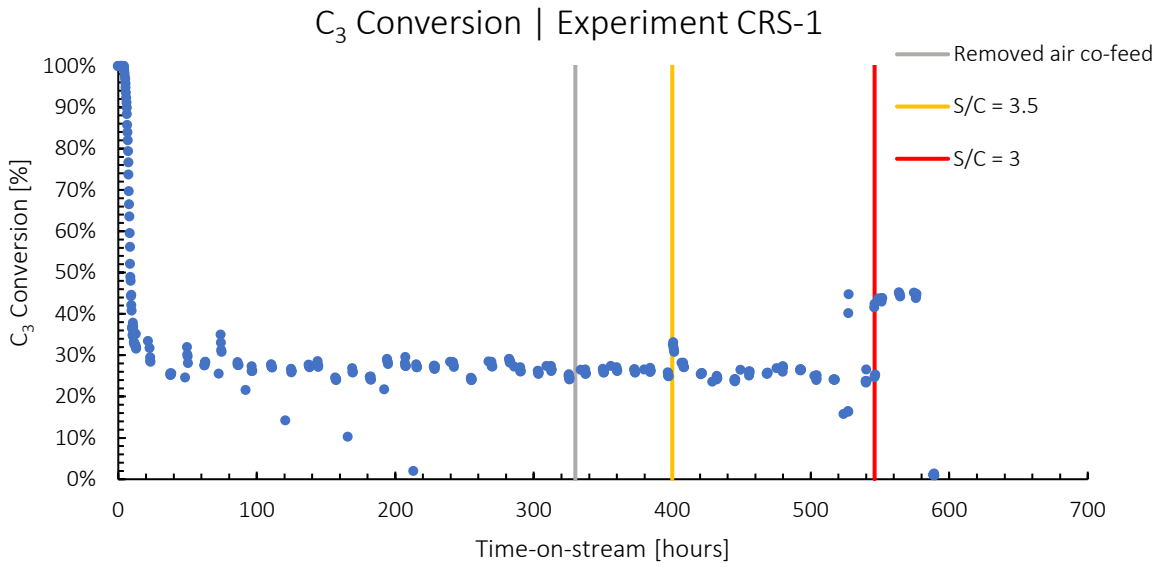

Figure 4.41: C_3 conversion vs. time-on-stream for experiment CRS-1 at 750°C and 1 bar_g where the grey line indicates the removal of the air co-feed at 1% of the dry feed composition, the yellow line indicates changing the stream-to-carbon ratio to 3.5 and the red line indicates changing the S/C ratio to 3

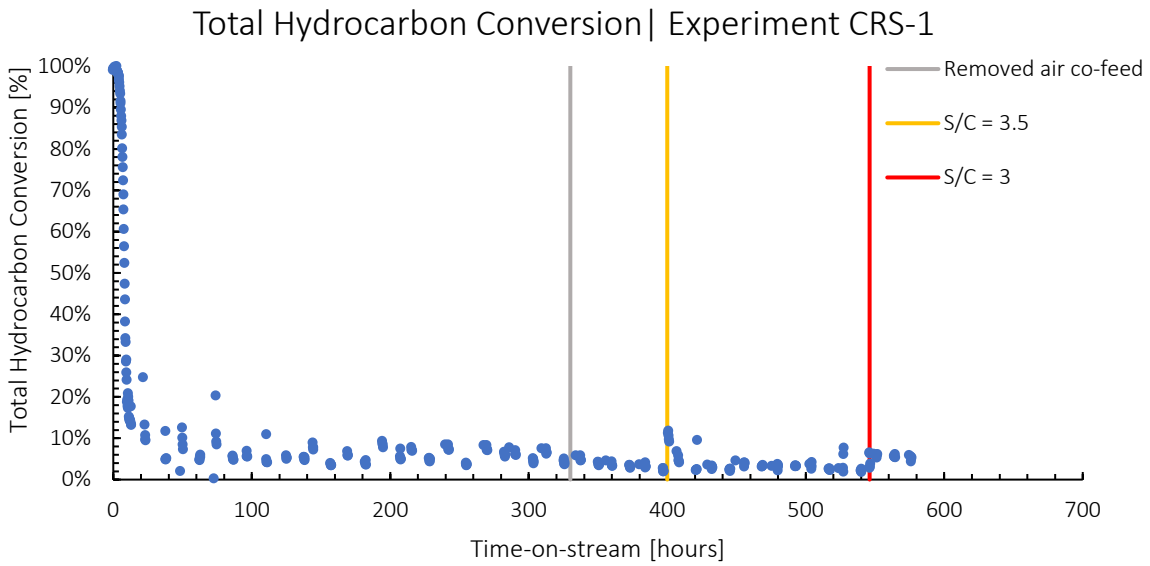

Figure 4.42: Total hydrocarbon conversion vs. time-on-stream for experiment CRS-1 at 750°C and 1 bar_g where the grey line indicates the removal of the air co-feed at 1% of the dry feed composition, the yellow line indicates changing the S/C ratio to 3.5, and the red line indicates changing the S/C ratio to 3

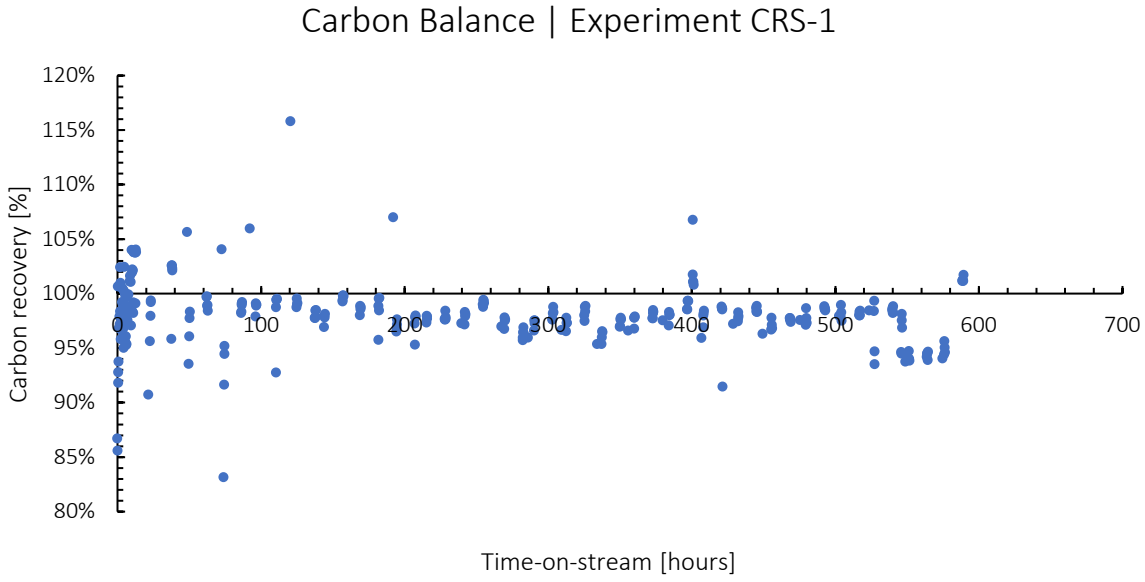

Figure 4.43: Carbon balance vs. time-on-stream for experiment CRS-1

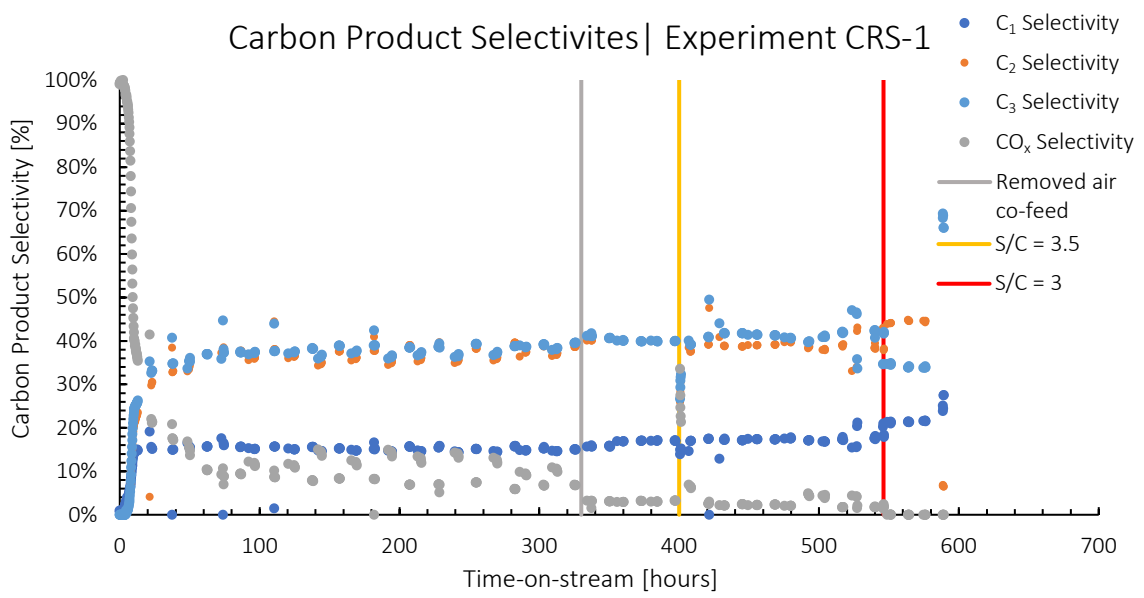

Figure 4.44: Carbon product selectivities vs. time-on-stream for Experiment CRS-1 at 750°C and 1 bar_g where the grey line indicates the removal of the air co-feed at 1% of the dry feed composition, the yellow line indicates changing the stream-to-carbon ratio to 3.5 and the red line indicates changing the S/C ratio to 3

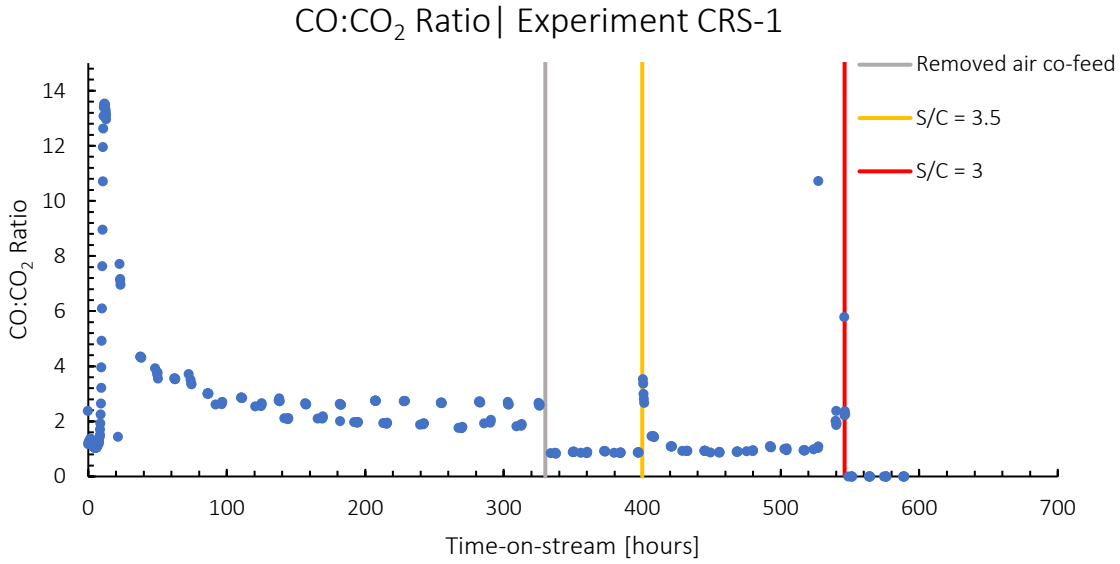

Figure 4.45: $CO:CO_2$ ratio vs. time-on-stream for experiment CRS-1 at 750°C and 1 bar_g where the grey line indicates the removal of the air co-feed at 1% of the dry feed composition, the yellow line indicates changing the stream-to-carbon ratio to 3.5 and the red line indicates changing the S/C ratio to 3

With removal of the 1% air co-feed at 330 h time-on-stream, no change in the C_3 conversion is evidenced, while total hydrocarbon conversion is, perhaps, slightly reduced. The CO_x selectivity decreases noticeably while C_1, C_2 and C_3 selectivities increase proportionally (note, selectivities are normalised and hence a decrease in one will affect an apparent increase in others). Also, the $CO:CO_2$ ratio falls from roughly 2.2 to less than 1 upon air removal from the feed (Figure 4.45). All these effects are consistent with performance changes observed in the case of the CR experiments.

A decrease in S/C ratio to 3.5 at 400 h time-on-stream brings about little change in catalyst performance, if any. Conversions remain essentially stable and possibly a slight decrease in CO_x selectivity and increase in $CO:CO_2$ ratio are observed but performance remains stable.

Due to water pump failure (i.e., S/C ratio declining sharply) upon the intended change of conditions to a S/C ratio of 3, there is little value in any analysis of the data past the change.

4.2.3.2. Experiment CRS-2

Experiment CRS-2 was performed as a repeat experiment of CRS-1, to confirm the different performance of calcination-reduction-steaming procedure of CRS-1 as compared to that of the CR experiments, also a 1% air co-feed from the start of the experiment. The reduction-steaming pre-treatment is outlined in Section 3.2.5.1.2. The experiment was terminated at 165 h time-on-stream (for the reason of failing furnace heating cartridges) following the shutdown procedure outlined in Section 3.2.5.3, and the catalyst was recovered as per Section 3.2.5.4.

Data for CRS-2 are presented in Figures 4.46 to 4.50. Measured water flowrate is presented in Figure A10.5. The measured water flowrate was around 0.83 ml/min rather than the intended 1.22 ml/min, corresponding to an S/C ratio of 2.7 rather than the intended S/C ratio of 4. Water flow was stable throughout the experiment.

The CRS-2 carbon balance is presented in Figure 4.48 and is considered satisfactory throughout the experiment, albeit a slightly positive balance during the first 10 h time-on-stream.

Data for the C_3 conversion and the total hydrocarbon conversion are shown in Figures 4.46 and 4.47, respectively. The general pattern of conversion behaviour prior to the removal of air at 110 h time-on-stream is the same as that for experiment CRS-1, albeit with C_3 conversion slightly lower than the case for CRS-1 and total hydrocarbon conversion falling close to zero after 15 h time-on-stream. Possibly, this may be attributed to the lower S/C ratio prevailing in CRS-2, *viz*., S/C of 2.7, versus the S/C of 4 during CRS-1.

Carbon product selectivities for CRS-2 are provided in Figure 4.49. CO_x selectivity starts at 100%, declining steeply to 8% by 13 h time-on-stream, ultimately to about 4%. C_1, C_2 and C_3 selectivities start at 0% and increase to 17%, 39% and 37% by 13 h time-on-stream, respectively. By 26 h time-on-stream, all selectivities are relatively stable, with C_1, C_2, C_3 and CO_x selectivities at 17%, 40%, 39% and 4%, respectively. Essentially, as per the case for conversion, the time-on-stream behaviour in respect of product selectivities is the same for bothCRS-1 and CRS-2.

The CO:CO_2 ratio for CRS-2 is provided in Figure 4.50, starting out at about 1.9 and increasing to slightly over 6 by 13 h time-on-stream, after which it remains high in the range 8 – 11, but these data exhibit a significant scatter, possibly attributable to the very low reforming activity (total hydrocarbon conversion close to zero), and low CO_x selectivity (roughly 4%) after the first 15 h time-on-stream. Consequently, the CO:CO_2 ratio is subject to significant error at these conditions and is perhaps treated with caution.

In summary, past the initial “settling-in” period of about 15 h, the CRS-2 catalyst is essentially inactive for reforming with only cracking activity apparent. But for the unreliable CO:CO_2 ratio data (discussed above), the general performance of CRS-1 and CRS-2 are similar in all respects.

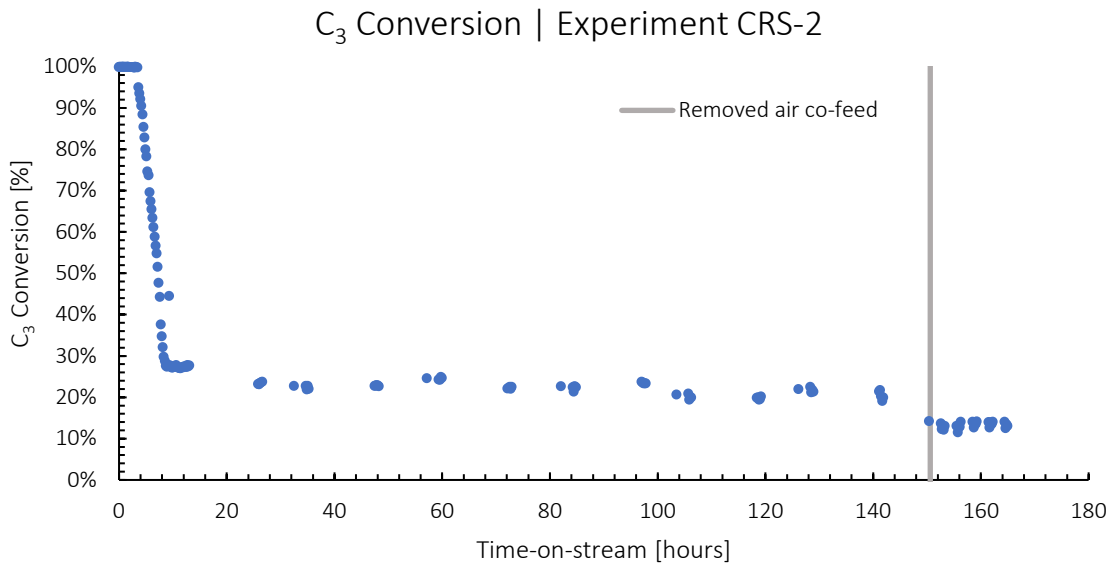

Figure 4.46: C_3 conversion vs. time-on-stream for experiment CRS-2 at 750°C and 1 bar_g where the grey line represents the removal of an air co-feed at 1% of the dry feed composition

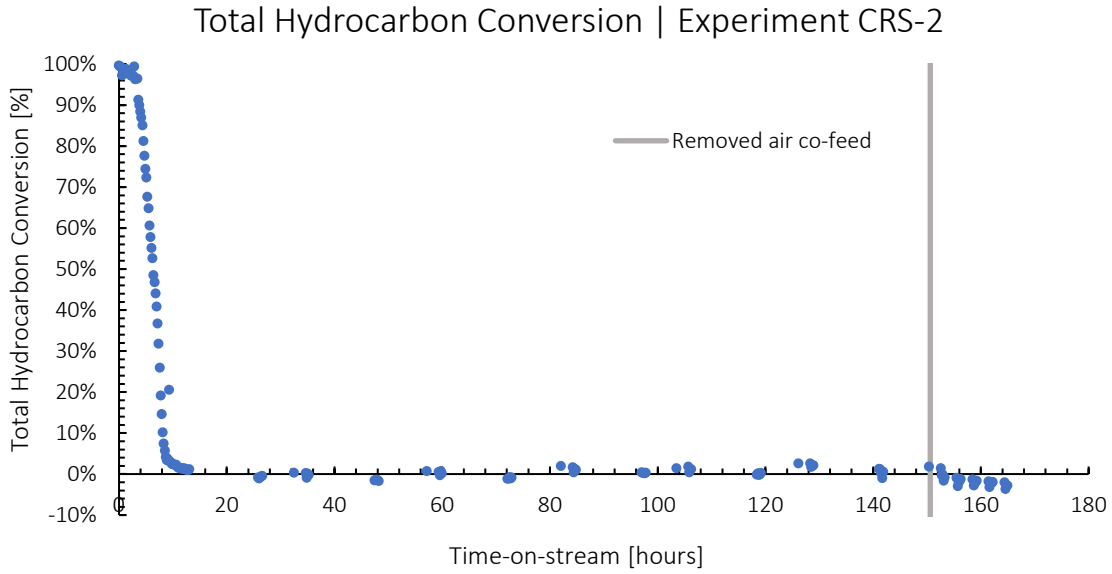

Figure 4.47: Total hydrocarbon conversion vs. time-on-stream for experiment CRS-2 at 750°C and 1 bar_g where the grey line represents the removal of an air co-feed at 1% of the dry feed composition

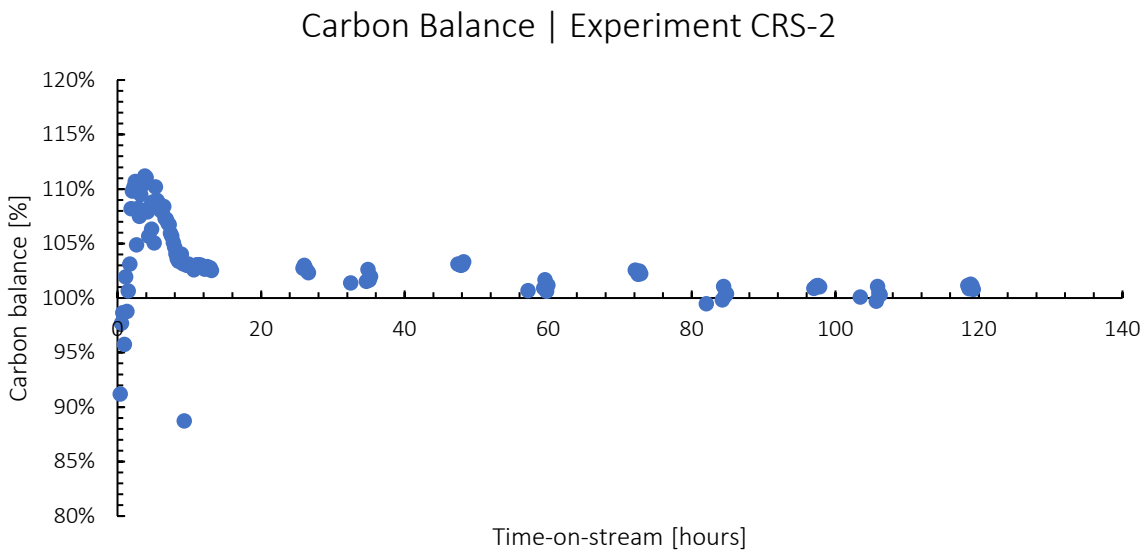

Figure 4.48: Carbon balance vs. time-on-stream for experiment CRS-2

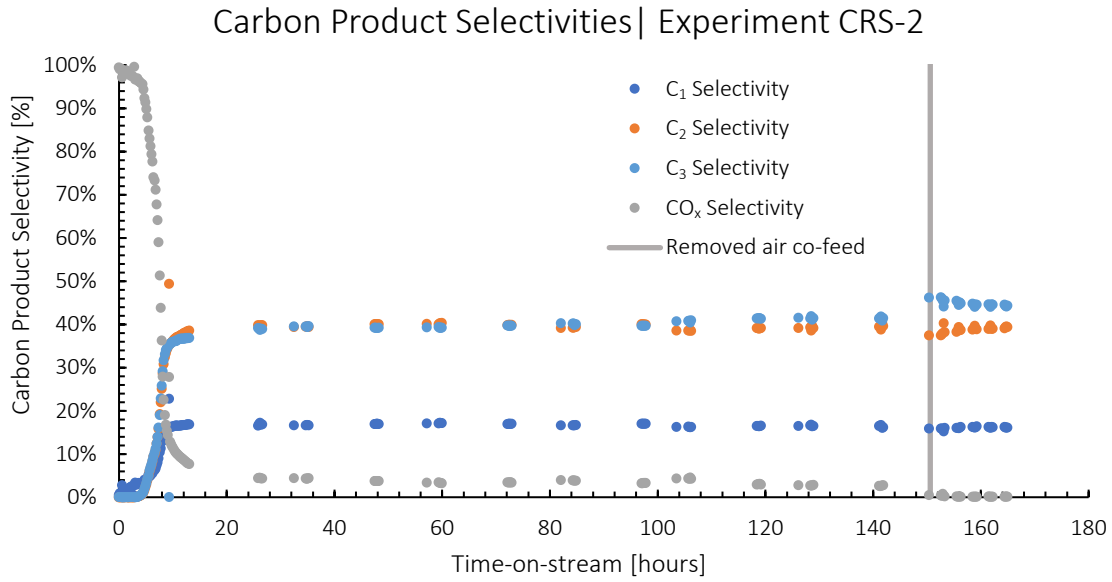

Figure 4.49: Carbon product selectivity vs. time-on-stream for experiment CRS-2 at 750°C and 1 bar_g where the grey line represents the removal of an air co-feed at 1% of the dry feed composition

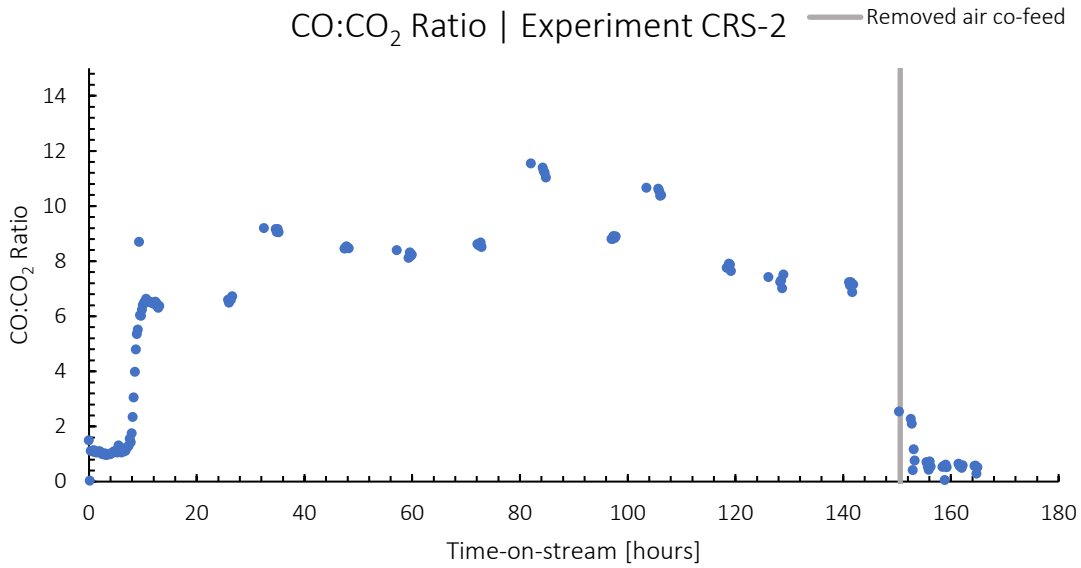

Figure 4.50: CO:CO_2 ratio vs time-on-stream for experiment CRS-2 at 750°C and 1 bar_g where the grey line represents the removal of an air co-feed at 1% of the dry feed composition

Following the removal of the 1% air co-feed at roughly 150 h time-on-stream, but for the C_3 conversion which appears to decrease significantly, the response of other performance metrics is much as in the case of the CRS-1 experiment.

4.3. Spent Catalyst Characterization

4.3.1. Thermogravimetric Measurements

Thermogravimetric measurements of catalyst recovered from experiments were used to determine the extent of carbon deposition on the catalyst. TGA-DTG-DTA curves for oxidation of the recovered catalyst samples are shown in Figures A11.1 to A11.6.

Carbon deposits may be classified into volatile and 'hard coke' components, with volatile components being removed at temperatures between 200°C and 400°C, and hard coke components being removed at higher temperatures, typically around 600°C [44]. Hard coke components may gasify at different temperatures depending on whether the coke is deposited solely on the metal particle, on the metal-support interface, or solely on the support; with proximity to metal particles being associated with greater reactivity and thus gasification at lower temperatures [63].

In order to attain a suitable bed volume for the experiments, the catalyst was combined with SiC of a similar but slightly larger particle diameter so that the catalyst could be sieved out and recovered after the termination of an experiment (see Section 3.2.5.4 on page 26). It was determined visually that a small proportion of this SiC remained in the recovered catalyst, and consequently, the resulting mass loss from the recovered catalyst cannot be regarded as perfectly quantitative of carbon deposition. To partially compensate for this, several analyses were run for each of the recovered catalysts, so that outliers could be excluded, and an average mass loss calculated. Results from these analyses are provided below in Table 4.7.

Table 4.7: Mass loss evaluation of TGA curves of the set of recovered catalysts (see Figures A11.1 to A11.6)

Sample	*Mass loss (%)**	*Time-on-stream (h)*
CR-1	40.2 ± 1.9	498
CR-2	15.3 ± 1.2	289
CR-3	33.8 ± 0.4	359
CR-4	25.3 ± 0.2	715
CRS-1	34.4 ± 0.9	589
CRS-2	29.4 ± 1.8	165

*Indicating the average value and the standard deviation

In CR-1, CR-3 and CR-4, a single large peak in the DTG curve is observed. In CR-2, CRS-1 and CRS-2, a shoulder is observed to the right of the largest peak. In all cases, the largest peak occurs in the region of 600°C, and the presence of a corresponding peak in the DTA curve indicates that an exothermic reaction is occurring, which is consistent with the removal of coke though oxidation. This is also consistent with literature which indicates the removal of hard coke at temperatures in the range of 600°C [55]. The large peak likely corresponds to coke which is deposited on the metal and metal/support interface, whereas the shoulder likely corresponds to coke which is deposited on the support [63].

4.3.2. X-ray Diffraction (XRD)

X-ray diffractograms of the spent catalyst samples were collected to determine the oxidation state of the ruthenium, to ascertain the extent of sintering of the metal/metal oxide particles, and to partially characterise the carbon deposition occurring on the catalyst.

XRD analysis of the spent catalysts was complicated by contamination of the samples with SiC, which was used as a dilutant when the catalyst was packed into the reactor. While much of the SiC was carefully separated from the samples by means of sieving the samples, some remained, and due to the highly crystalline nature of the SiC, it produced very intense reflections in the diffractograms, partially obscuring the reflections of the other compounds. In the diffractograms presented below in Figure 4.51, the SiC reflection peaks have been truncated.

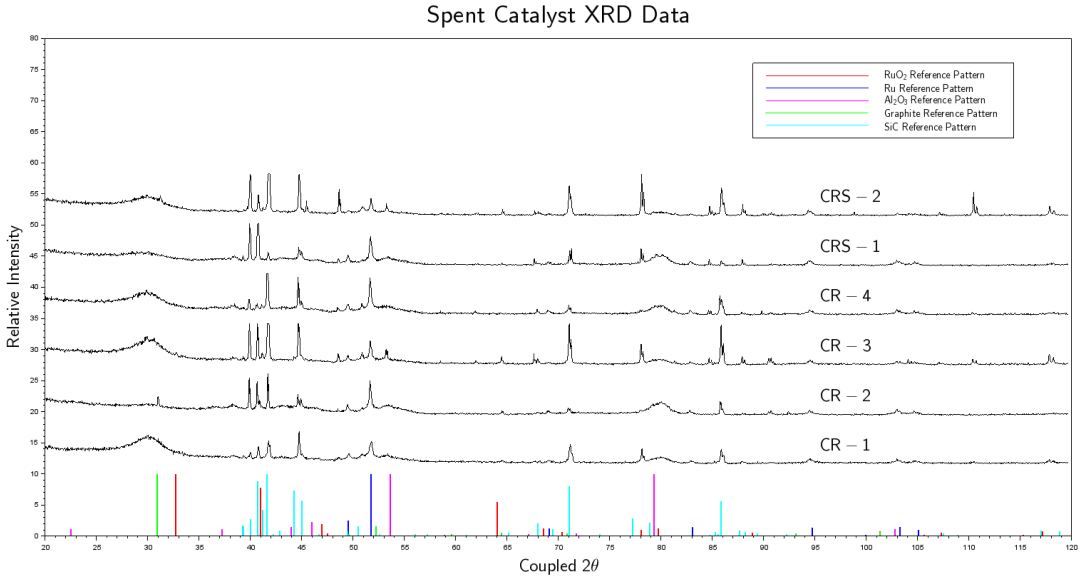

Figure 4.51: XRD patterns for spent catalysts (CR-1, CR-2, CR-3, CR-4, CRS-1, and CRS-2)

Crystallite sizes for Ru/RuO_2 and alumina were calculated for each of the samples using the clearest peak and reported in Table 4.8 below. The pattern from the diffractograms indicated that the Ru had remained reduced, and essentially no reflections were observed for RuO_2. Crystallite size was in the region of 50 nm for CR-2, CR-3, CRS-1, and CRS-2, while CR-1 reported a smaller crystallite size and CR-4 reported a larger crystallite size. No other variable appeared to correlate to this difference, and so the most likely explanation for this difference is experimental measurement error due to overlap with the SiC reflection peaks. Sintering of the Ru metal does not appear to be occurring, as time-on-stream does not appear to be correlated to Ru crystallite size. A reflection peak was observed for graphitic carbon for all the samples, clearly indicating that graphitic carbon accounts for a significant proportion of the coking of the catalyst.

Table 4.8: XRD Crystallite Sizes and Components of the Spent Catalyst Samples calculated using Scherrer equation

Sample	*Crystallite Size (nm)*			*Time-on-stream (h)*
	Ru	Al_2O_3	C	
CR-1	33.6	12.0	3.79	498
CR-2	53.8	73.0	81.9	289
CR-3	51.6	12.0	4.29	359
CR-4	76.0	9.82	5.62	715
CRS-1	49.1	6.99	4.72	589
CRS-2	45.2	8.74	6.85	165

4.3.3. Transmission Electron Microscopy

TEM images were collected to compare with the fresh catalyst samples, to observe any morphological changes occurring in the particles and to also characterise the deposition of carbon on the sample.

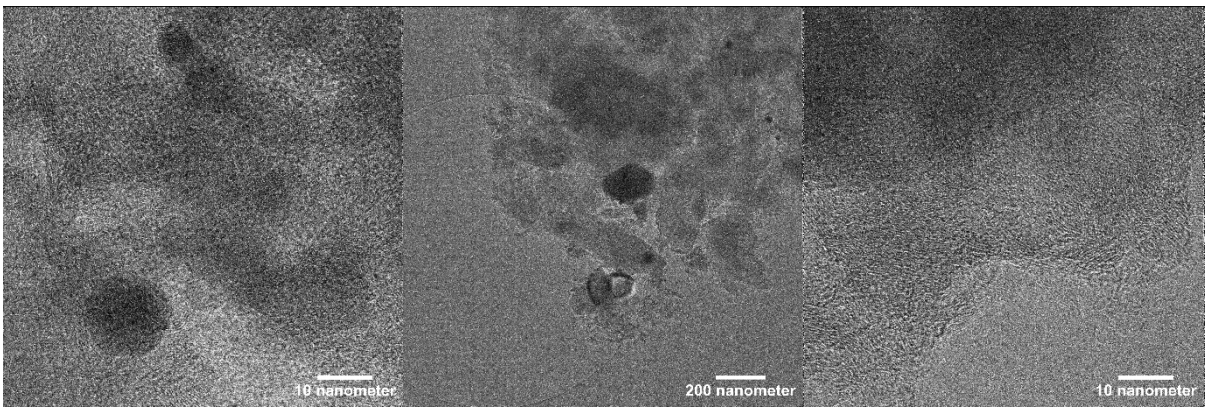

Figure 4.52: TEM Images of CR-1 Spent Catalyst

TEM images of the recovered spent catalyst from CR-1 are shown above in Figure 4.52. CR-1 was an experiment started using the standard reduction procedure. The leftmost image displays Ru metal particles fully encapsulated in graphitic carbon. The middle image shows several Ru metal particles, also fully encapsulated in graphitic carbon. The rightmost image displays more graphitic carbon, where the d-spacing can be observed.

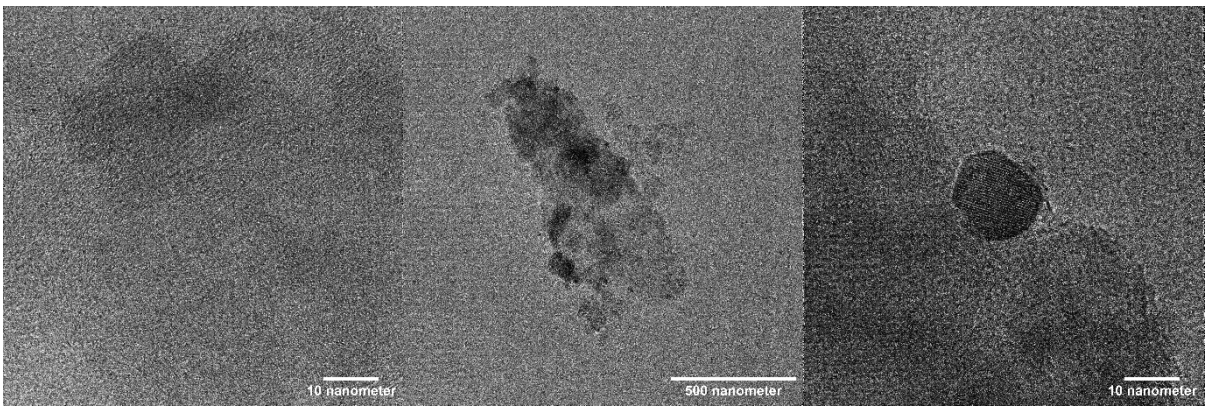

Figure 4.53: TEM Images of CR-2 Spent Catalyst

TEM images of the recovered spent catalyst from CR-2 are shown above in Figure 4.53. CR-2 was an experiment started using the standard reduction procedure. The leftmost image displays graphitic carbon encapsulating a nanoparticle. The middle image displays Ru particles on the support, wherein the Ru particles are encapsulated by a thin layer of graphitic carbon. The rightmost image displays an Ru particle where the d-spacing is clearly visible, mostly encapsulated in graphitic carbon.

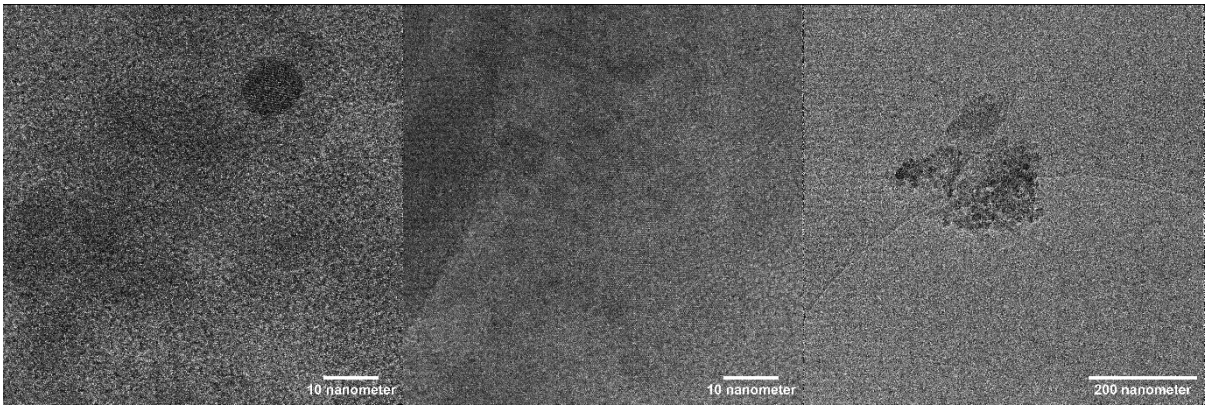

Figure 4.54: TEM images of CR-3 Spent Catalyst

TEM images of the recovered spent catalyst from CR-3 are shown above in Figure 4.54. CR-3 was an experiment started using the standard reduction procedure. The leftmost image displays an Ru nanoparticle encapsulated by graphitic carbon. The middle image displays graphitic carbon on the surface of a larger Ru particle. The rightmost image displays some of the support.

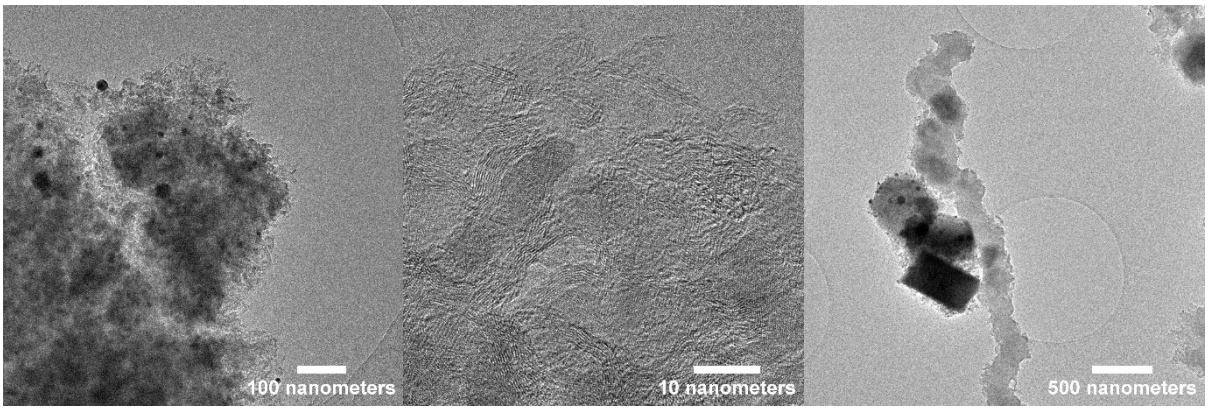

Figure 4.55: TEM images of CR-4 Spent Catalyst

TEM images of the recovered spent catalyst from CR-4 are shown above in Figure 4.55. CR-4 was an experiment started using the standard reduction procedure. The leftmost image displays small Ru particles on the support encapsulated by graphitic carbon. The middle image displays the graphitic carbon where the d-spacing of the carbon is visible. The leftmost image displays several Ru particles next to a carbon nanotube.

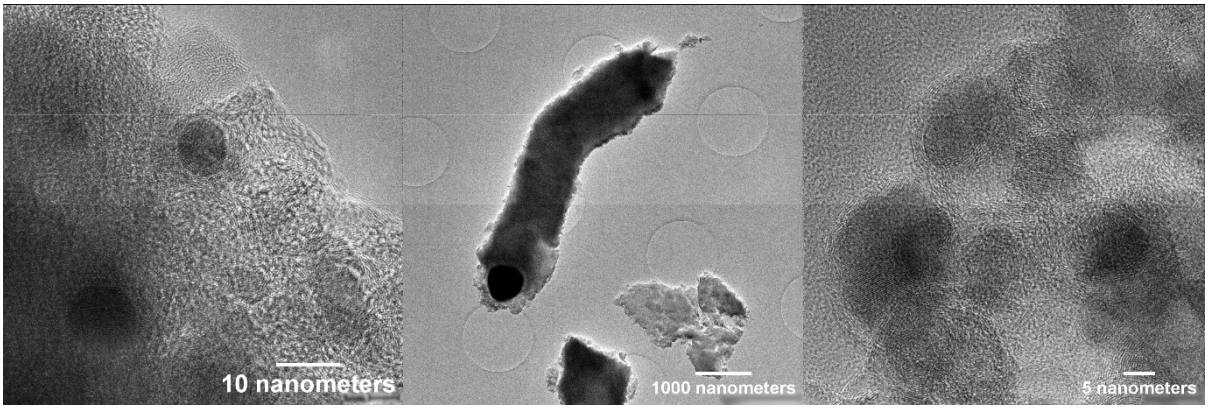

Figure 4.56: TEM images of CRS-1 Spent Catalyst

TEM images of the recovered spent catalyst from CRS-1 are shown above in Figure 4.56. CRS-1 was an experiment started using the reduction then steaming procedure. The leftmost image displays Ru particles encapsulated in graphitic carbon. The middle image displays a carbon nanotube growing off an Ru particle. The rightmost image displays several platelets, which have been encapsulated by graphitic carbon.

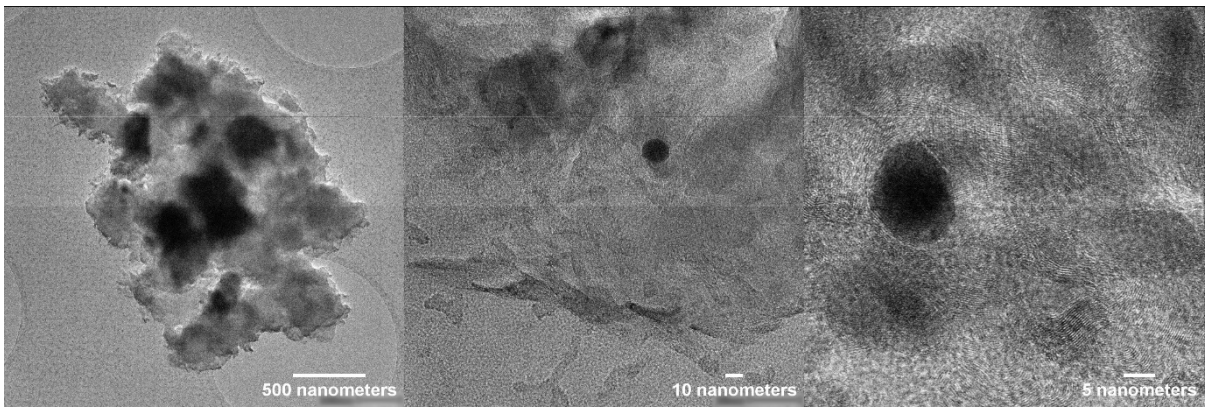

Figure 4.57: TEM Images of CRS-2 Spent Catalyst

TEM images of the recovered spent catalyst from CRS-2 are shown above in Figure 4.57. CRS-2 was an experiment started using the reduction and steaming procedure. The leftmost image displays several larger Ru particles encapsulated in graphitic carbon. The middle image displays a small Ru particle in a large quantity of graphitic carbon. The rightmost image displays a small Ru particle encapsulated in graphitic carbon, where the d-spacing of the carbon is visible.

5. Discussion

The overall objective of this study was to investigate the mechanism of deactivation in steam reforming on Ru/Al_2O_3 and to further investigate the effect of the introduction of an air co-feed to ascertain its effects on deactivation and determine if it extends catalytic lifespan. Further to this, the study sought to investigate the effects of S/C ratio on the rate of catalytic deactivation.

This study hypothesised that carbon deposition is the primary mechanism of deactivation in steam reforming on Ru/Al_2O_3 catalysts, and that co-feeding air will avail free oxygen at the catalytic surface in the catalyst bed, facilitating the removal of carbon from the surface of the catalyst, thus availing a greater active surface area, thereby mitigating deactivation. This study sought to investigate this hypothesis by synthesising and characterising a Ru/Al_2O_3 catalyst, performing several experimental propane steam reforming runs using that catalyst, varying certain conditions to investigate if they mitigate deactivation, and characterising the spent catalyst to ascertain the mechanism of deactivation.

This study commenced with the synthesis of a 5 wt% Ru/Al_2O_3 catalyst. The prepared 5 wt% Ru/Al_2O_3 catalyst was subjected to various treatments before the initiation of the propane steam reforming runs. The first was a reduction procedure, and the second was a steaming and oxygenation procedure. Some samples of catalyst were prepared by following the procedures and then collecting the catalysts without performing any steam reforming. The reduction procedure was found to have a limited effect on the physicochemical properties of the catalyst, with moderate degradation of the support and complete reduction of the RuO_2 to Ru metal. In contrast, the reduction and steaming procedure was found to have incurred significant dispersal of the Ru metal, with a substantial decrease in particle size and a complete re-oxidation of the Ru metal back to RuO_2.

The 'base' 5 wt% Ru/Al_2O_3 catalyst was prepared by means of wetness impregnation as a synthesis method, followed by calcination up to 800°C. Ru metal loading was confirmed at 5 wt% by means of ICP-OES analysis. XRD indicated conversion of $RuCl_3$ to RuO_2, and a RuO_2 crystallite size of 46.9 nm. TEM analysis indicated a broad PSD, with particles of diameter in the range of 733 ± 579 nm. This contrast between crystallite size as calculated using the Scherrer equation and the PSD from TEM analysis is indicative of conglomeration of crystallites within the sample. BET analysis indicated a surface area of 169 m^2/g, a moderate reduction in the surface area of the support reported by the manufacturer of 185 – 215 m^2/g. TPO indicated that some chlorine may have remained during calcination. TPR indicated complete reduction occurred at 320°C. This reduction temperature was used in the reduction procedure for CO chemisorption, which combined with the ICP-OES confirmed metal loading, indicated metal dispersion of 2.9%. This low metal dispersion value may have been anticipated due to the relatively high weight loading of 5% Ru metal, but is lower than values reported in literature for Ru/Al_2O_3 catalysts with the same weight loading [62], suggesting that either the use of wetness impregnation instead of incipient wetness impregnation, or the relatively high

calcination temperature, may have had an adverse effect on metal dispersion. Overall, characterisation indicated a catalyst with the correct anticipated metal loading, limited degradation of the support, with large, conglomerated metal oxide particles.

The catalyst prepared using the in-situ reduction procedure was confirmed by XRD to have fully reduced the Ru metal, which was anticipated given the results from the TPR of the fresh calcined catalyst. XRD analysis via the Scherrer equation showed an increased crystallite size in the sample of 49.7 nm. TEM analysis indicated a PSD of 693 ± 486 nm, indicating that the conglomeration which was found in the fresh calcined catalyst sample remained in the reduced catalyst sample, but that there was a reduced distribution towards larger particles. BET analysis indicated a surface area of 137 m^2/g, a reduction in surface area from the fresh calcined catalyst attributable to the greater time spent at a higher temperature. Overall, the various characterisation techniques used indicated limited morphological changes from the fresh calcined catalyst, with limited degradation of the support, with remaining with large, conglomerated metal particles.

The catalyst prepared using the in-situ reduction and steaming/oxygenation procedure was confirmed by XRD to have oxidised the Ru metal back to RuO_2. XRD analysis indicated an RuO_2 crystallite size of 29.3 nm, a reduction from both the fresh calcined catalyst and the reduced catalyst. TEM analysis indicated a PSD of 311 ± 313 nm, indicating a reduced degree of conglomeration and significantly reduced distribution towards larger particles, in comparison to the fresh calcined catalyst and the reduced catalyst. Furthermore, TEM images indicated a significant morphological change in the catalyst, with the formation of many smaller RuO_2 platelets, which may have increased surface area for the sample. BET analysis indicated a surface area of 97.6 m^2/g, a decrease attributable to the greater time spent at a higher temperature and greater exposure to steam at a higher temperature. Overall, characterisation indicated a substantial degree of morphological change in comparison to the fresh calcined catalyst and the reduced catalyst, with further degradation of the support, and with substantially smaller particles and crystallites which were re-oxidised to RuO_2.

Several investigative propane steam reforming experiments were undertaken. First was a blank experimental run to ascertain background thermal activity. Second were a series of runs using catalyst which was reduced in the reactor. Third was a pair of experiments in which the catalyst was steamed and oxygenated following the reduction treatment, co-feeding of air and changing the S/C ratio were varied to investigate their effects on catalytic activity and deactivation.

The blank experimental run was performed under standard reaction conditions to ascertain the thermal background activity of the experimental apparatus. The blank reactor run indicated that in the absence of catalyst, there was a degree of cracking activity, with approximately 15% of propane being cracked, with a selectivity of 45% towards propene, 37% towards C_2 products and 16% towards methane. In the region of 2% was converted to CO_x products, indicating that reforming activity was effectively negligible.

Four experiments were performed with the calcination/reduction start-up procedure, codenamed CR-1, CR-2, CR-3, and CR-4. The behaviour observed in these runs followed a three-stage pattern – a first "settling-in"/restructuring phase, typically spanning 10 – 20 h, during which time there was a clear increase in conversion, reflected in both the C_3 conversion and the total hydrocarbon conversion. This was succeeded by a second phase of gradual and progressive deactivation, followed by a third phase, in which the catalyst was essentially completely deactivated to the reforming reaction.

The first phase started with C_3 conversion at 34 ± 8%, increasing to a peak at 54 ± 6%, and with total hydrocarbon conversion starting at 23 ± 11%, increasing to 43 ± 5%. The time over which the change in conversion occurred (10 – 20 h) is better explained by catalytic restructuring than explained by residence time in the reactor system, or a similar experimental artifact. There are two likely possibilities to explain the restructuring – the restructuring could involve the production of ruthenium-carbon compounds as an active phase or may have involved the production of RuO_2 via the presence of steam. The carbon balance was often negative over the initial time-period, supporting that the restructuring may have involved carbon deposition. It should be noted that, without having terminated an experiment at exactly this point, it is not possible to have determined the state of the catalyst. Moreover, as carbon deposition would likely have already occurred, if RuO_2 had been produced, it may well have been reduced during the cooling period, in any case.

The second phase proceeded over an extended time-on-stream, with the continued decrease of C_3 and total hydrocarbon conversion. This period spanned a period of 100 – 250 h, indicating a degree of variability in the rate of deactivation. This period of deactivation was likely caused by continual carbon deposition, leading to a loss of active catalytic surface area. The deposited carbon was reflected in large quantities in the characterisation of the spent catalysts. Supporting the idea that RuO_2 is the active phase, an increased quantity of deposited carbon could have inhibited Ru oxidation to RuO_2 as the active species.

During the third phase, C_3 conversion stabilised at 32 ± 14%. The C_3 conversion of the blank run, at 15%, was around half that of the stable value of the CR runs. CO_x selectivity settled at 11 ± 9%, which was marginally higher than the blank run. Total hydrocarbon conversion stabilised at 9 ± 9%, which, while substantially higher than the blank run at ~2%, showed significant variability and was nearly completely deactivated towards the reforming reaction. It is possible that carbon deposition continued to occur over this final period, however, if most of the carbon deposition was occurring over this period, it would be anticipated that a relationship would be observed between total time-on-stream and the final measured mass loss in TGA, which was not the case. It is likely, therefore, that carbon deposition was occurring cumulatively over the second phase, leading to the observed deactivation.

Two experiments were performed with the reduction and steaming start-up procedure – CRS-1 and CRS-2. The dispersive effect of the reduction and steaming procedure was clearly

apparent in the data, since, contrasting with the CR runs, a two-stage pattern was observed in the data: a first phase of very high catalytic activity which reduced very quickly, and a second phase of stable performance. Though the first phase started at what was effectively the second phase for the CR runs, the peak catalytic performance in these runs was much higher, with both C_3 and total hydrocarbon conversion starting at 100% and declining rapidly over 10 – 20 h time-on-stream. The initial high conversion suggests that RuO_2 may be the active phase. The period of deactivation occurred more rapidly and completely, with C_3 conversion stabilising at 25 ± 2%, and total hydrocarbon conversion stabilising at 2.5 ± 2.5%. Contrasting C_3 conversion at 25 ± 2% against the blank run at 15%, there was more cracking occurring than purely due to thermal background effects. Contrasting the C_3 conversion against the CR runs at 32 ± 14%, the spread of data was lower, as was the final extent of the cracking reaction. The total hydrocarbon conversion, at 2.5 ± 2.5%, was effectively the same as the blank run, but lower than the CR runs at 9 ± 9%. The substantially increased initial conversion in comparison to the CR-runs may be explained by a change in particulate size and shape, as XRD indicated a reduced crystallite size, and TEM indicated a change in particle shape towards platelets, which would have resulted in a significantly more dispersed catalyst. Alternatively, the increased initial performance seems to support the idea that RuO_2 is the active phase. Analysis of the spent catalyst from the CRS runs via XRD showed that the Ru was reduced, indicating that some degree of structural change must have occurred over the initial experimental period, as the catalyst placed in the reactor was in oxide form. However, it is also possible that due to the large quantity of deposited carbon on the catalyst, RuO_2 which was present during the reaction may have been reduced during the cooling period after termination of the experiments. It is also possible that due to the smaller particle size of the CRS catalyst, complete encapsulation of the metal particles may have occurred, inhibiting the gasification of carbon which may otherwise have occurred on the interface between the carbon and the metal particles.

The results of the CR and CRS experiments served to suggest that the active phase in the reaction may be RuO_2 as opposed to Ru metal. The substantially higher initial performance and two stage pattern of the CRS runs, in which the catalyst was in RuO_2 form at the initiation of the dry feed, in contrast to the CR runs with a three-stage performance pattern, in which the catalyst was in Ru metal form, seemed to support this conclusion. Moreover, this would seem to be supported by the modest effect of the addition of the air co-feed in the reforming experiments.

The effect of air as a co-feed was tested in all but the first experiment. In CR-2, CR-3 and CR-4, air was added as a co-feed after the conversions had reached steady state. In CR-4, air as a co-feed was removed once the observed effects of the co-feed had stabilised, to determine if the effects were reversible (and partially to determine if they were real and not just an artifact). In CRS-1 and CRS-2, air was present as a co-feed from the start of the run, and the effects of removing the co-feed were observed.

Experiment CR-2 utilised the addition of an air co-feed at 1% of the dry feed composition after the experiment had reached pseudo-steady state. A limited and very small increase in C_3 conversion, total hydrocarbon conversion, and CO:CO_2 ratio was observed, though this may have been an experimental artifact. While the CO_x selectivity appeared to be decreasing, it appeared to stabilise following the addition of the co-feed. These factors indicated that there may be a small effect due to the addition of the 1% air co-feed.

Experiment CR-3 utilised the addition of an air co-feed at 1% of the dry feed composition after the experiment had reached pseudo-steady state. The obtained data were very highly scattered, hindering data analysis to a large degree. No clear pattern emerged in the C_3 or total hydrocarbon conversion following the addition of the 1% air co-feed. The CO_x selectivity appeared to increase from near 0% to a majority of data points lying in excess of 10%. Furthermore, the CO:CO_2 ratio appears to increase substantially, from 0.25 to 1.5, indicating the possibility of an effect on catalytic performance and deactivation.

Experiment CR-4 utilised a larger co-feed addition of air at 3% of the total dry feed composition. There was no clear increase in the C_3 conversion, however, there was a clear increase in the total hydrocarbon conversion, with data points clearly increasing from near-zero values to in the region of 1 – 10%. Most notable was a marked increase and stabilisation in the CO_x product selectivity – with an increase from 6% to 12%, clearly indicating an effect. There was also a clear increase in the CO:CO_2 ratio from 0.89 to 1.9, and a clearly observable upwards trend, suggesting that the carbon removal from the catalyst surface at this co-feed proportion may continue over time. That these changes were caused by the addition of the co-feed was supported by the fact that they were reversed immediately on removal of the co-feed.

Experiment CRS-1 was started with an air co-feed of 1% already running. Deactivation was pronounced in spite of the presence of the co-feed, indicating that the effect was not somehow more pronounced when run from 0 h time-on-stream. The co-feed was removed after the experiment had reached pseudo-steady state. No observable changes occurred in the C_3 conversion or the total hydrocarbon conversion. Nonetheless, there was a clear and immediate decrease in CO_x selectivity from ~11% to 3%, and a decrease in CO:CO_2 ratio from 2 to 0.9, indicating that the co-feed was mitigating deactivating to some degree.

Experiment CRS-2 was started with an air co-feed of 1%. There was a small observable decrease in C_3 conversion and total hydrocarbon conversion following the removal of the co-feed, and a decrease in CO_x selectivity from 3% to ~0%. Most notably, there was an immediate decrease in the CO:CO_2 ratio from 7% to 0.4%. These results are indicative of a small effect from the co-feed.

Through all of the experiments using an air-co feed, the effects most clearly associated with an air co-feed were a higher CO_x selectivity, and a higher CO:CO_2 ratio. Small increases in C_3 conversion and total hydrocarbon conversion were observed, though too small to ascertain with certainty. The effect was most pronounced in experiment CR-4, which utilised the largest co-

feed, indicating that the effect scales with the proportion of the co-feed, leaving room for further work at a higher co-feed proportion. This also suggested that RuO_2 may be the active phase, increased in proportion by the addition of the air co-feed.

The S/C ratio was altered intentionally in two experiments: CRS-1 reduced the S/C ratio from 4 to 3.5 and then to 3, while in CR-4, the S/C ratio was increased to 6. Due to some malfunctions affecting the water pump, variation was created in some of the other experiments, most notably CR-1.

Experiment CR-1 incurred a change in S/C ratio over time from 3.7 to 3 due to the malfunction of the water pump. Whereas it was expected that the decrease in S/C ratio would lead to a decline in catalytic performance, the C_3 conversion and total hydrocarbon conversion remained relatively unchanged throughout the duration of the decline, indicating a remarkable tolerance to decreased S/C ratio. Notwithstanding, following the correction of the water pump flowrate towards the end of the experiment, C_3 conversion and total hydrocarbon conversion remained relatively unchanged, however, there was a pronounced increase in CO_x selectivity.

Experiment CRS-1 implemented an S/C ratio change of 4 to 3.5 and then to 3. In both cases, the space velocity was made up with nitrogen. In the change from 4 to 3.5, there were no observable changes in C_3 conversion or total hydrocarbon conversion, indicating a remarkable invariance in activity with respect to S/C ratio. Limited changes were observed in the carbon product selectivities, but none were pronounced. The S/C ratio change from 3.5 to 3 was accompanied by a substantial increase in C_3 conversion and total hydrocarbon conversion, but this is thought to be an artifact due to several confounding factors.

Experiment CR-4 implemented an S/C ratio change from 4 to 6. There were no observed changes in C_3 or total hydrocarbon conversion, but some changes in carbon product selectivity were observed, with a small increase in CO_x selectivity. The results of the changes were indicative of a relative insensitivity of the process to increased S/C ratio.

Variation of the S/C ratio was found to have a very limited effect on the C_3 and total hydrocarbon conversions. In particular, similar catalytic activity and deactivation was observed when the S/C ratio was decreased. As such, S/C ratio was not found to be a primary determining factor in the rate of carbon deposition.

In all experiments, deactivation was observed to be pronounced, and the effects of the deactivation mitigation measures was limited. Characterisation of the spent catalyst was performed using XRD, TEM and TGA-DTG-DTA, as these were the means of characterisation which would effectively quantify and characterise the form of the deposited carbon. Results of the characterisation of the spent catalyst confirmed that substantial carbon deposition had occurred on all of the spent catalyst samples. It is likely that this carbon deposition occurred largely over the period of deactivation which was observed in the reactions. It is important to note that all of the experiments were terminated due to failing of the furnace, and that increased

carbon laydown may have occurred over this period. Nonetheless, while analyses of the spent catalyst indicated that only Ru metal was found, the abundance of carbon may have acted to reduce the RuO_2 back to Ru over the cooling period, and the experimental results indicated that it was likely that RuO_2 was the active phase in the steam-reforming reaction.

Thermogravimetric analyses in air indicated similar mass loss and heat flow curves for all of the samples, with a clear DTG peak in the region of 600°C, which is indicative of the removal of 'hard coke', i.e., graphitic carbon and carbon nanotubes. Most of the mass loss occurs at this temperature. The clearest example is seen in Figure A11.5, which shows a shoulder on the peak that is likely reflective of the removal of carbon from the support, which is more resistant to gasification than the carbon deposited close to or on the metal particles. Mass loss values from the thermogravimetric analyses are tabulated in Table 4.7. The average mass loss across all the spent catalyst samples was 29.7 ± 7.9%, while the average for the samples from the standard reduction procedure runs was 28.7 ± 9.3%, and the average for the samples from the reduction and steaming procedure was 31.9 ± 2.5%, indicating that there was not an observable difference in quantifiable carbon between the samples from the different procedures. Mass loss from the fresh calcined catalyst was 9.8% (see Figure 4.1), occurring at a much lower temperature, indicating a smaller proportion of physisorbed water, and further validating the extent of the carbon deposition.

X-ray diffraction analysis of the spent catalyst samples indicated that in all cases, the Ru contained in the catalyst remained reduced or metallic following the termination of the experiment, including the runs which were terminated with air running as a co-feed. Notwithstanding, this does not negate the possibility that RuO_2 may have been the active phase in the reaction, as the reduction may have occurred over the cooling down period, due to the presence of large quantities of carbon, as confirmed by TGA. The average crystallite size of the Ru particles from the spent catalysts was 54.5 ± 12.7 nm (compared to the reduced catalyst at 49.7 nm and the reduced and steamed catalyst at 29.3 nm). No clear relationship between time-on-stream and crystallite size was observed. The crystallite size remained effectively unaltered from the crystallite size of the fresh catalysts. Peaks for graphitic carbon were observed for all the spent catalyst samples, providing further support for the hypothesis that carbon deposition is the primary mechanism of deactivation.

TEM images showed further that substantial carbon deposition had occurred on all the spent catalyst samples. In all cases, graphic carbon was found to have encapsulated Ru particles, which indicates that the carbon contributed substantially to deactivation. Several images also indicated the presence of carbon nanotubes, which are known to contribute to separation of the metal from the support. The presence of such significant quantities of graphitic carbon effectively rendered the collection of particle size distributions for the spent catalyst samples infeasible, as it was not possible to clearly observe particle borders.

6. Conclusions and Recommendations

The aim this study was to investigate the effect of introducing a co-feed of air in propane steam reforming on Ru/Al_2O_3 and therewith to determine whether the extent of deactivation could be reduced. Steam reforming catalysts are prone to deactivation, and short product lifespans may hinder the development of fuel-processer technology. The study hypothesised that co-feeding air at low proportions relative to the total dry feed (1 – 3%) may be used to mitigate deactivation by availing free oxygen at the catalytic surface. The study further sought to investigate the effect of varying the S/C ratio of the feed, and also that of certain pre-reaction catalytic treatments.

Results from the series of propane steam reforming experiments showed different behaviour following the different pre-treatments of the catalyst. The Calcined/Reduced catalyst runs followed three phases of reaction performance: first, an increase in performance due to catalytic restructuring; second, a gradual decline in catalytic performance; and third, a stable performance in which reforming activity was essentially negligible. This contrasted with the Calcined/Reduced/Steamed catalyst runs, in which two stages were seen: a first stage with a rapid decline from near-complete conversion, leading to a second stage, with a lower stable conversion for the cracking and reforming reactions than what was observed in the Calcined/Reduced catalyst runs. All of the runs contrasted with the blank run, with cracking activity effectively twice that due to thermal background effects, and with reforming activity marginally higher than that due to thermal background effects, but effectively negligibly so. The initially higher performance of the Calcined/Reduced/Steamed catalyst indicated that RuO_2 may have been the active phase in the reforming reaction.

Results from the series of propane steam reforming experiments in which air was added/removed as a co-feed indicated that C_3 conversion and total hydrocarbon conversion were minimally affected, with very limited changes observed, however with an increased total hydrocarbon conversion, particularly in the experiment with the largest air co-feed addition. Notwithstanding, carbon product selectivity was affected favourably in all cases, with a clear increase in CO_x selectivity, and an increase in $CO:CO_2$ ratio. These effects were reversible on removal of the co-feed, indicating clearly that it was causing an effect. Most experiments were performed with air as a co-feed at 1% of the total dry feed composition, with only one experiment utilising a 3% level of co-feed addition. The effects were most noticable for this experiment, suggesting that a larger co-feed may yield a greater effect, and leaving room for further investigation. This also lends support to the idea that RuO_2 may be the active phase.

Several experiments varied the S/C ratio of the feed to the reactor and found very limited changes in performance, indicating that the S/C ratio was not a substantial controlling factor in the rate of carbon deposition. This leaves room for further investigation into the extent of the resilience of the catalyst to decreased S/C ratio, as it is desirable for the intended applications of the catalyst that it utilise less water.

Characterisation of the fresh catalysts indicated that a steaming procedure may reduce metal particle size, increase dispersion, change morphology, and oxidise the Ru back to RuO_2, explaining the significantly higher initial activity observed in these experiments. The more complete deactivation observed with the reduced/steamed catalysts may be explained by complete encapsulation of the smaller metal/metal oxide particles, which was consistent with the results of the spent catalyst characterisation. Further work may investigate this steaming dispersion effect, particularly to determine if the higher initial performance may be stabilised.

Characterisation of the spent catalysts indicated that significant carbon deposition had occurred in all cases. Thermogravimetric analysis indicated that carbon deposition accounted for ~30% of the mass of the spent catalyst samples, and the thermal peaks in the DTG and DTA curves indicated that the carbon deposition was in the form of 'hard coke', i.e., graphitic carbon and carbon nanotubes. TEM pictures of the spent catalyst samples confirmed the presence of graphitic carbon and carbon nanotubes. In particular, graphitic carbon was found to have fully encapsulated many metal particles in the samples, accounting for deactivation. XRD analysis of the spent catalyst samples indicated (non-quantitatively) the presence of graphitic carbon on all the spent catalyst samples. Though Ru was found in the metallic phase, this may be due to reduction occurring in during the cooling of the reactor after experiments and does not rule out the possibility of RuO_2 as the active phase. Moreover, since all of the experiments ended with a comparatively decreased temperature due to furnace failure, the lower temperature may have incurred a greater quantity of carbon deposition.

The reactor system which was used to perform this series of experiments experienced several issues that should be fixed before engaging in further work. In particular, the furnace which was used to heat the reactor tube experienced frequent and significant breakdowns in performance, attributable to the heater cartridges used to heat the furnace, which were not suited to operation at high temperatures for extended periods. Moreover, as lower temperatures are associated with more carbon deposition, the furnace system must be capable of operating at higher temperatures, particularly in excess of 800°C. The HPLC which was used to supply water to the reactor also experienced breakdowns on several occasions and using a water pump which is specified at a higher flowrate may be advisable. Furthermore, the use of a new argon mass flow controller or an entirely different internal standard may incur less faulty data sets.

The deactivation mitigating effect of the air co-feed was tested for co-feeds with a small oxygen-to-carbon ratio. Since the effect was found to be greatest where there was a larger co-feed content, further investigations should investigate larger co-feeds, as the effect may become more pronounced – perhaps even to a level of sustainable deactivation mitigation. Further work should also include investigating the dispersive effects of the reduction and steaming procedure, as it may be possible to stabilise the higher initial activity. Finally, further work should seek to investigate the active phase of the catalyst, possibly through a technique such as in-situ XRD, as results indicated that RuO_2 may likely be the active phase.

References

1. Barbir, F., *PEM Fuel Cells: Theory and Practice*. 2nd ed. 2012: Elsevier.
2. Kaur, G., ed. *PEM Fuel Cells: Fundamentals, Advanced Technologies, and Practical Application*. 2021, Candice Janco.
3. Stone, R., *Introduction to Internal Combustion Engines*. 2012: Palgrave Macmillan 516.
4. Heywood, J., *Internal Combustion Engine Fundementals*. 2018: McGraw-Hill Education.
5. Leach, F., *et al.*, *The scope for improving the efficiency and environmental impact of internal combustion engines.* Transportation Engineering, 2020. **1**.
6. Schüth, F., *Challenges in hydrogen storage.* The European Physical Journal Special Topics, 2009. **176**(1): p. 155-166.
7. Murkin, C. and J. Brightling, *Eighty Years of Steam Reforming.* Johnson Matthey Technology Review, 2016. **60**(4): p. 263-269.
8. Carrette, L., K.A. Friedrich, and U. Stimming, *Fuel Cells: Principles, Types, Fuels and Applications.* ChemPhysChem, 2000. **2000**: p. 162-193.
9. US Department of Energy - Office of Energy Efficiency and Renewable Energy. *Types of fuel cells*. [cited 2019 17th April]; Describes the different types of fuel cells and gives a description of their mechanism]. Available from: https://www.energy.gov/eere/fuelcells/types-fuel-cells.
10. Ghenciu, A.F., *Review of fuel processing catalysts for hydrogen production in PEM fuel cell systems.* Current Opinion in Solid State & Materials Science, 2002. **6**: p. 389-399.
11. Rostrup-Nielsen, J.R., *Production of synthesis gas.* Catalysis Today, 1993. **18**: p. 305-324.
12. Sperle, T., *et al.*, *Pre-reforming of natural gas on a Ni catalyst: Criteria for carbon free operation.* Applied Catalysis A: General, 2005. **282**(1-2): p. 195-204.
13. Gottesfeld, S. and T.A. Zawodzinski, *Polymer Electrolyte Fuel Cells*, in *Advances in Electrochemical Science and Engineering*, R.C. Alkire, *et al.*, Editors. 1997, Wiley-VCH Verlag GmbH. p. 197-297.
14. Edwards, N., *et al.*, *On-board hydrogen generation for transport applications the HotSpot™ methanol processor* Journal of Power Sources, 1998. **71**: p. 123-128.
15. Keulen, A.N.J.V. and J.G. Reinkingh, *Hydrogen Purification*, U.S.P. Office, Editor. 2002, Johnson Matthey Public Limited

Company: United States of America. p. 14.

16. Ashraf, M.A., *et al.*, *Final step for CO syngas clean-up: Comparison between CO-PROX and CO-SMET processes.* International Journal of Hydrogen Energy, 2014. **39**(31): p. 18109-18119.
17. Castaldi, M.J., *Removal of Trace Contaminants from Fuel Processing Reformate: Preferential Oxidation*, in *Hydrogen and Syngas Production and Purification Technologies*, K. Liu, C. Song, and V. Subramani, Editors. 2010, American Institute of Chemical Engineers.
18. Mills, G.A. and F.W. Steffgen, *Catalytic Methanation.* Catalysis Reviews, 1974. **8**(1): p. 159-210.
19. Rönsch, S., *et al.*, *Review on methanation – From fundamentals to current projects.* Fuel, 2016. **166**: p. 276-296.
20. Fox, J.M., *The Different Catalytic Routes for Methane Valorization: An Assessment of Processes for Liquid Fuels.* Catalysis Reviews, 1993. **35**(2): p. 169-212.
21. Whang, H.S., *et al.*, *Enhanced activity and durability of Ru catalyst dispersed on zirconia for dry reforming of methane.* Catalysis Today, 2017. **293-294**: p. 122-128.
22. Ayabe, S., *et al.*, *Catalytic autothermal reforming of methane and propane over supported metal catalysts.* Applied Catalysis A: General, 2002. **241**: p. 261-269.
23. Kumar, N., M. Shojaee, and J.J. Spivey, *Catalytic bi-reforming of methane: from greenhouse gases to syngas.* Current Opinion in Chemical Engineering, 2015. **9**: p. 8-15.
24. Stroud, T., *et al.*, *Chemical CO_2 recycling via dry and bi reforming of methane using Ni-Sn/Al_2O_3 and Ni-Sn/CeO_2-Al_2O_3 catalysts.* Applied Catalysis B: Environmental, 2018. **224**: p. 125-135.
25. Song, C. and W. Pan, *Tri-reforming of methane: a novel concept for catalytic production of industrially useful synthesis gas with desired H2/CO ratios.* Catalysis Today, 2004. **98**(4): p. 463-484.
26. Izquierdo, U., *et al.*, *Tri-reforming: A new biogas process for synthesis gas and hydrogen production.* International Journal of Hydrogen Energy, 2013. **38**(18): p. 7623-7631.
27. Subramani, V., *et al.*, *Catalytic Steam Reforming Technology for the Production of Hydrogen and Syngas*, in *Hydrogen and Syngas Production and Purification Technologies*, K. Liu, C. Song, and V. Subramani, Editors. 2010, John Wiley & Sons, Inc.: Hoboken, New Jersey. p. 32-112.

28. Grasso, G., *et al.*, *Methane Steam Reforming in Microchannel Reactors: Technical Challenges and Performances Benefits.* Topics in Catalysis, 2011. **54**(13-15): p. 859-865.
29. Joensen, F. and J.R. Rostrup-Nielsen, *Conversion of hydrocarbons and alcohols for fuel cells.* Journal of Power Sources, 2002. **105**: p. 195-201.
30. Chorkendorff, I. and J.W. Niemantsverdriet, *Concepts of Modern Catalysis and Kinetics*. 1 ed. 2003, Weinheim: John Wiley & Sons.
31. Avcı, A., *et al.*, *Hydrogen production by steam reforming of n-butane over supported Ni and Pt-Ni catalysts.* Applied Catalysis A: General, 2004. **258**(2): p. 235-240.
32. Kolb, G., *Review: Microstructured reactors for distributed and renewable production of fuels and electrical energy.* Chemical Engineering and Processing: Process Intensification, 2013. **65**: p. 1-44.
33. Cheekatamarla, P.K. and C.M. Finnerty, *Reforming catalysts for hydrogen generation in fuel cell applications.* Journal of Power Sources, 2006. **160**(1): p. 490-499.
34. Trimm, D.L. and Z.I. Önsan, *Onboard Fuel Conversion for Hydrogen-Fuel-Cell-Driven Vehicles.* Catalysis Reviews, 2001. **43**(1-2): p. 31-84.
35. Italiano, C., *et al.*, *High specific surface area supports for highly active Rh catalysts: Syngas production from methane at high space velocity.* International Journal of Hydrogen Energy, 2018. **43**(26): p. 11755-11765.
36. Mei, D., *et al.*, *Highly active and stable $MgAl_2O_4$-supported Rh and Ir catalysts for methane steam reforming: A combined experimental and theoretical study.* Journal of Catalysis, 2014. **316**: p. 11-23.
37. Ashraf, M.A., *et al.*, *Analysis of Ru/La-Al_2O_3 catalyst loading on alumina monoliths and controlling regimes in methane steam reforming.* Chemical Engineering Journal, 2018. **334**: p. 1792-1807.
38. Koo, K.Y., *et al.*, *Ru-coated metal monolith catalyst prepared by novel coating method for hydrogen production via natural gas steam reforming.* Catalysis Today, 2017. **293-294**: p. 129-135.
39. Vita, A., *et al.*, *Methane oxy-steam reforming reaction: Performances of Ru/γ-Al_2O_3 catalysts loaded on structured cordierite monoliths.* International Journal of Hydrogen Energy, 2014. **39**(32): p. 18592-18603.
40. Vita, A., *et al.*, *Syngas production by steam and oxy-steam reforming of biogas on monolith-supported CeO_2 -based catalysts.* International Journal of Hydrogen Energy, 2018. **43**(26): p. 11731-11744.

41. Menad, S., *et al.*, *Designing new high oxygen mobility supports to improve the stability of Ru catalysts under dry reforming of methane.* Catalysis Letters, 2003. **89**(1-2): p. 63-67.
42. Miyamoto, M., *et al.*, *Influence of metal cation doping on Ru/CeO_2/Al_2O_3 catalyst for steam reforming of desulfurized kerosene.* International Journal of Hydrogen Energy, 2015. **40**: p. 2657-2662.
43. van Niekerk, W., *Investigation into the behaviour of a wash-coated PGM-based catalyst layer in micro-channel reactors for the steam reforming of methane.*, in *Department of Chemical Engineering* 2017, University of Cape Town: Cape Town. p. 114.
44. Argyle, M. and C. Bartholomew, *Heterogeneous Catalyst Deactivation and Regeneration: A Review.* Catalysts, 2015. **5**(1): p. 145-269.
45. Bartholomew, C.H., *Carbon Deposition in Steam Reforming and Methanation.* Catalysis Reviews, 1982. **24**(1): p. 67-112.
46. Rostrup-Nielsen, J.R., *Coking on Nickel Catalysts for Steam Reforming of Hydrocarbons.* Journal of Catalysis 1974. **33**: p. 184-201.
47. Figueiredo, J.L.C.D.C., *Carbon formation on steam reforming catalysts* in *Faculty of Engineering* 1974, University of London.
48. Figueiredo, J.L., *Carbon Formation and Gasification on Nickel*, in *Progress in Catalyst Deactivation*. 1982, Springer, Dordrecht: NATO Advanced Study Institutes Series (Series E: Applied Sciences).
49. Forzatti, P. and L. Lietti, *Catalyst Deactivation.* Catalysis Today, 1999. **52**: p. 165-181.
50. Menon, P.G., *Coke on catalysts - harmful, harmless, invisible and benefical types.* Journal of Molecular Catalysis 1990. **59**: p. 207-220.
51. Wei, J. and E. Iglesia, *Isotopic and kinetic assessment of the mechanism of reactions of CH_4 with CO_2 or H_2O to form synthesis gas and carbon on nickel catalysts.* Journal of Catalysis, 2004. **224**(2): p. 370-383.
52. Vita, A., *et al.*, *Syngas production by methane oxy-steam reforming on Me/CeO_2 (Me = Rh, Pt, Ni) catalyst lined on cordierite monoliths.* Applied Catalysis B: Environmental, 2015. **162**: p. 551-563.
53. Karatzas, X., *et al.*, *Autothermal reforming of low-sulfur diesel over bimetallic RhPt supported on Al_2O_3, CeO_2–ZrO_2, SiO_2 and TiO_2.* Applied Catalysis B: Environmental, 2011. **106**(3-4): p. 476-487.
54. Agilent, *490 Micro GC User Manual*. 2017.

55. Wang, B. and G. Manos, *A novel thermogravimetric method for coke precursor characterisation.* Journal of Catalysis, 2007. **250**(1): p. 121-127.
56. Scherrer, P., *Determination of the internal structure and size of colloidal particles by means of X-rays*, in *Colloid Chemistry: A textbook*. 1912, Springer: Heidelberg, Berlin. p. 387-409.
57. Suoranta, T., M. Niemela, and P. Peramaki, *Comparison of digestion methods for the determination of ruthenium in catalyst materials.* Talanta, 2014. **119**: p. 425-9.
58. Newkirk, A.E. and D.W. McKee, *Thermal Decomposition of Rhodium, Iridium and Ruthenium Chlorides.* Journal of Catalysis 1968. **11**: p. 370-377.
59. Mazzieri, V., *XPS, FTIR and TPR characterization of Ru/Al_2O_3 catalysts.* Applied Surface Science, 2003. **210**(3-4): p. 222-230.
60. Koopman, P.G.J., A.P.G. Kieboom, and H.v. Bekkum, *Characterization of Ruthenium Catalysts as Studied by Temperature Programmed Reduction.* Journal of Catalysis, 1980. **69**: p. 172-179.
61. Trimm, D.L. *Thermal Stability of Catalyst Supports*. in *Catalyst Deactivation*. 1996. Elsevier Science Publishers B.V. Amsterdam.
62. Mieth, J.A. and J.A. Schwartz, *Effects of Alumina Dissolution and Metal Ion Buffering on the Dispersion of Alumina Supported Nickel and Ruthenium Catalysts.* Applied Catalysis 1989. **55**: p. 137-149.
63. Martin, N., *et al.*, *Coke Characterization on Pt/Al_2O_3 Zeolite Reforming Catalysts.* Industrial Engineering Chemistry Research, 2004. **43**: p. 1206-1210.

7. Appendix I: MFC Calibration Data

7.1. Nitrogen MFC Calibration

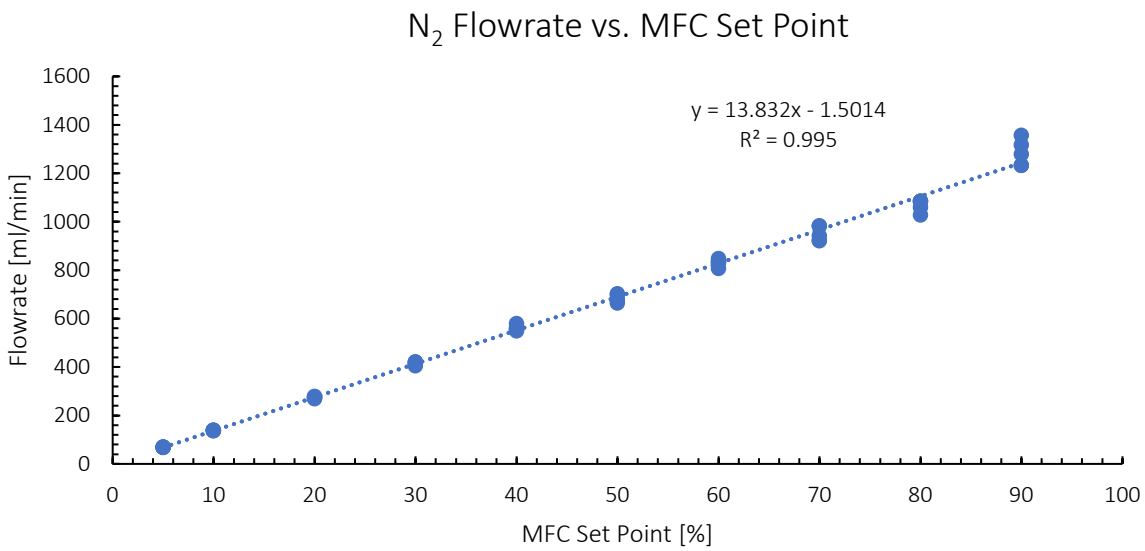

Figure A7.1: Nitrogen Mass Flow Calibration Curve

7.2. Argon MFC Calibration

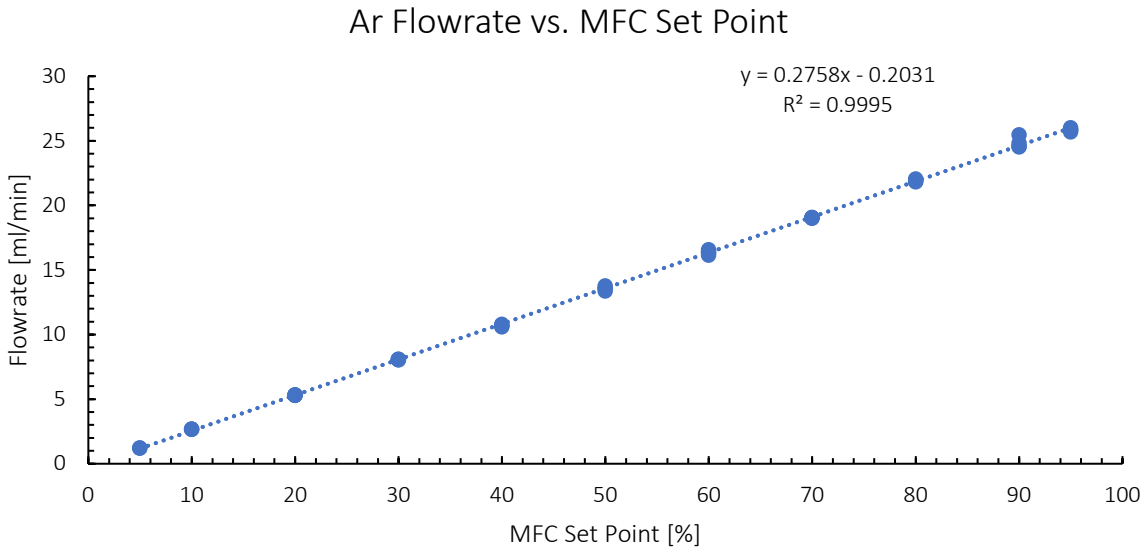

Figure A7.2: Argon Mass Flow Controller Calibration Curve

7.3. Hydrogen MFC Calibration

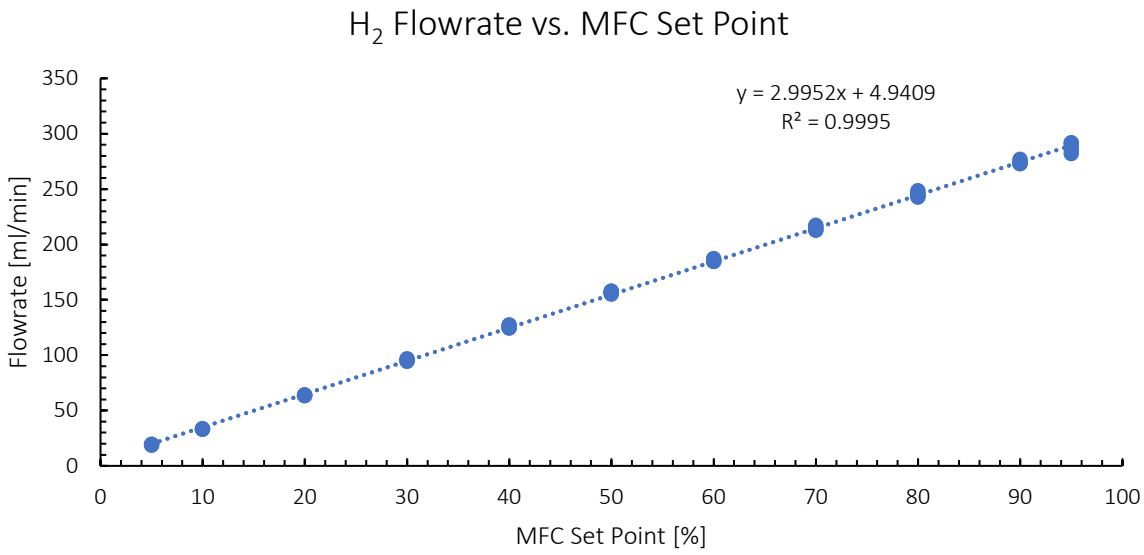

Figure A7.3: Hydrogen Mass Flow Controller Calibration Curve

7.4. Reactor MFC Calibration

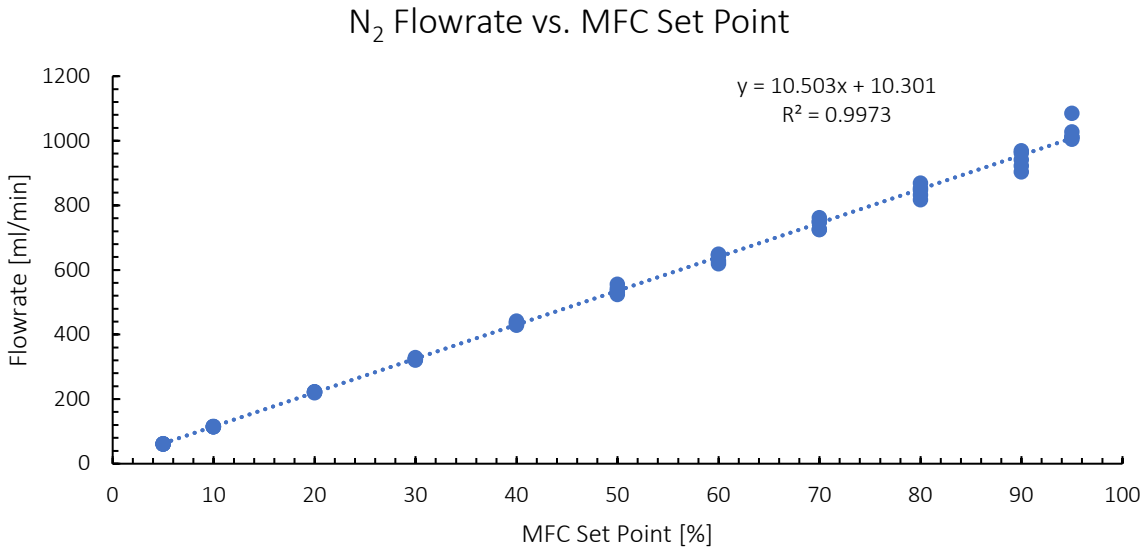

Figure A7.4: Nitrogen Mass Flow Controller Calibration Curve

7.5. Propane MFC Calibration

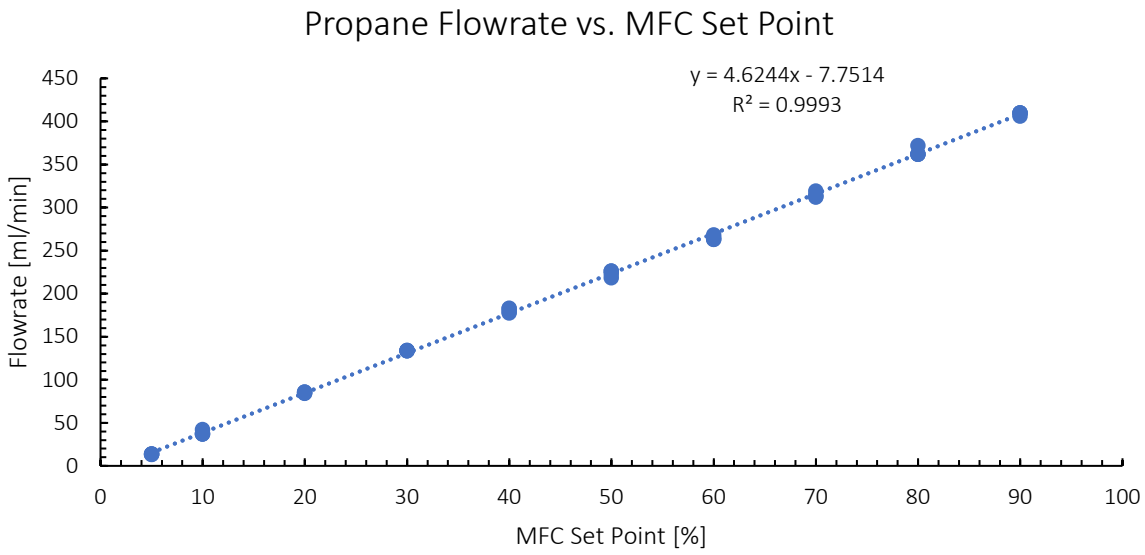

Figure A7.5: Propane Mass Flow Controller Calibration Curve

7.6. Carbon Monoxide MFC Calibration

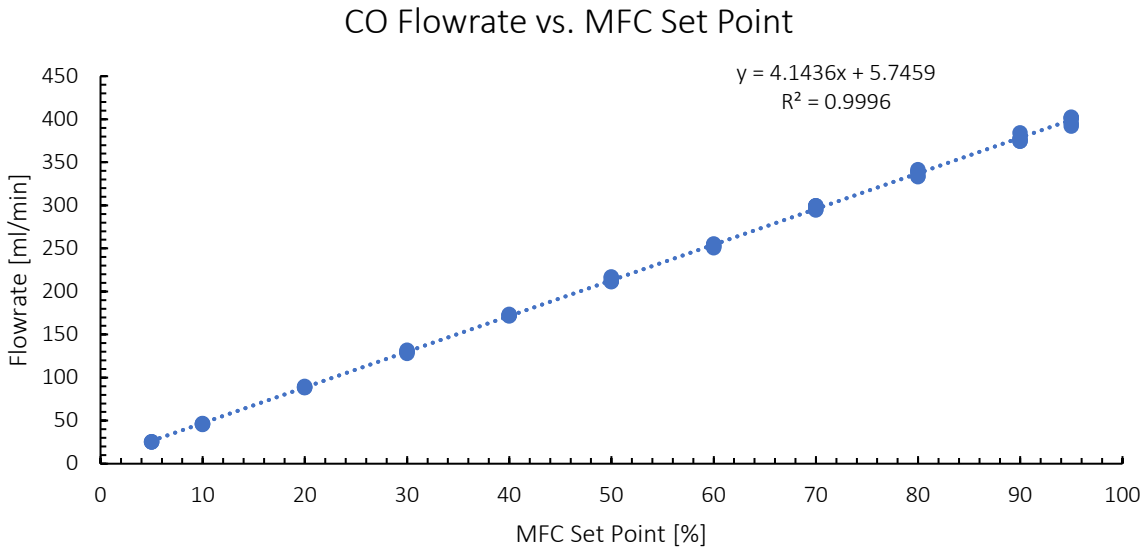

Figure A7.6: Carbon Monoxide Mass Flow Controller Calibration Curve

7.7. Methane MFC Calibration

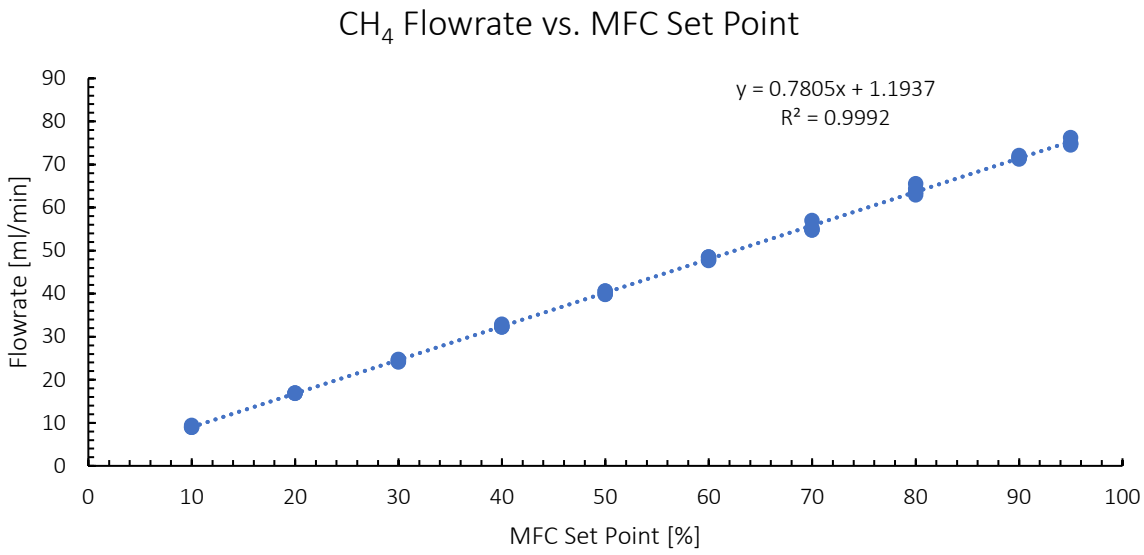

Figure A7.7: Methane Mass Flow Controller Calibration Curve

7.8. Carbon Dioxide MFC Calibration

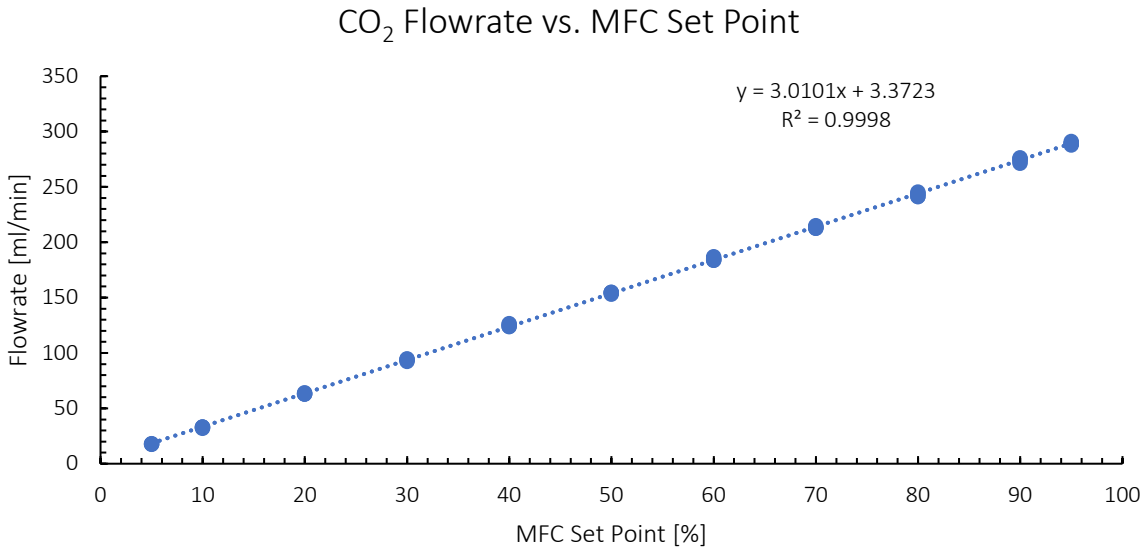

Figure A7.8: Carbon Dioxide Mass Flow Controller Calibration Curve

7.9. Air MFC Calibration

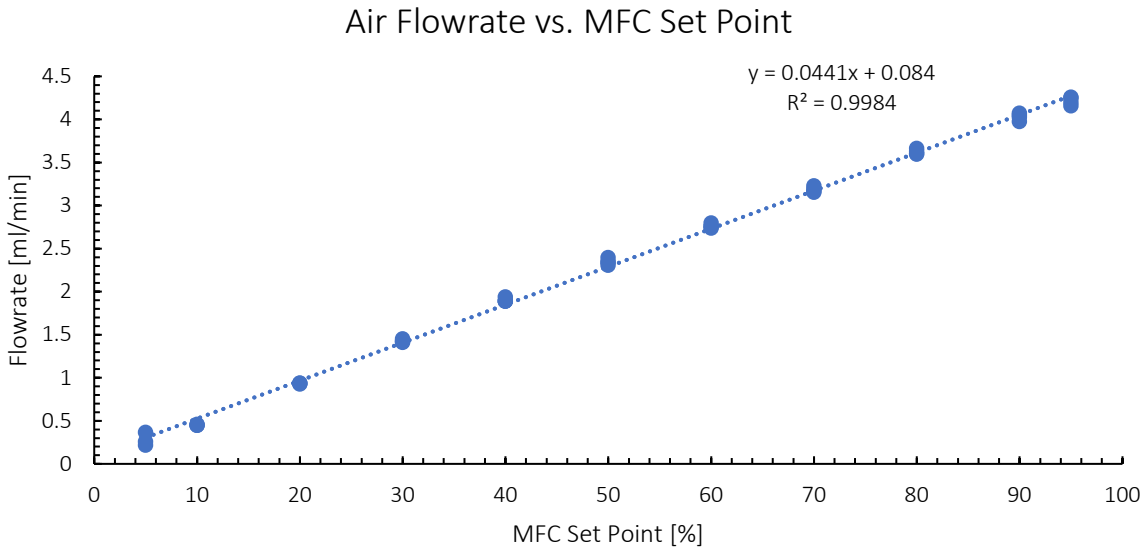

Figure A7.9: Air Mass Flow Controller Calibration Curve

7.10. Pump Calibration

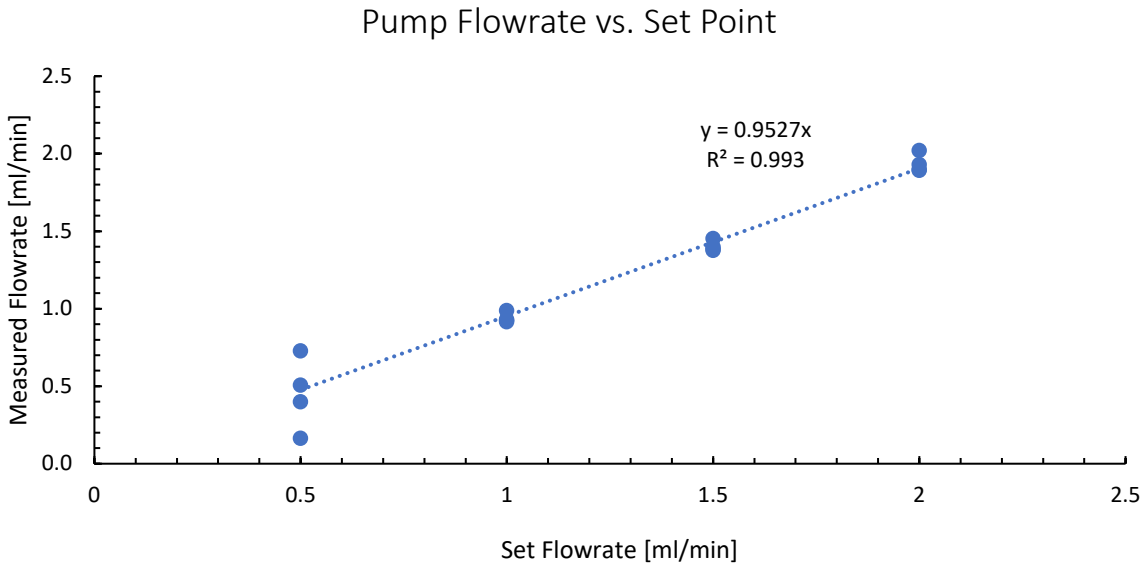

Figure A7.10: HPLC Pump Calibration Curve

8. Appendix II: Relative Response Factor Calibration Data

8.1. Relative Response Factor Calibration Data on Channel 1

8.1.1. Hydrogen Relative Response Factor on Channel 1

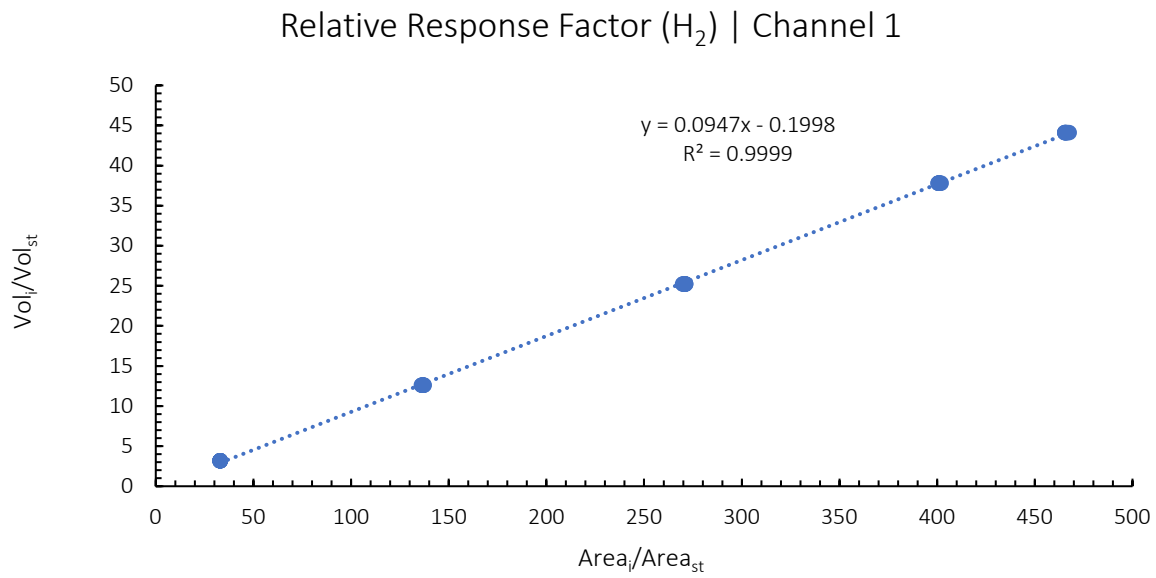

Figure A8.1: Hydrogen Relative Response Factor Calibration Curve on Channel 1

8.1.2. Methane Relative Response Factor on Channel 1

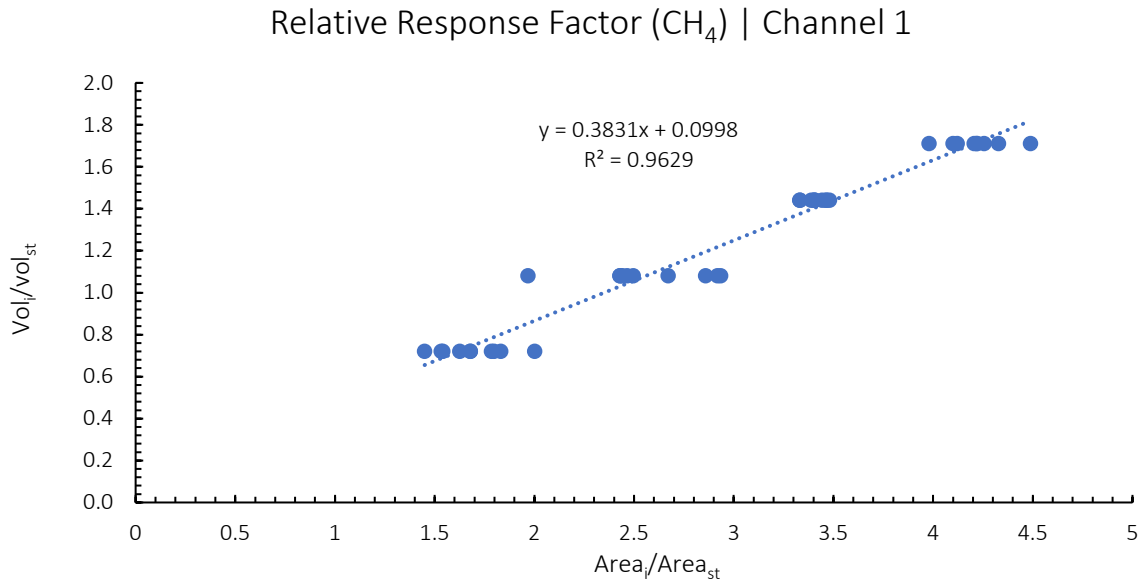

Figure A8.2: Methane Relative Response Factor Calibration Curve on Channel 1

8.1.3. Carbon Monoxide Relative Response Factor on Channel 1

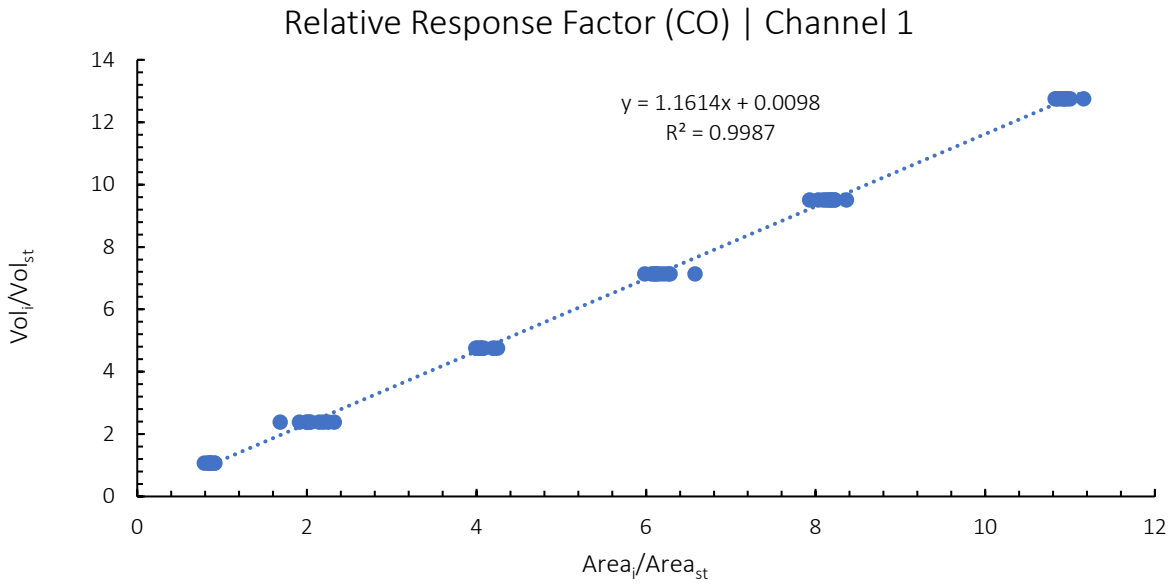

Figure A8.3: Carbon Monoxide Relative Response Factor Calibration Curve on Channel 1

8.1.4. Nitrogen Relative Response Factor on Channel 1

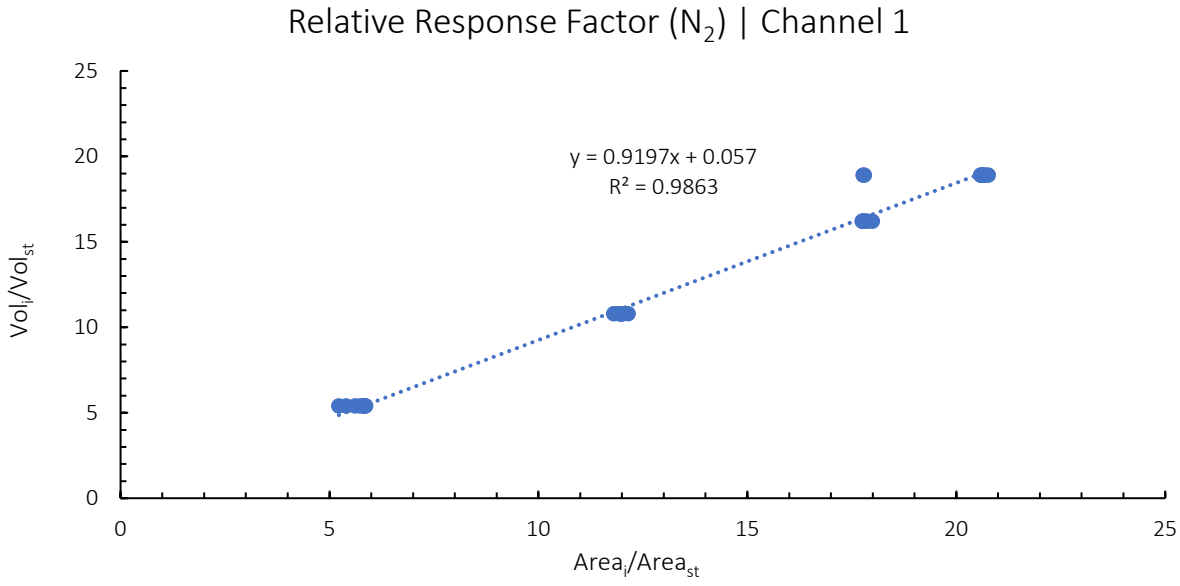

Figure A8.4: Nitrogen Relative Response Factor Calibration Curve on Channel 1

8.2. Relative Response Factor Calibration Data on Channel 2

8.2.1. Nitrogen Relative Response Factor on Channel 2

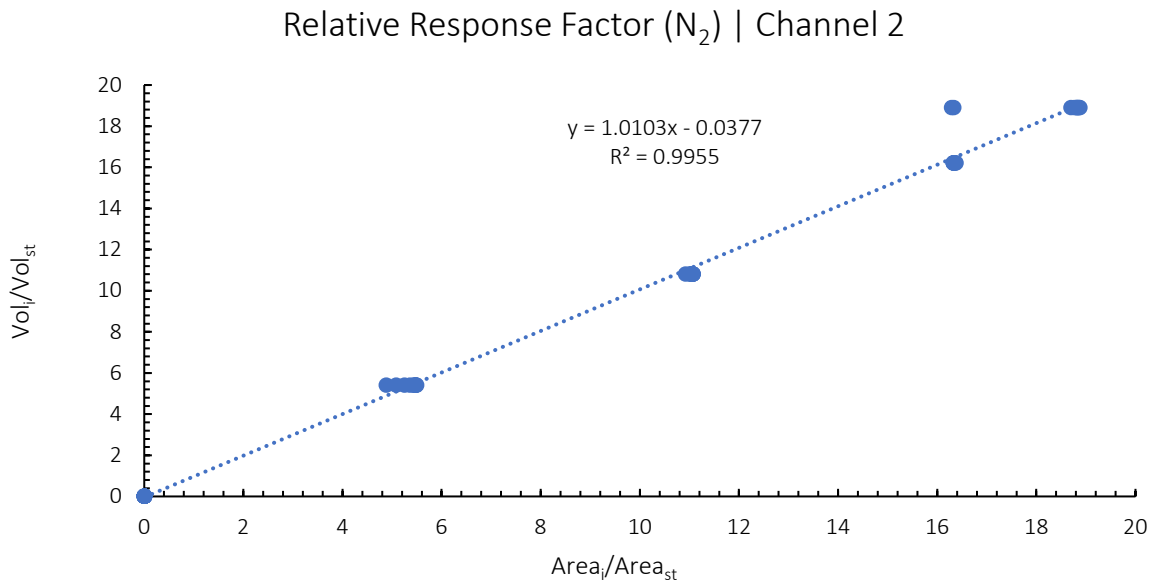

Figure A8.5: Nitrogen Relative Response Factor Calibration Curve on Channel 2

8.2.2. Carbon Monoxide Relative Response Factor on Channel 2

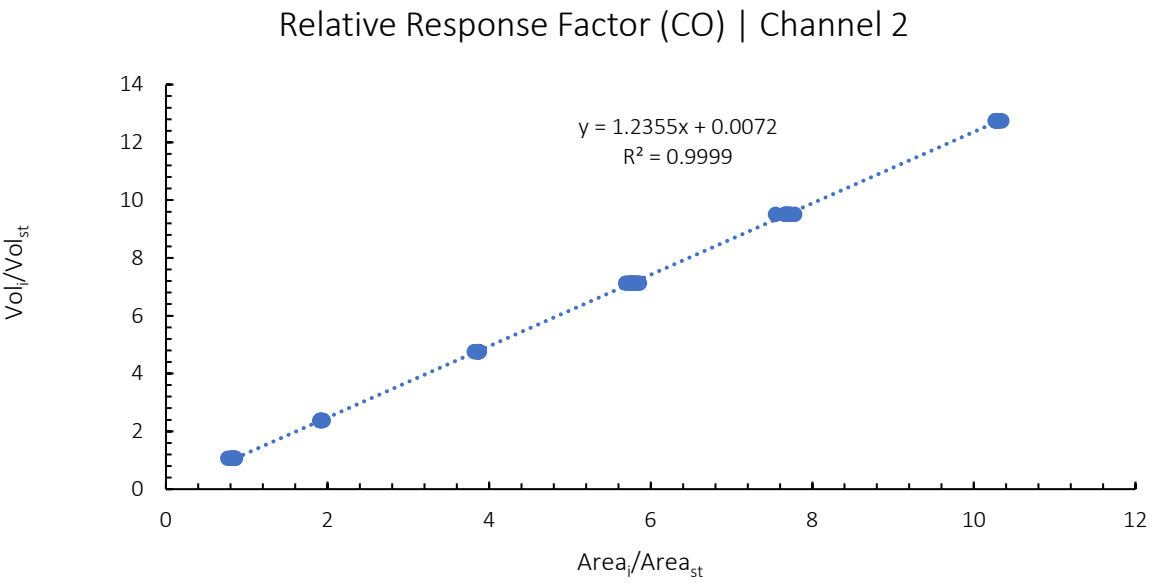

Figure A8.6: Carbon Monoxide Relative Response Factor Calibration Curve on Channel 2

8.2.3. Methane Relative Response Factor on Channel 2

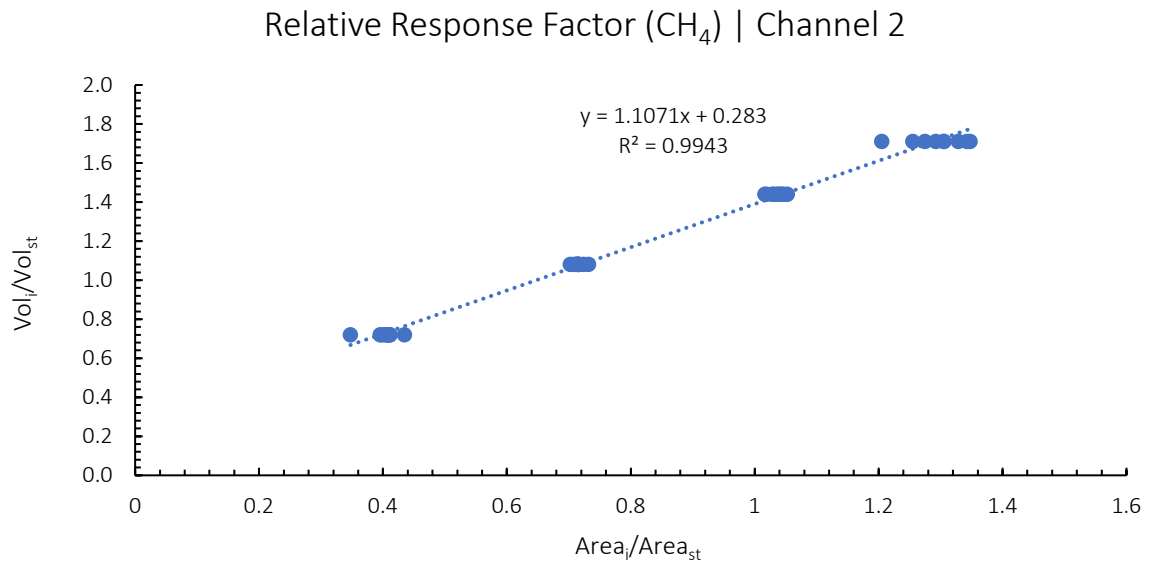

Figure A8.7: Methane Relative Response Factor Calibration Curve on Channel 2

8.3. Relative Response Factor Calibration Data on Channel 3

8.3.1. Propane Relative Response Factor on Channel 3

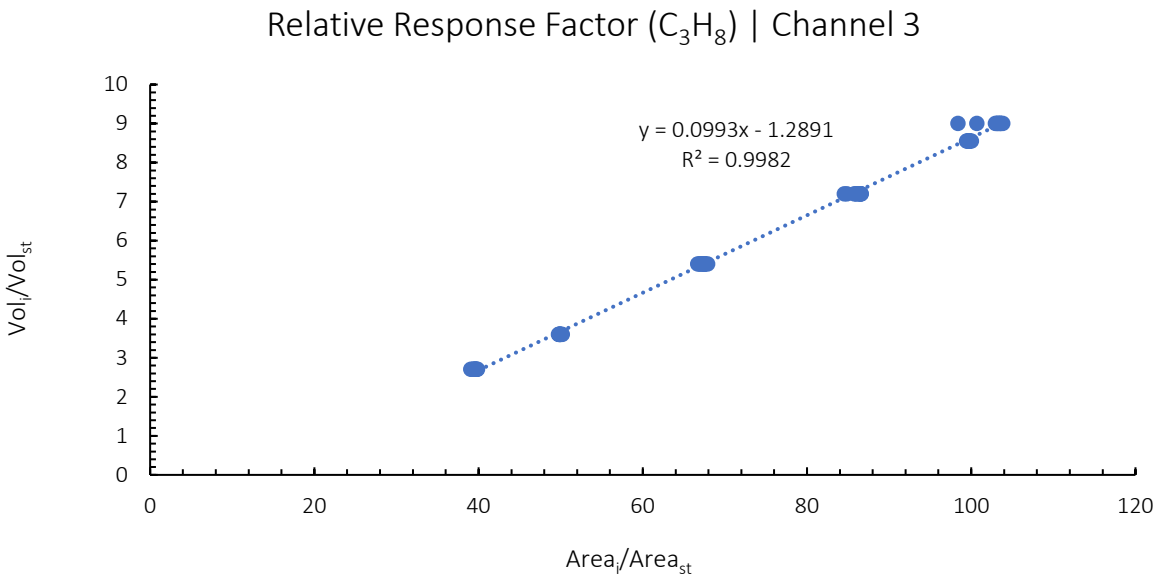

Figure A8.8: Propane Relative Response Factor Calibration Curve on Channel 3

8.3.2. Carbon Dioxide Relative Response Factor on Channel 3

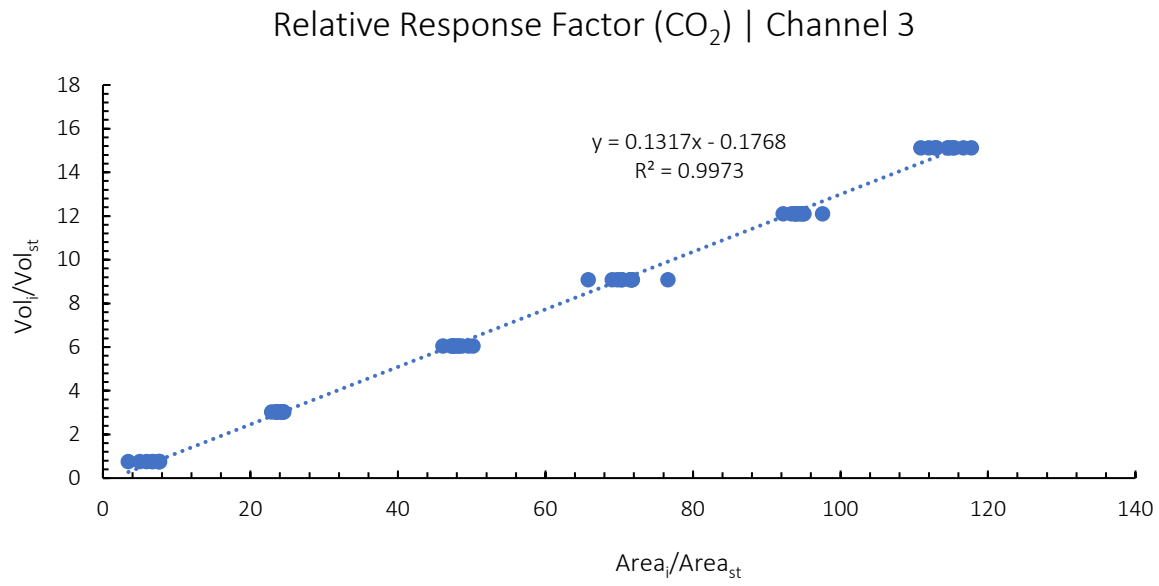

Figure A8.9: Carbon Dioxide Relative Response Factor Calibration Curve on Channel 3

8.3.3. Methane Relative Response Factor on Channel 3

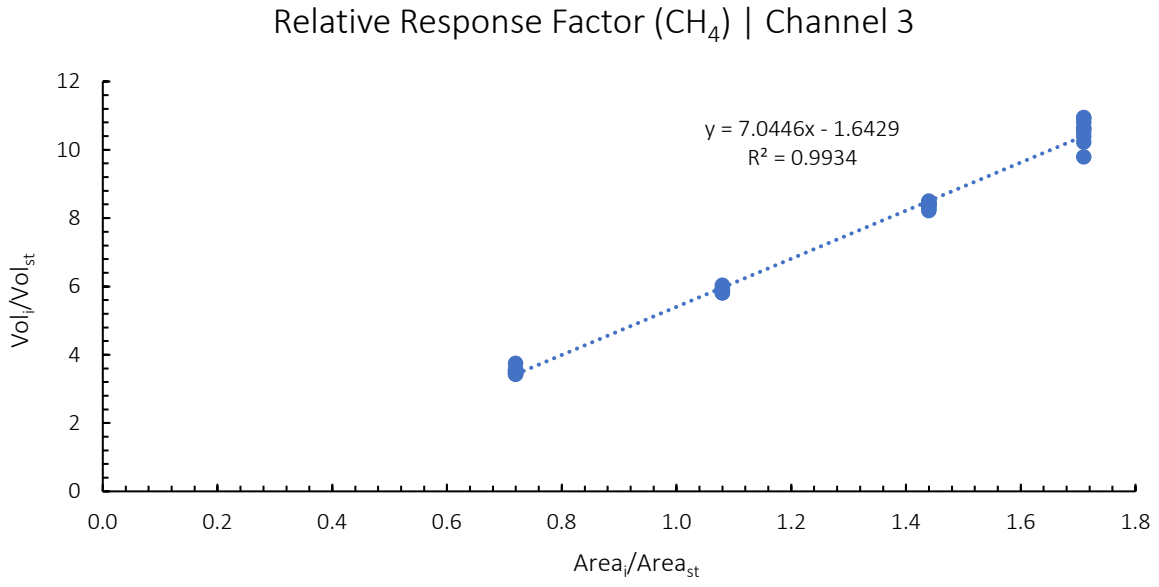

Figure A8.10: Methane Relative Response Factor Calibration Curve on Channel 3

8.3.4. Ethene Relative Response Factor on Channel 3

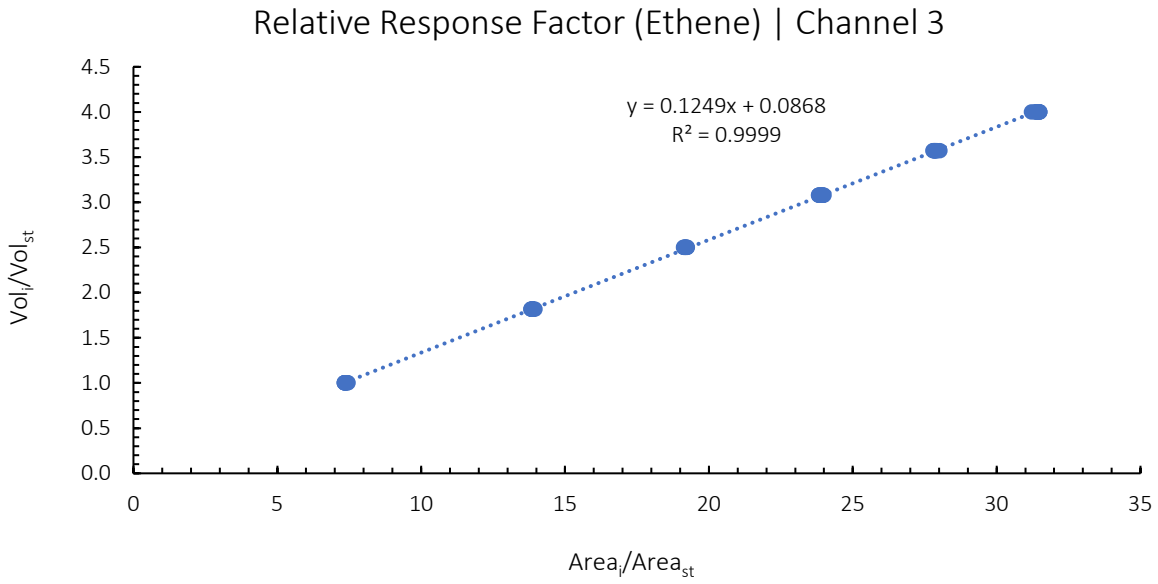

Figure A8.11: Ethene Relative Response Factor Calibration Curve on Channel 3

8.3.5. Ethane Relative Response Factor on Channel 3

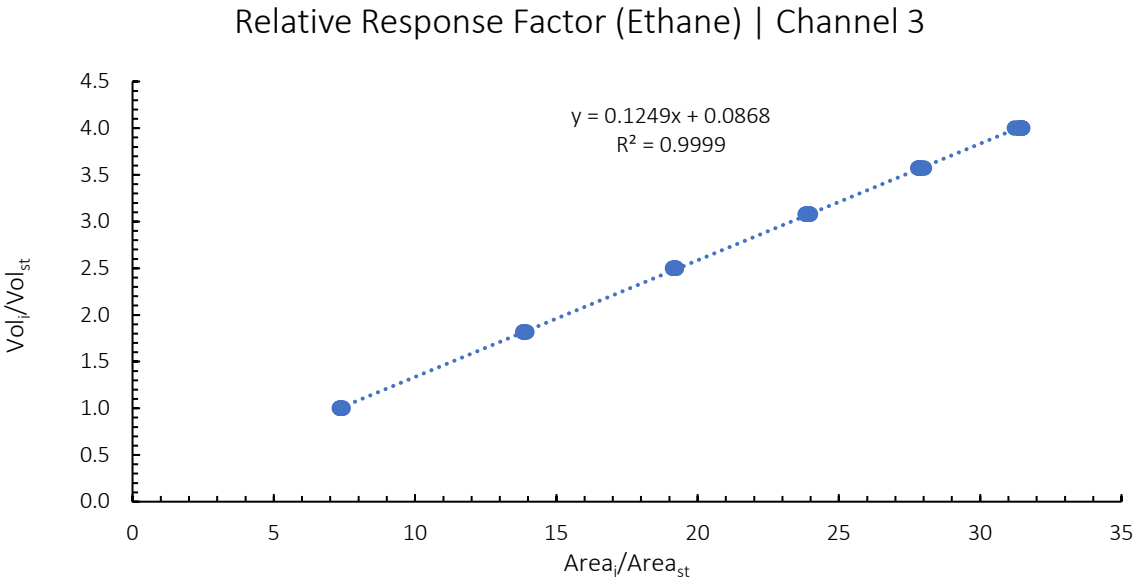

Figure A8.12: Ethane Relative Response Factor Calibration Curve on Channel 3

9. Appendix II – Backflush Calibration

The backflush calibration was performed in two stages. In the molsieve columns, the last eluting compounds are CH_4 and CO, so these compounds of interest are analysed to evaluate what point the backflush setting should be initiated. If the backflush time is set too early, the peaks of interest are partially or totally backwashed.

The calibration was performed in two stages. In the first stage backflush times were tested to evaluate where the peaks of interest would be totally backwashed. In the second stage, the backflush time was fine-tuned by examining a narrower range around the time found in stage 1, to determine where the peaks of interest would be fully eluted from the pre-column.

9.1. Initial approximate backflush calibration

9.1.1. Channel 1

The calibration examined backflush times from 0 to 10 seconds in 0.5 second increments.

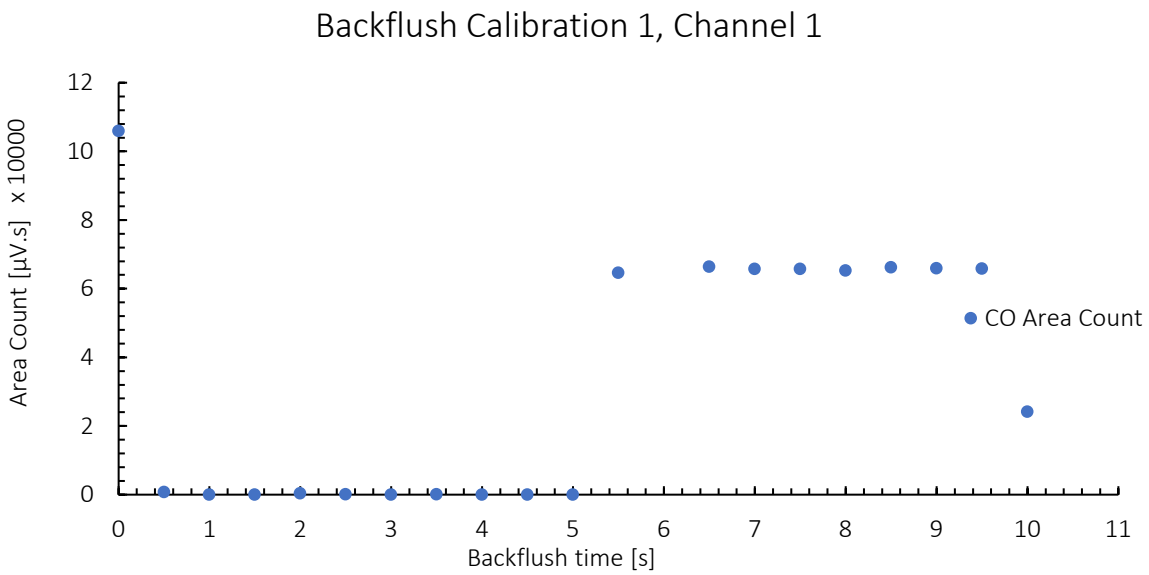

Figure A9.1: Area count for compounds of interest for initial channel 1 backflush calibration

It was determined that below a backflush time setting of 5.5 seconds, the desired compounds started to be removed by the backflush.

9.1.2. Channel 2

The initial approximate calibration examined backflush settings from 0 to 10 seconds in 0.5 second increments to determine the approximate backflush time setting where desired compounds for analysis would not be removed by the backflush.

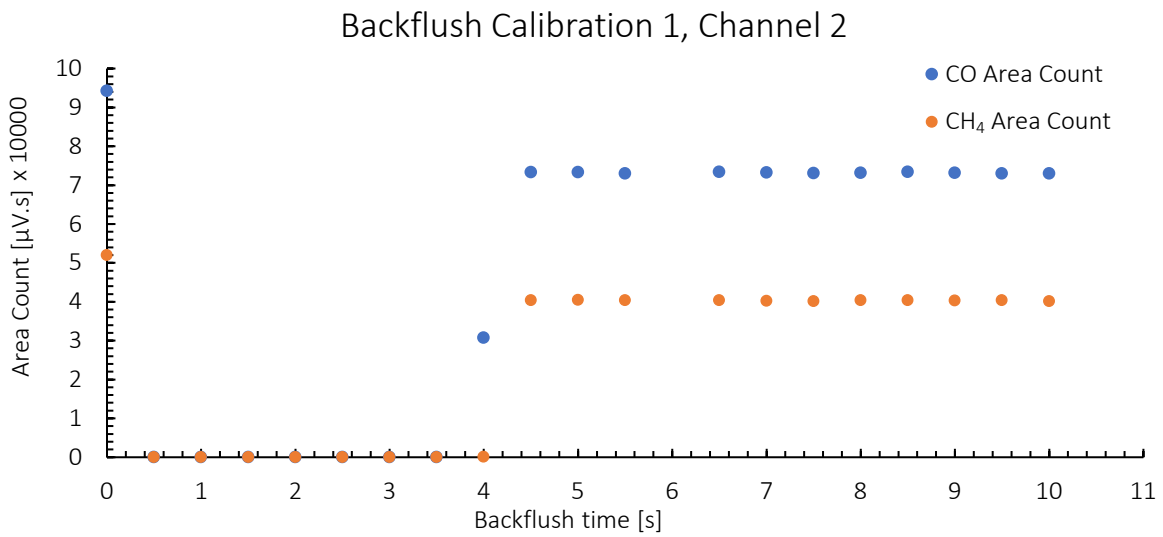

Figure A9.2: Area count for compounds of interest for initial channel 2 backflush calibration

It was determined that at a backflush time setting of approximately 4.5 seconds, the compounds desired for analysis were removed.

9.2. Fine tuning backflush calibration

9.2.1. Channel 1

The fine-tuning calibration for channel 1 examined backflush settings from 5.5 to 7.5 seconds in 0.1 second increments. At backflush settings which are too low, the compounds of interest will only partially be able to elute from the pre-column.

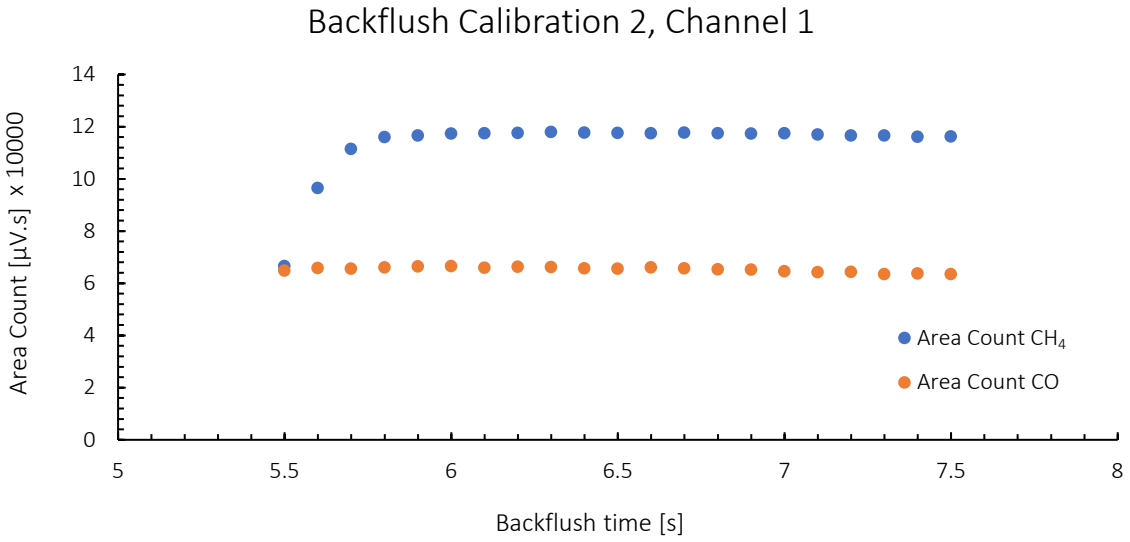

Figure A9.3: Area count for compounds of interest for fine tuning channel 1 backflush calibration

It was determined that at a backflush time setting of 6.1 seconds, all the desired compounds of interest would fully elute from the pre-column.

9.2.2. Channel 2

The fine-tuning calibration for channel 2 examined backflush settings from 4 to 6 seconds in 0.1 second increments.

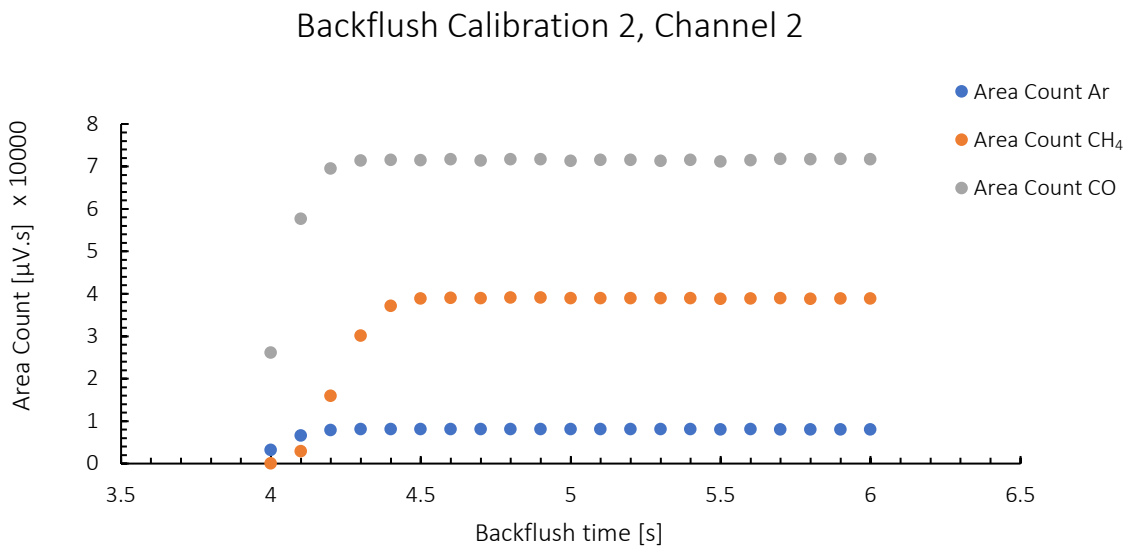

Figure A9.4: Area count for compounds of interest for fine tuning channel 2 backflush calibration

It was determined that at a backflush time setting of 4.6 seconds, all the desired components would elute fully from the pre-column.

10. Appendix III – Additional experimental data

10.1. Blank Run

All collected experimental data was reported for this experiment.

10.2. CR-1

All collected experimental data was reported for this experiment.

10.3. CR-2

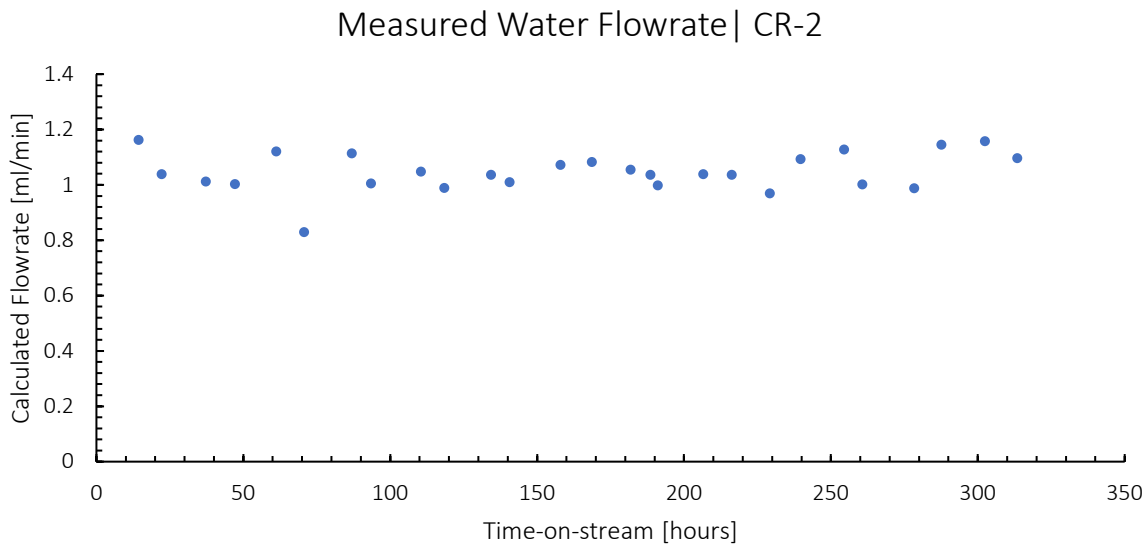

Figure A10.1: Measured water flowrate for Experiment CR-2

10.4. CR-3

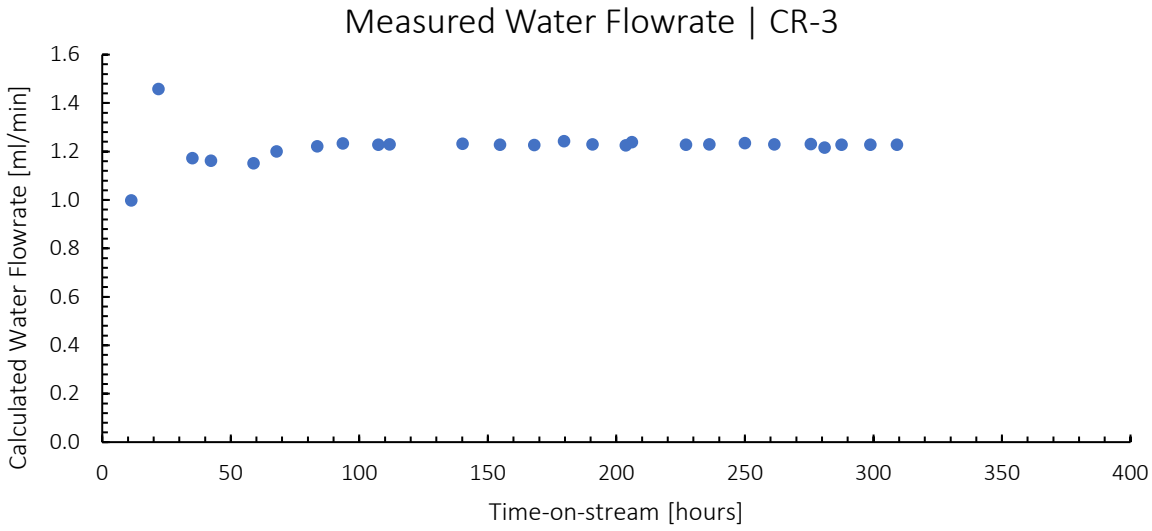

Figure A10.2: Measured water flowrate for Experiment CR-3

10.5. CR-4

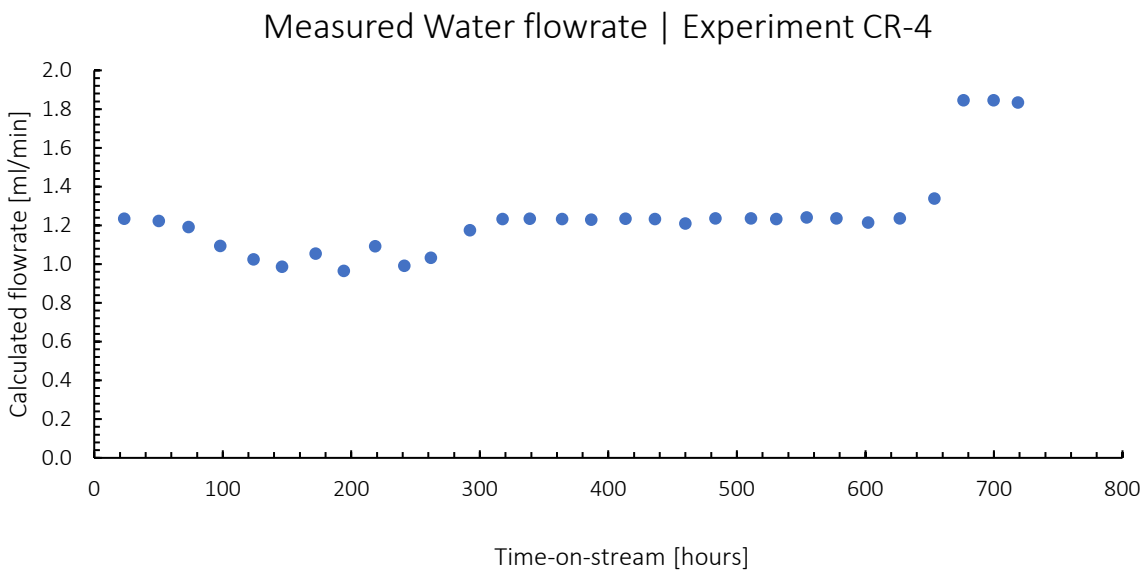

Figure A10.3: Measured water flowrate for Experiment CR-4

10.6. CRS-1

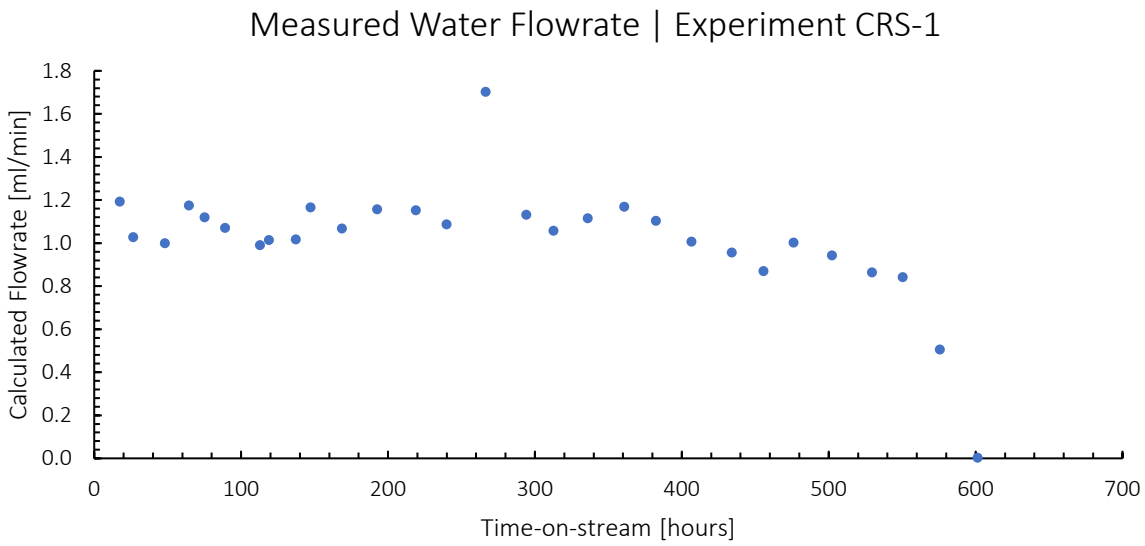

Figure A10.4: Measured water flowrate for experiment CRS-1

10.7. CRS-2

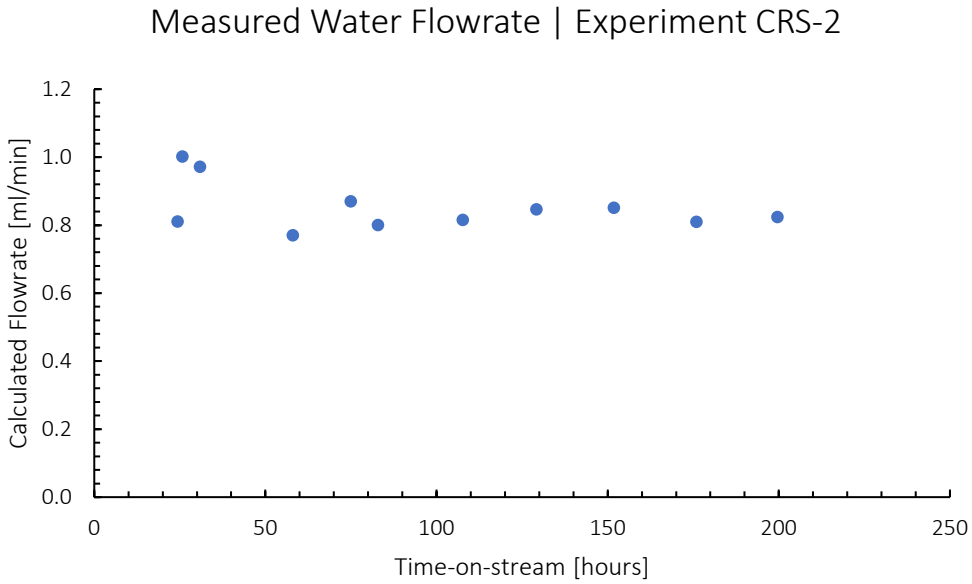

Figure A10.5: Measured water flowrate for experiment CRS-2

11. Appendix IV – Additional Characterisation Data

11.1. Spent Catalyst TGA-DTA-DTG Curves

11.1.1. Experiment CR-1

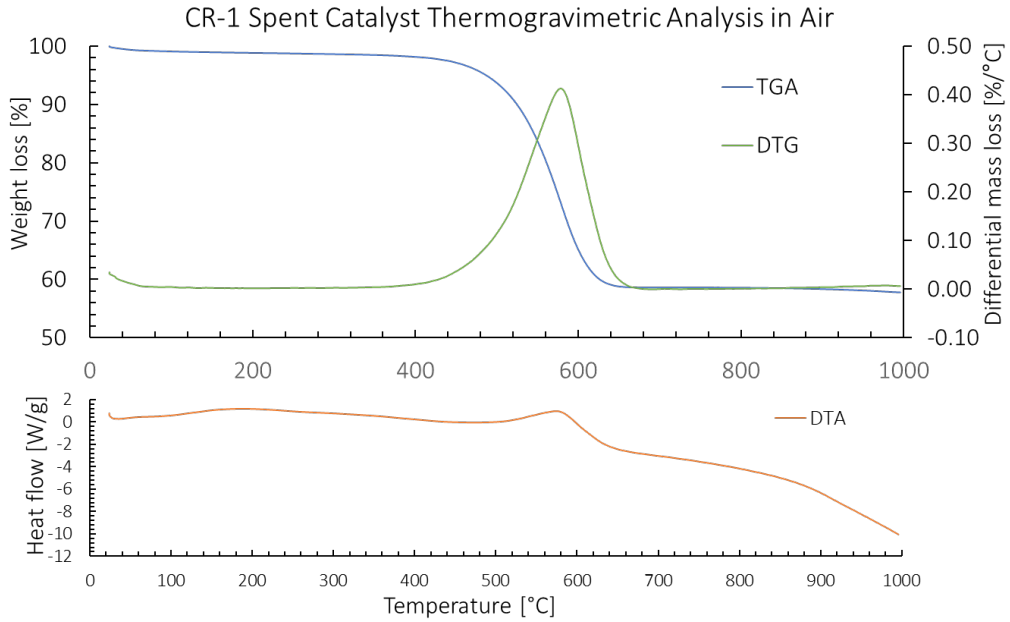

Figure A11.1: TGA-DTG-DTA Curves of recovered 5% Ru/Al_2O_3 catalyst used in CR-1 in air (10 sccm/min) at 3°C/min heating rate

Overall mass loss is 38.3%. Additional analyses indicated an average mass loss of 40.2% ± 1.9%. Mass loss peaks at 585°C, as indicated by the DTG curve.

11.1.2. Experiment CR-2

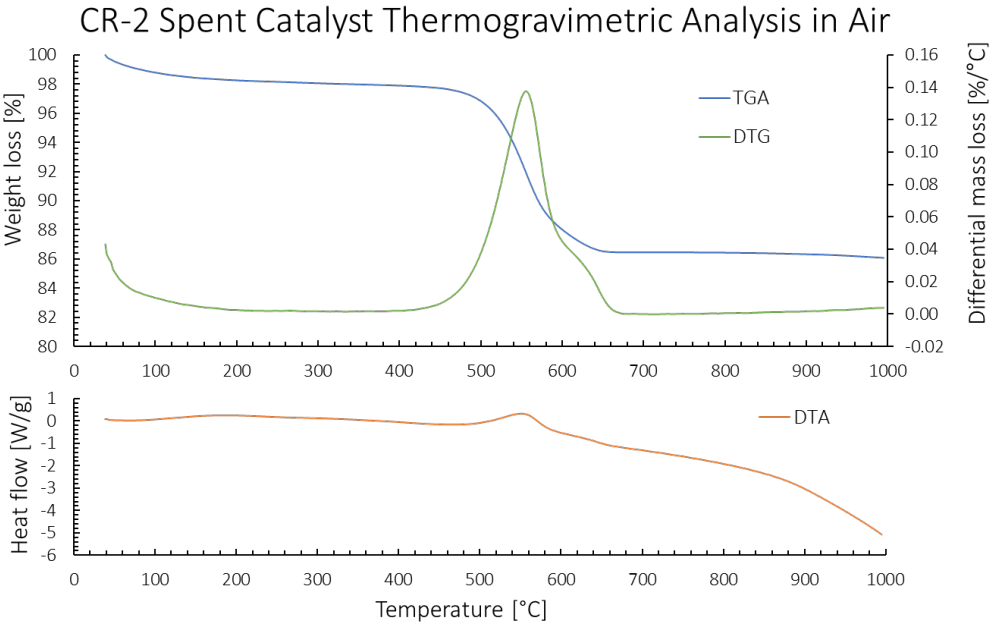

Figure A11.2: TGA-DTG-DTA Curves of recovered 5% Ru/Al_2O_3 catalyst used in CR-2 in air (10 sccm/min) at 3°C/min heating rate

Overall mass loss is 13.9%. Additional analyses indicated an average of 15.3 ± 1.2%. Mass loss has a peak at 560°C and a shoulder at 615°C, as indicated by the DTG curve.

11.1.3. Experiment CR-3

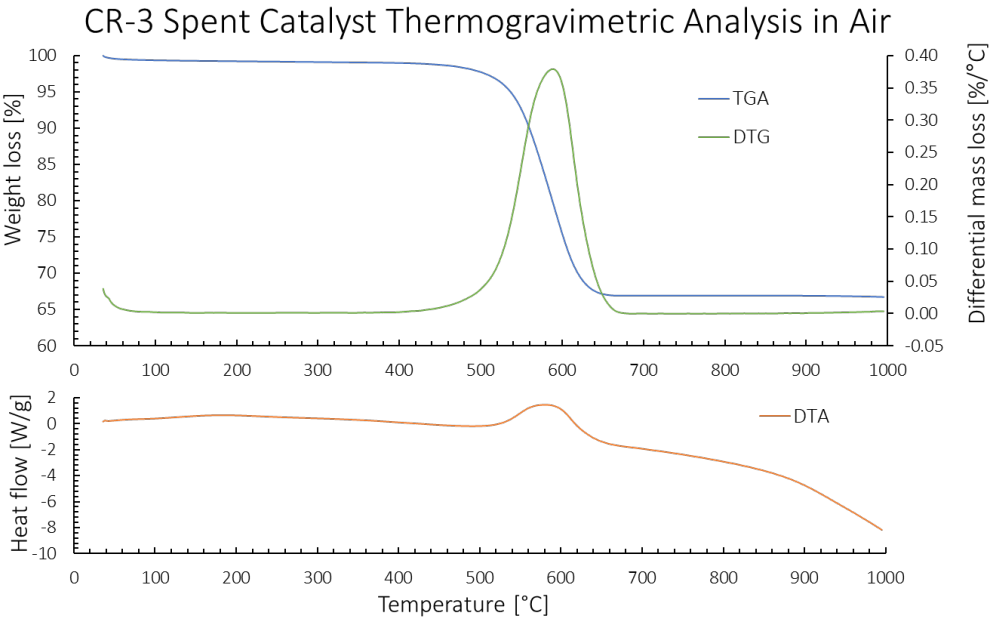

Figure A11.3: TGA-DTG-DTA Curves of recovered 5% Ru/Al_2O_3 catalyst used in CR-3 in air (10 sccm/min) at 3°C/min heating rate

Mass loss 33.3%. Additional analyses indicate an average of 33.8 ± 0.43%. Mass loss has a peak at 595°C, as indicated by the DTG curve.

11.1.4. Experiment CR-4

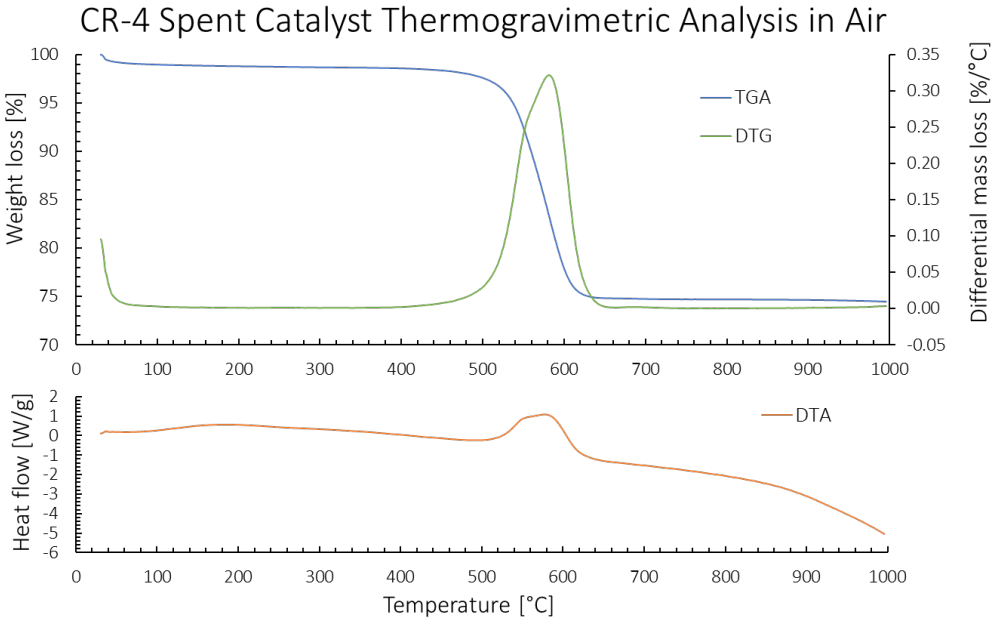

Figure A11.4: TGA-DTG-DTA Curves of recovered 5% Ru/Al_2O_3 catalyst used in CR-4 in air (10 sccm/min) at 3°C/min heating rate

Overall mass loss is 25.5%, and additional analyses indicate an average mass loss of 25.3 ± 0.2%. A single peak in mass loss is observed at 585°C.

11.1.5. Experiment CRS-1

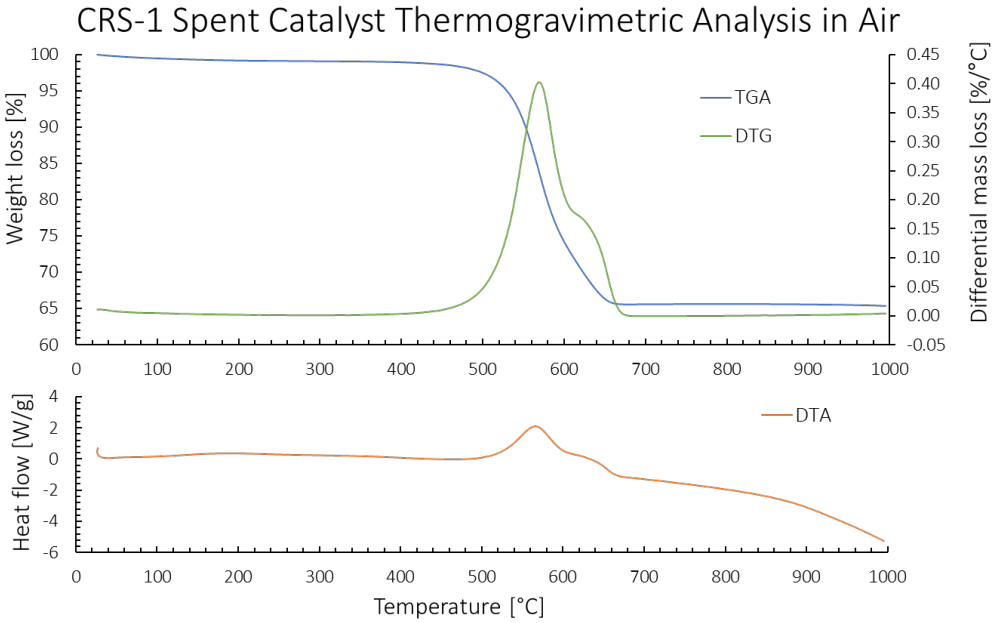

Figure A11.5: TGA-DTG-DTA Curves of recovered 5% Ru/Al_2O_3 catalyst used in CRS-1 in air (10 sccm/min) at 3°C/min heating rate

Overall mass loss is 34.7%. Additional analyses indicate an average mass loss of 34.4 ± 0.85%. Mass loss has a peak at 585°C and a shoulder at 625°C, as indicated by the DTG curve.

11.1.6. Experiment CRS-2

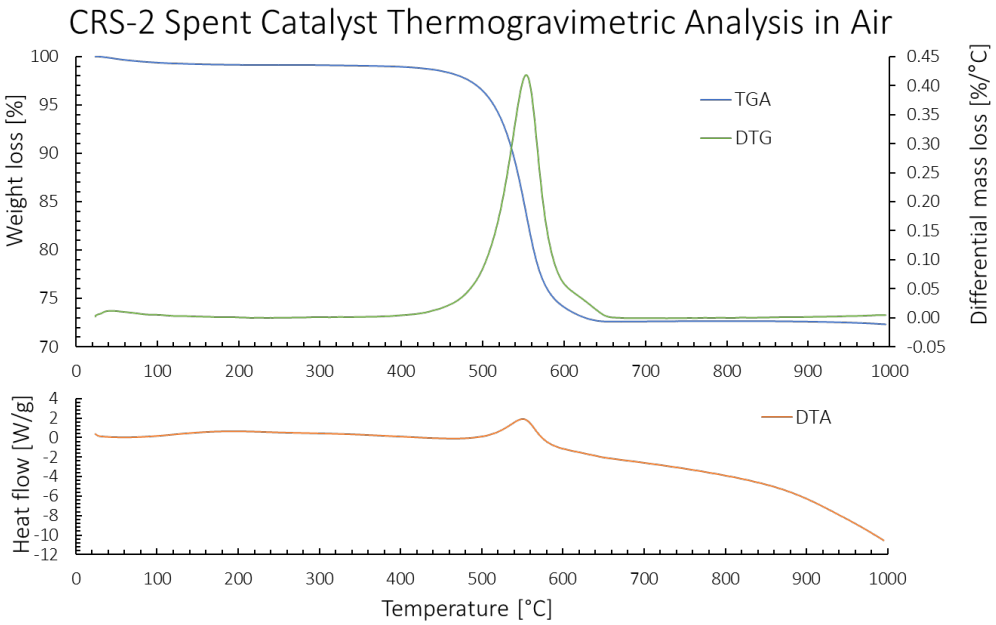

Figure A11.6: TGA-DTG-DTA Curves of recovered 5% Ru/Al_2O_3 catalyst used in CRS-2 in air (10 sccm/min) at 3°C/min heating rate

Overall mass loss is 27.7%. Additional analyses indicated an average mass loss of 29.4 ± 1.75%. Mass loss has a peak at 560°C, and a shoulder at 625°C, as indicated by the DTG curve.

12. Appendix V – Reactor Assembly

12.1. Reactor Head

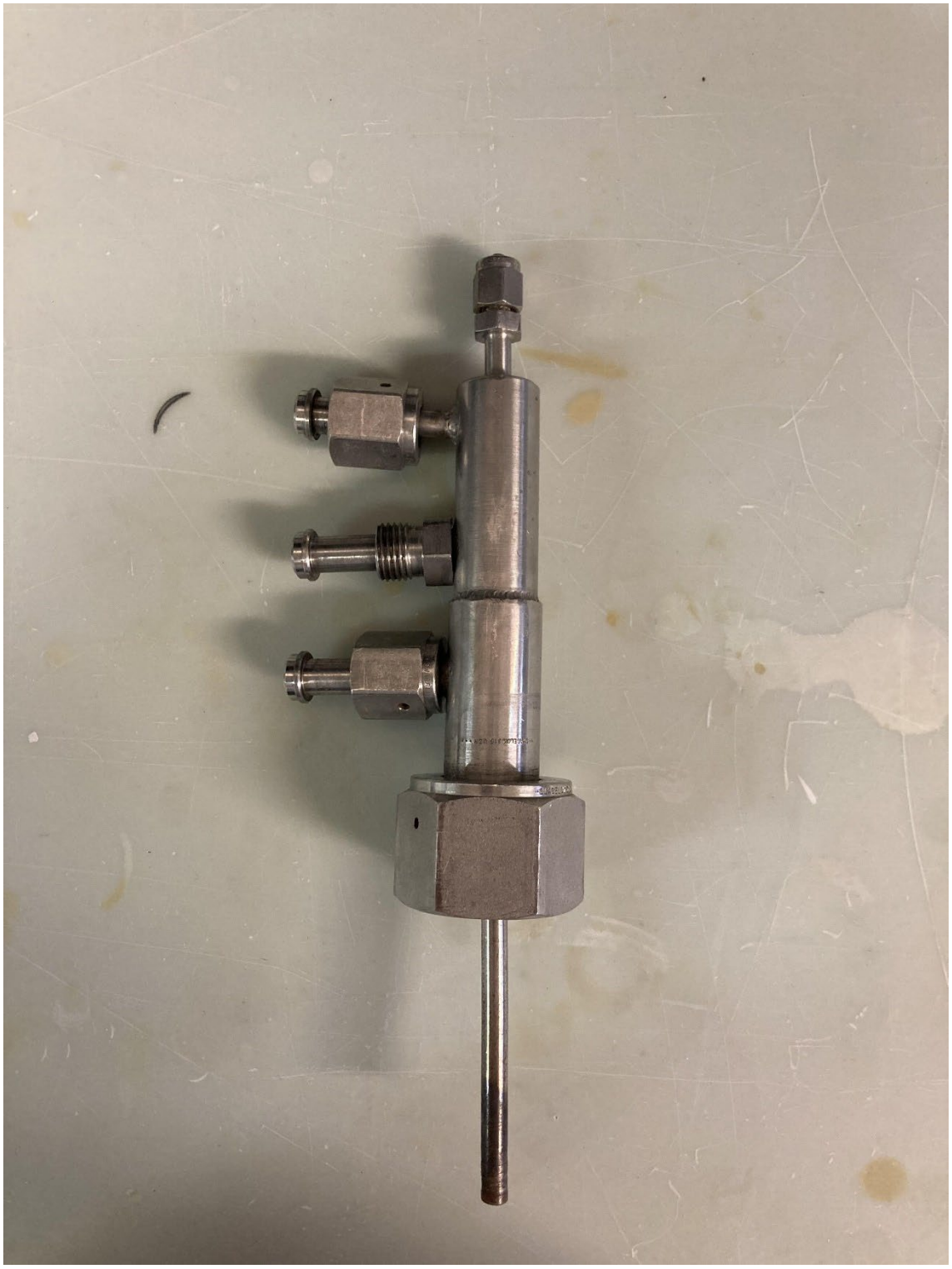

Figure A12.1: Reactor head indicating long inlet into SiC to mitigate risk of explosion

12.2. Reactor Tube with Catalyst Placement

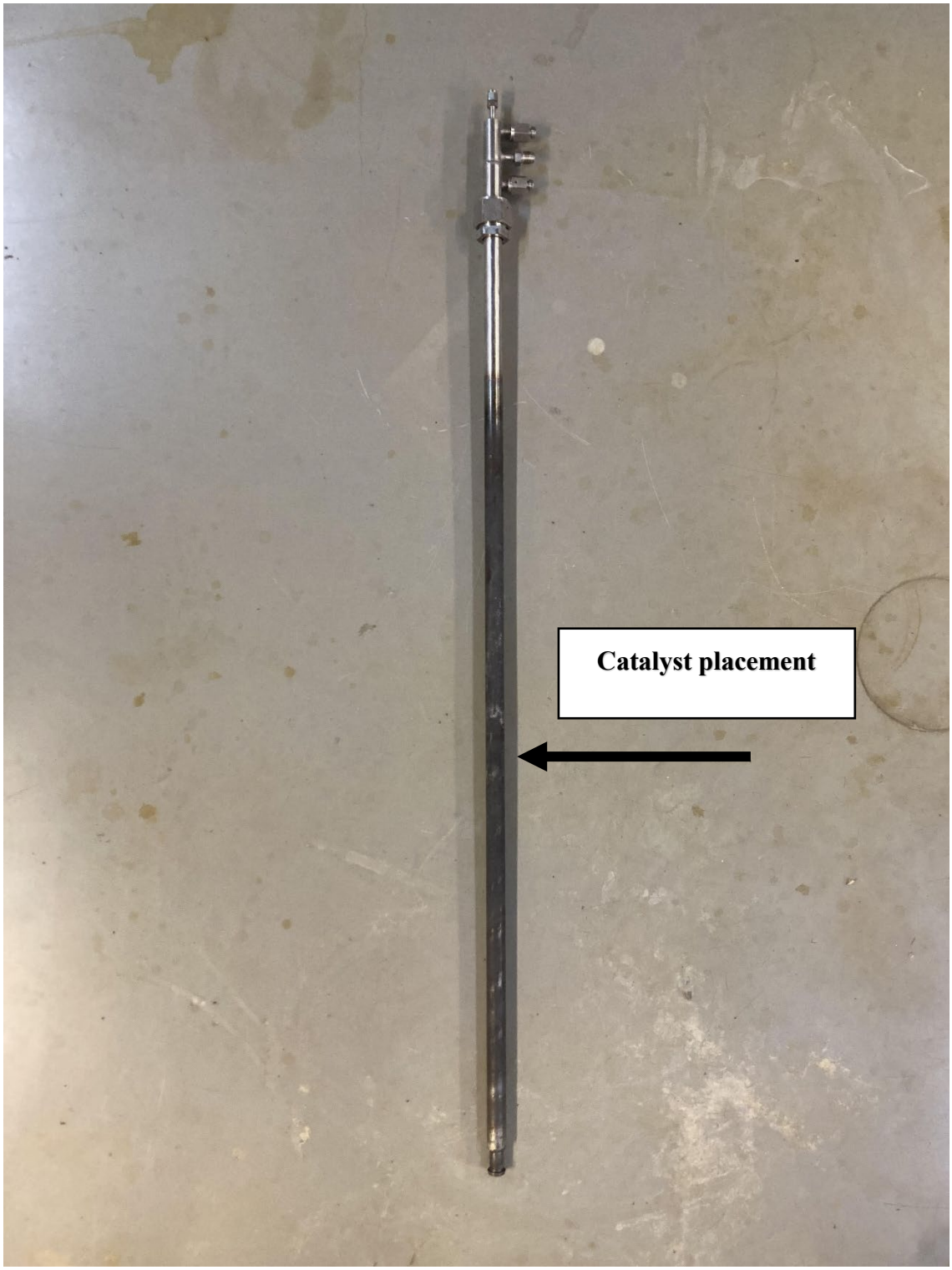

Figure A12.2: Reactor Tube with catalyst placement zone indicated by black arrow

Catalyst placement was determined using Figure 3.2, measured from the top of the reactor, which was 1 m long.

12.3. Water Catch Pot

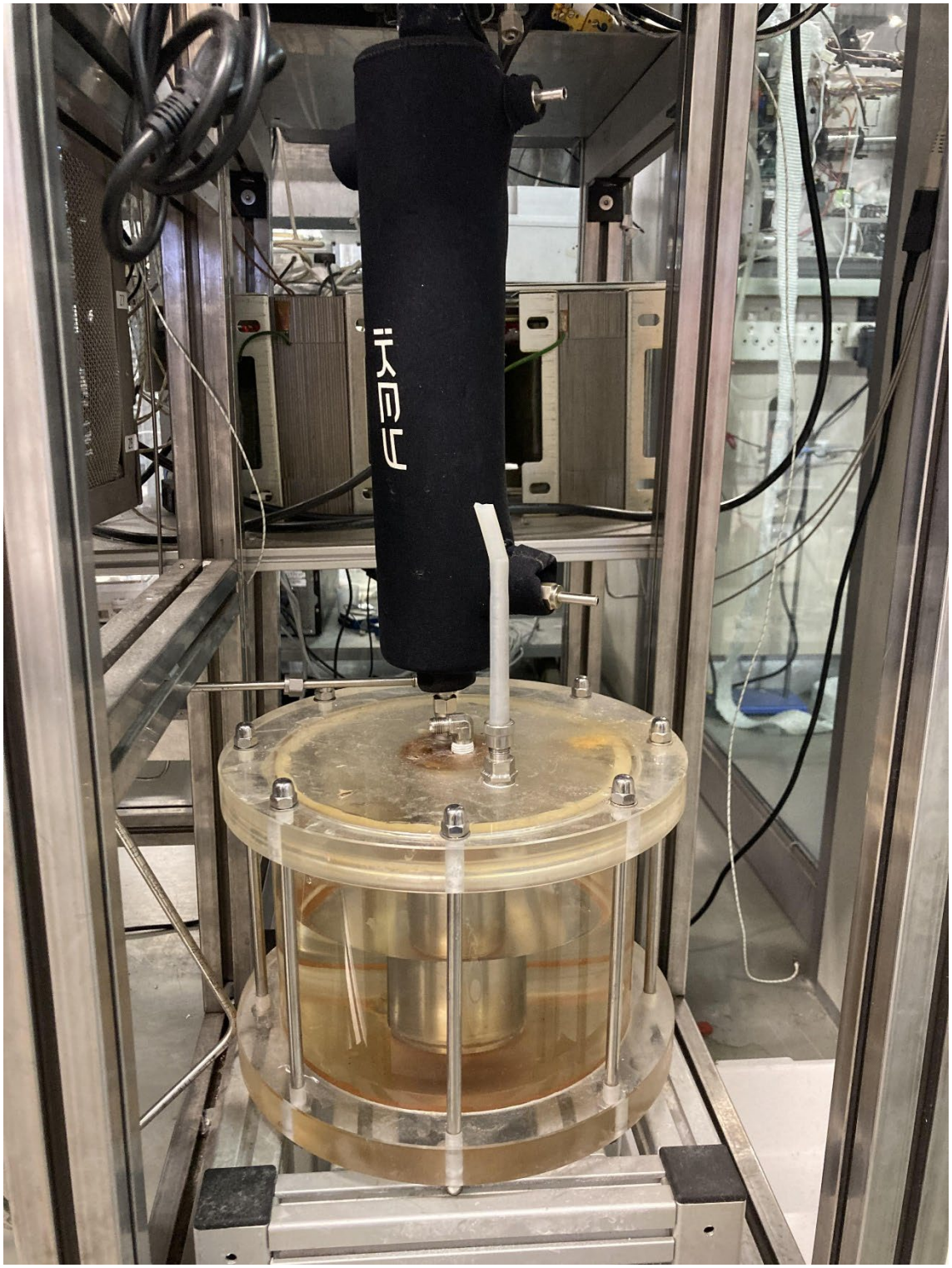

Figure A12.3: Water catch pot and connected chiller

13. Appendix VI: EBE Faculty "Assessment of Ethics in Research Project Form"

Application for Approval of Ethics in Research (EiR) Projects
Faculty of Engineering and the Built Environment, University of Cape Town

ETHICS APPLICATION FORM

Please Note:
Any person planning to undertake research in the Faculty of Engineering and the Built Environment (EBE) at the University of Cape Town is required to complete this form **before** collecting or analysing data. The objective of submitting this application *prior* to embarking on research is to ensure that the highest ethical standards in research, conducted under the auspices of the EBE Faculty, are met. Please ensure that you have read, and understood the **EBE Ethics in Research Handbook** (available from the UCT EBE, Research Ethics website) prior to completing this application form: http://www.ebe.uct.ac.za/ebe/research/ethics1

APPLICANT'S DETAILS		
Name of principal researcher, student or external applicant		Stephen Mark Cotterrell
Department		Chemical Engineering Department
Preferred email address of applicant:		CTTSTE004@myuct.ac.za
If Student	Your Degree: e.g., MSc, PhD, etc.	MSc
	Credit Value of Research: e.g., 60/120/180/360 etc.	120
	Name of Supervisor (if supervised):	Prof. Jack C.Q. Fletcher
If this is a researchcontract, indicate the source of funding/sponsorship		Departmental Funding
Project Title		Mitigating the deactivation of ruthenium-based steam reforming catalysts

I hereby undertake to carry out my research in such a way that:

- there is no apparent legal objection to the nature or the method of research; and
- the research will not compromise staff or students or the other responsibilities of the University;
- the stated objective will be achieved, and the findings will have a high degree of validity;
- limitations and alternative interpretations will be considered;
- the findings could be subject to peer review and publicly available; and
- I will comply with the conventions of copyright and avoid any practice that would constitute plagiarism.

APPLICATION BY	Full name	Signature	Date
Principal Researcher/ Student/External applicant	Stephen Mark Cotterrell	Signed by candidate	25/01/2021
SUPPORTED BY	**Full name**	**Signature**	**Date**
Supervisor (where applicable)	Jack CQ Fletcher	Signed by candidate	25 Jan 2021

APPROVED BY	Full name	Signature	Date
HOD (or delegated nominee) Final authority for all applicants who have answered NO to all questions in Section 1; and for all Undergraduate research (Including Honours).	Prof H von Blottnitz	Signed by candidate	7 March 2021
Chair: Faculty EIR Committee For applicants other than undergraduate students who have answered YES to any of the questions in Section 1.			